PhD Thesis

Cavity optomechanical feedback cooling and magnetic field sensing

Department of Physics

Technical University of Denmark

Jan Bílek

Supervisor: Professor Ulrik Lund Andersen
Co-supervisor: Associate Professor Tobias Gehring

March 2019

Abstract

This work is focused on the theoretical and experimental study of the interaction between electromagnetic radiation and mechanical micro-resonators. Through the radiation pressure interaction, it is possible to steer micromechanical oscillators into exotic, non-classical motional states - e.g. a Schrödinger cat state. The main requirement to observe a non-classical behaviour of massive mechanical oscillators is the ability to cool such oscillators into their motional quantum ground state. In the first part of this work, we investigate the feedback cooling of a tethered membrane vibration mode by radiation pressure. The presented experiment paves the way towards quantum control of macroscopic mechanical systems.

Due to the resonant enhancement of both optical and mechanical response, the cavity optomechanical devices allow ultra-sensitive measurements of displacement, forces or masses. The measurement precision is ultimately limited by the classical noise sources coupled to the system, e.g. thermal noise from the environment, or probe beam shot noise. In the second part if this work, we demonstrate that by interfacing the optomechanical sensor with a squeezed light, we can improve both its sensitivity and bandwidth. Specifically, we are using an on-chip SiO_2/Si whispering-gallery-mode resonator as a room temperature magnetic field sensor. In a proof-of-concept experiment, we show that at the frequencies, where the probe laser shot noise is the dominating noise source, injection of squeezed state lowers the detection noise floor thereby improving the peak sensitivity. Furthermore, the squeezed light broadens the frequency range at which thermal noise dominates, which increase the overall bandwidth of the sensor.

Dansk resumé

Nærværende afhandling er et teoretisk og eksperimentelt studie af den optomekaniske vekselvirkning mellem elektromagnetisk stråling og mekaniske mikroresonatorer. I kraft af vekselvirkningen, medieret af det optiske strålingstryk, er det muligt at drive den mekaniske resonator ud i eksotiske ikke-klassiske kvantetilstande som f.eks. Schrödingers kat-tilstande. En betingelse for at kunne frembringe og observere sådanne ikke-klassiske tilstande for makroskopiske objekter er, at de indledningsvist kan køles til deres kvantemekaniske grundtilstand. Det er en helt central udfordring, som har været omdrejningspunktet for den første del af afhandlingen. Konkret omhandler denne del et studie af feedbackkøling af mikromekaniske trampolinresonatorer ved hjælp af det optiske strålingstryk. Det eksperimentelle arbejde der fremlægges demonstrerer teknikken og dens potentiale som et værktøj til at opnå kvantefysisk kontrol over makroskopiske mekaniske systemer.

Optomekaniske systemer, der integrerer optiske og mekaniske resonatorer, muliggør ultra-sensitive målinger af fysiske parametre som amplituden af det mekaniske udsving, eksterne kraftpåvirkninger samt masse. Det skyldes den resonante forstærkning som både det optiske felt og det mekaniske respons oplever i sådanne systemer. Målingens præcision er fundamentalt begrænset af de klassiske støjkilder der uundgåeligt kobles til systemet, f.eks termisk støj fra omgivelserne og optisk kvantestøj på probelyset. I afhandlingens anden del demonstreres det, hvordan en forbedring af både sensitiviteten og båndbredden af denne type optomekaniske sensorer kan opnås under anvendelse af squeezed probelys, hvor den optiske fasestøj er reduceret under den sædvanlige kvantestøjsgrænse. Eksperimentelt eftervises dette for integrerede SiO_2/Si "whispering-gallery" resonatorer anvendt som magnetfeltsensorer ved standard rumtemperatur. Et proof-of-concept eksperiment viser, at i frekvensområder hvor optisk kvantestøj er dominerende, kan målingens støjgulv reduceres ved at anvende squeezed lys. Herved øges signal-støj-forholdet og sensorens følsomhed forbedres. Brugen af squeezed lys bevirker desuden en udvidelse at det frekvensområde hvor termisk støj er dominerende, hvilket forøger sensorens samlede båndbredde.

Acknowledgments

Firstly, I am grateful to the Ulrik L. Andersen for giving me an opportunity to be part of the QPIT research group, for sharing his insights to the field of optomechanics and for his always kind supervision.

Many thanks belong to my optomech fellows Ulrich B. Hoff, Joost van der Heijden, Iman M. Haghighi, and Dennis Høj who were around for varied periods of time during my studies. Ulrich's deep insight into optomechanics helped the whole project to go on, Joost helped me to design and to build the optomechanical and vacuum setup, Iman helped me in the lab and with understanding the theory, and Dennis Høj together with Kristian H. Rasmussen provided me with a never-ending supply of trampolines.

I also want to thank Clemens Schäfermeier who introduced me to the experiments in optomechanics, to Tobias Gehring, Christian S. Jacobsen, Jonas S. Neergaard-Nielsen and Xueshi Guo who gave me a lot of practical advice regarding the optical cavities and electronics, to Poul E. Andersen and Erik Hanses who turned a piece of metal into the optical cavity parts and manufactured various other components and finally to Tine H. Klitmøller for knowing answer to any administrative question.

During the work on the magnetometry experiment, I had the pleasure to collaborate with Warwick P. Bowen and Bei-Bei Li. Together with Bei-Bei we gathered and processed the data while Warwick's input was essential during writing the magnetometry article.

Special thanks belong to Ulrik L. Andersen, Ulrich B. Hoff, Joost van der Heijden, Iman M. Haghighi and Angelo Manetta for reading parts of this manuscript in a very short time and giving me a lot of insightful feedback. Furthermore, Ulrich also provided me with a Danish abstract.

Above all, I am grateful to my family and to Monika. Thank you for your endless patience, care, and love!

Lyngby, March 2019

Jan

Contents

List of Figures

List of Tables

Chapter 1

Introduction

Optomechanics is a rapidly developing field of research that explores the interaction between light and mechanical motion [1]. The momentum carried by light gives rise to the radiation pressure force which is the underlying mechanism of the optomechanical interaction. The capabilities of such hybrid systems have draw the attention of numerous scientist due to the extensive range of application, both in technology and fundamental science. The radiation pressure force was first postulated in the 17th century by Kepler, who noticed that the tails of comets always point away from the sun. Later, it was described by the use of Maxwell theory of electromagnetic radiation and the first experimental demonstration of radiation pressure force occured in 1885 [2].

The study of radiation pressure coupling to the motion of the mirror was pioneered by Braginsky in the context of interferometric gravitational wave detection [3]. It was discovered, that a probe beam coupled to the mirror to measure its position affects the measurement. This perturbance is caused by a momentum exchange between light and the mirror and leads to an imprecision in the mirror position, which then feeds back to the light. This effect is known as *quantum back-action* and sets a lower limit to the measurement sensitivity. Later, the theory of continuous quantum measurement and consequences of quantum fluctuations of radiation pressure to the measurement accuracy was formulated by Braginsky and Khalili [4].

Optical interferometric measurements enable the measurement of small variations of the position of the massive objects. For example, in a resonantly probed Fabry-Pérot interferometer, the motion of the end mirror may imprint a relatively large changes in the phase of the reflected probe beam. The uncertainty of the phase of the probe beam gives rise to the *imprecision noise*, which decreases with increasing laser power. However, increasing the laser power leads to a larger number of intracavity photons and thus

increased back-action noise. The limit in readout precision is achieved when the contribution from both noises is equal. This is known as the standard quantum limit (SQL).

In a seminal work by Caves [5] it was however realized that the standard quantum limit could be surpassed in gravitational wave interferometers using quantum correlated states of light. Those so-called squeezed states can exhibit phase fluctuations below the level attained by a coherent state (ideal laser) in the expense of larger amplitude fluctuations or vice versa. In other words, they lead to decrease in the imprecision noise and consequent increase of the radiation pressure-back action noise. Thus they allow reaching SQL with lower probe power and even surpassing the SQL when the quadrature phase of the squeezed state is rotated. Later, this was experimentally demonstrated for Mach-Zehnder [6], Michelson [7] and large-scale gravitational-wave interferometers [8]. In this work, we study the effect of using phase-squeezed light on the performance of a cavity optomechanical magnetometer.

Braginsky also predicted the dynamical effect of the radiation pressure on a harmonically suspended mirror of a cavity. When the lifetime of a photon inside the cavity is comparable or longer than a mirror oscillation period, retarded nature of a radiation pressure force may lead to either amplification or damping of the mirror motion. In case of damping, the scheme is in optomechanics referred to as *cavity-assisted cooling* or *sideband cooling*. Later, it was proposed [9] and demonstrated [10], that the delay in between radiation pressure force and mechanical oscillator (mirror) can be created externally using electro-optic systems. This scheme is referred to as *feedback cooling* or *cold damping*.

Cooling of a mechanical system to the motional quantum ground state is a necessary condition for observing its quantum behavior which is otherwise masked by the classical thermal noise. Laser cooling have been used to cool down trapped ions into their motional ground state [11], but ground state cooling of a larger system containing many atoms remained an elusive goal. A lot of effort was put in the direction of making cryogenic compatible optomechanical systems, with the aim of lowering the base temperature of oscillator's thermal bath. Eventually, cooling to the motional ground state by radiation pressure with cryogenic pre-cooling was achieved in microwave-frequency mechanical resonator [12]. Most recently, feedback cooling of a cryogenically pre-cooled phononic SiN membrane was demonstrated [13].

This work describes the development of the first cold damping experiment of SiN tethered membrane coupled to a Fabry-Pérot optical cavity in our group. The SiN tethered membranes - *trampolines* are nanogram-scale high aspect ratio mechanical resonators [14, 15]. The coupling of the membrane to its environment is significantly reduced by tethers leading to extremely low dissipation rate and thus potentially opening the doors for room temperature quantum experiments [14].

Chapter 2

Theoretical minimum

2.1 Quantum measurements

Quantum mechanics is based on non-commuting observables which characterize physically measurable quantities (e.g. position, momentum, energy,..). The act of measurement in quantum mechanics corresponds to the application of operator $\hat{\mathcal{O}}$ to the state $|\psi\rangle$. The outcome of such measurement must be one of the eigenvalues $\mathcal{O}_i$ of the operator $\hat{\mathcal{O}}$. Each operator have a set of eigenvalues which can be found by solving eigenvalue equation

$$\hat{\mathcal{O}}\,|\psi_i\rangle = \mathcal{O}_i\,|\psi_i\rangle\,. \tag{2.1}$$

Measuring the state which is prepared in the eigenstate of the operator $\hat{\mathcal{O}}$ must give output of the corresponding eigenvalue $\mathcal{O}_i$. If the system is prepared in arbitrary state $|\psi\rangle$ we can calculate the probability of obtaining result $\mathcal{O}_i$ by

$$\langle\hat{\mathcal{O}}\rangle = \langle\psi|\hat{\mathcal{O}}|\psi\rangle\,. \tag{2.2}$$

The first moment (mean value) of $\langle\hat{\mathcal{O}}\rangle$ is also called expectation value of the operator $\hat{\mathcal{O}}$. The spread of the results about the expectation value is characterized by variance which corresponds to the uncertainty of the measurement

$$Var(\hat{\mathcal{O}}) = (\Delta\hat{\mathcal{O}})^2 = \langle\hat{\mathcal{O}}^2\rangle - \langle\hat{\mathcal{O}}\rangle^2\,. \tag{2.3}$$

2.2 Uncertainty relations

We can see whether measuring of one quantum observable will affect the other by the operators commutator

$$[\hat{A},\hat{B}] \equiv \hat{A}\hat{B} - \hat{B}\hat{A} = \hat{C}. \tag{2.4}$$

If $\hat{A}\hat{B} = \hat{B}\hat{A}$ we will say that the operators commute. This means that $\hat{A}$ and $\hat{B}$ shares common set of eigenstates and we can measure their values with complete accuracy [16]. For the non-commuting operators $\hat{A}\hat{B} \neq \hat{B}\hat{A}$. The fact that two measured operators interferes with each other leads to the famous Haisenberg uncertainty relation [17]

$$\Delta\hat{A}\Delta\hat{B} \geq \frac{1}{2}|C|. \tag{2.5}$$

2.3 Quantum harmonic oscillator

Quantum harmonic oscillator is essential element of quantum optics and quantum mechanics in general. The motion of many wave-like systems are

well described by simple harmonic oscillator [16]. In this thesis, the formalism of quantum harmonic oscillator will be used to describe a single mode of a light inside an optical cavity as well as a single mode of mechanical vibration. The energy quanta of the optical mode is called *photon* and in case of the mechanical vibration *phonon*. This section will introduce some of the fundamental features of quantum harmonic oscillator. More details of the topic can be found in many quantum physics book such as [18].

Harmonic oscillator with mass m and angular frequency ω is described in quantum mechanics by the Hamiltonian

$$\hat{H} = \frac{m\omega\hat{q}^2}{2} + \frac{\hat{p}^2}{2m}, \tag{2.6}$$

where $\hat{q}$ and $\hat{p}$ are quantum position and momentum operators, respectively, which obey the commutation relation

$$[\hat{q}, \hat{p}] = i\hbar \tag{2.7}$$

The position and momentum operators can be expressed as a combination of *creation* $\hat{a}^\dagger$ and *annihilation* $\hat{a}$ operators as

$$\hat{q} = \sqrt{\frac{\hbar}{2m\omega}}(\hat{a}^\dagger + \hat{a}), \qquad \hat{p} = \sqrt{\frac{\hbar m\omega}{2}}i(\hat{a}^\dagger - \hat{a}). \tag{2.8}$$

The *creation* and *annihilation* operators are also called *ladder* operators because they act to add or subtract a single quantum of energy from the harmonic oscillator originally prepared in energy state $|n\rangle$

$$\hat{a}^\dagger |n\rangle = \sqrt{n+1}\,|n+1\rangle\,, \qquad \hat{a}\,|n\rangle = \sqrt{n}\,|n-1\rangle\,. \tag{2.9}$$

From the relations above we can directly see

$$\hat{a}^\dagger\hat{a}\,|n\rangle = n\,|n\rangle\,, \qquad \hat{n} \equiv \hat{a}^\dagger\hat{a}, \tag{2.10}$$

where we defined a number operator $\hat{n}$. The ground state $|0\rangle$ is defined by

$$\hat{a}\,|0\rangle = 0. \tag{2.11}$$

Using the ladder operators, we re-express the Hamiltonian 2.6

$$\hat{H} = \hbar\omega(\hat{a}^\dagger a + \frac{1}{2}) = \hbar\omega(\hat{n} + \frac{1}{2}) \tag{2.12}$$

and we will find the energy spectrum E_n of the quantum harmonic oscillator by solving the time-independent Schrödinger equation

$$\hat{H}\left|n\right\rangle = E_n\left|n\right\rangle, \tag{2.13}$$

$$\hbar\omega(\hat{n}+\frac{1}{2})\left|n\right\rangle = En\left|n\right\rangle, \tag{2.14}$$

$$En = \hbar\omega(n+\frac{1}{2}). \tag{2.15}$$

From the energy spectrum 2.15 we can see that energy levels are equally spaced by $\hbar\omega$ and that the ground state energy is equal to the *zero-point energy* of $\frac{1}{2}\hbar\omega$. As a consequence of the zero-point energy, there are *zero-point motion* and *zero-point momentum* of a quantum harmonic oscillator

$$q_{zpf} = \sqrt{\frac{\hbar}{2m\omega}}, \qquad p_{zpf} = \sqrt{\frac{\hbar m\omega}{2}}. \tag{2.16}$$

Field quadratures

We saw that the quantum harmonic oscillator is naturally described in terms of ladder operators. However, the annihilation and creation operator are non-Hermitian and thus do not represent real measurable observables. Taking their real and imaginary part we will get Hermitian operators called amplitude and phase quadratures

$$\hat{X}^q = \hat{a}^\dagger(\omega) + \hat{a}(\omega), \tag{2.17}$$

$$\hat{X}^p = -i(\hat{a}(\omega) - \hat{a}^\dagger(\omega). \tag{2.18}$$

We can also define a general quadrature as a linear superposition of and amplitude and phase quadratures

$$\hat{X}^\theta = \hat{a}(\omega)\mathrm{e}^{-i\theta} + \hat{a}^\dagger(\omega)\mathrm{e}^{i\theta} = \hat{X}^q(\omega)\cos\theta + \hat{X}^p(\omega)\sin\theta. \tag{2.19}$$

The quadrature operators satisfy the commutation relation

$$[\hat{X}^q, \hat{X}^p] = 2i \tag{2.20}$$

leading to the uncertainty relation

$$\Delta(\hat{X}^q)\Delta(\hat{X}^p) \geq 1 \tag{2.21}$$

The states which satisfy the equality in 2.21 are called *minimum uncertainty states*.

2.4 Quantum states of light

In this section we describe quantum states of light essential for this thesis.

Fock state

The Fock states, also called the Number states, $|n\rangle$ are eigenstates of the number operator $\hat{n}$

$$\hat{n}\,|n\rangle = n\,|n\rangle \tag{2.22}$$

As we saw on the example of the quantum harmonic oscillator, the single mode of the radiation (vibration) has the eigenvalues $\hbar\omega(n+\frac{1}{2})$ and the corresponding eigenstate $|n\rangle$. The number of photons (phonons) n is exactly defined so the variance of $\hat{n}$ is equal to zero in the Fock state

$$Var(\hat{n}) = \langle n|\hat{n}^2|n\rangle - \langle n|\hat{n}|n\rangle^2 = 0. \tag{2.23}$$

Looking at the expectation value of the arbitrary quadrature amplitude, we find that for a Fock state

$$\langle \hat{X}^\theta \rangle_n = \langle n|\hat{X}^\theta|n\rangle = 0. \tag{2.24}$$

The vanishing mean value means that the phase is completely undefined.

Properties of the quantum vacuum state $|0\rangle$ (number state with zero photons) plays a major role in quantum optical experiments, as they place a fundamental limit to precision of any classical field measurement. Evaluating the mean and variance of the amplitude and phase quadratures we find

$$\langle \hat{X}^q \rangle = \langle \hat{X}^p \rangle = 0, \qquad Var(\hat{X}^q) = Var(\hat{X}^p) = 1. \tag{2.25}$$

Fluctuations of the of the quantum vacuum state leads to the standard quantum limit for field quadrature measurements, also known as the the *shot noise limit*.

Coherent state

The quantum state which is the closest quantum approximation of the field generated by a laser is the *coherent state*. Coherent states are defined as eigenstates of a lowering (annihilation) operator $\hat{a}$ [16]:

$$\hat{a}\,|\alpha\rangle = \alpha\,|\alpha\rangle\,, \qquad \langle\alpha|\,\hat{a}^\dagger = \alpha^*\,\langle\alpha|\,, \tag{2.26}$$

with complex eigenvalue $\alpha = |\alpha|e^{i\theta}$. The complex eigenvalue reflects the fact that the annihilation operator is non-Hermitian. Expanding the coherent state into the number state basis we get

$$|\alpha\rangle = \sum_{n=0}^{\infty} |n\rangle\langle n|\alpha\rangle = e^{-\frac{1}{2}|\alpha|^2} \sum_{n=0}^{\infty} \frac{\alpha^n}{\sqrt{n!}} |n\rangle . \tag{2.27}$$

The number of photons in a coherent state with amplitude α has Poisson distribution

$$P(n) = |\alpha|^2 = e^{|\alpha|^2} \frac{(|\alpha|^2)^n}{n!}, \tag{2.28}$$

with the average photon number $\langle \hat{n} \rangle = |\alpha|^2$ and the variance $\mathrm{Var}(\hat{n}) = |\alpha|^2$. The mean value and variance of the quadratures in coherent state are

$$\langle \hat{X}^q \rangle = \alpha + \alpha^* = 2Re(\alpha), \qquad \langle \hat{X}^p \rangle = -i(\alpha - \alpha^*) = 2Im(\alpha), \tag{2.29}$$

$$Var(\hat{X}^q) = Var(\hat{X}^p) = 1. \tag{2.30}$$

From 2.30 we see that the coherent states are minimum uncertainty states. Coherent state can be also obtained by displacing vacuum state [18]

$$|\alpha\rangle = \hat{D}(\alpha) |0\rangle , \tag{2.31}$$

where $\hat{D}(\alpha) = \exp(\alpha\hat{a}^\dagger - \alpha^*\hat{a})$ is the displacement operator.

Squeezed state

As we shown above, the coherent and vacuum states have the same amount of quadrature fluctuations which are evenly distributed to the both quadratures and saturates the uncertainty relations as both states are minimum uncertainty states. However, it is possible to prepare a state with fluctuation in one quadrature suppressed below the shot noise. Then, the fluctuations in the conjugate quadrature will be proportionally increased to satisfy the Haisenberg uncertainty relations. Such a states are call *squeezed states* and are represented by [19]

$$|\alpha, \xi\rangle , \qquad \xi = r_s e^{i2\theta_s}, \tag{2.32}$$

where r_s is the degree of squeezing and θ_s is the squeezing phase. Mathematically, we can generate squeezed state from a vacuum state by applying squeezing operator $\hat{S}(\xi)$ and displacement operator $\hat{D}(\alpha)$

$$|\alpha, \xi\rangle = \hat{D}(\alpha)\hat{S}(\xi) |0\rangle , \tag{2.33}$$

where the squeezing operator is defined as [20]

$$\hat{S}(\xi) = \exp\left(\frac{1}{2}\xi^*\hat{a}^2 - \frac{1}{2}\xi\hat{a}^{\dagger 2}\right). \tag{2.34}$$

Squeezing of a general quadrature $\theta = \theta_s$ and its conjugated quadrature $\theta' = \theta_s + \pi/2$ is represented by action

$$\hat{S}^\dagger(\xi)\hat{X}^\theta\hat{S}(\xi) = \hat{X}^\theta\left(\cosh(r) - \sinh(r)\right) = \hat{X}^\theta e^{-r_s}, \tag{2.35}$$

$$\hat{S}^\dagger(\xi)\hat{X}^{\theta+\pi/2}\hat{S}(\xi) = \hat{X}^{\theta+\pi/2}\left(\cosh(r) + \sinh(r)\right) = \hat{X}^{\theta+\pi/2}e^{r_s}. \tag{2.36}$$

Looking at variance of squeezed states in both quadratures we get

$$Var\left(\hat{S}^\dagger(\xi)\hat{X}^\theta\hat{S}(\xi)\right) = e^{-2r_s}Var(\hat{X}^\theta), \tag{2.37}$$

$$Var\left(\hat{S}^\dagger(\xi)\hat{X}^{\theta+\pi/2}\hat{S}(\xi)\right) = e^{2r_s}Var(\hat{X}^{\theta+\pi/2}), \tag{2.38}$$

which shows that a variance of the state in squeezed quadrature θ_s is reduced while the variance of the state in conjugate quadrature is increased.

Thermal state

Thermal states describes harmonic oscillator which is in equilibrium with its environment. Since both photon and phonons are Bosons, the occupancy probability $p(n)$ at thermal equilibrium follows the Bose-Einstein statistics

$$p(n) = \exp\left(-\frac{\hbar\omega n}{k_B T}\right)\left[1 - \exp\left(-\frac{\hbar\omega}{k_B T}\right)\right], \tag{2.39}$$

where T is the temperature of the environment and k_B is Boltzmann's constant. The mean occupancy of the oscillator and variance are

$$\langle\hat{n}\rangle = \sum_{n=0}^{\infty} np(n) = \left[\exp\left(\hbar\omega/k_B T\right) - 1\right]^{-1}, \quad Var(\hat{n}) = \langle\hat{n}^2\rangle - \langle\hat{n}\rangle^2. \tag{2.40}$$

Larger oscillators typically has smaller resonant frequencies. Macroscopic oscillators at a room temperature satisfies $k_B T \gg \hbar\omega$. Within this approximation know as a *classical limit* the expression 2.40 simplifies to

$$\langle n\rangle_{k_B T \gg \hbar\omega} = \frac{k_B T}{\hbar\omega}. \tag{2.41}$$

On the other side, visible light has a frequency of an order $\omega/2\pi \approx 10^{14}$. The thermal occupancy at a room temperature using equation 2.40 then gives

$\langle n \rangle \approx 10^{-35}$. This means, that optical fields in thermal equilibrium at room temperature are effectively in a ground state and can act as a cold bath [21].

Thermal state is a mixed state which can be conveniently described by a density matrix $\hat{\rho}$, which in a number state representation reads

$$\hat{\rho} = \sum_{n=0}^{\infty} \frac{\langle \hat{n} \rangle^n}{(1 + \langle \hat{n} \rangle)^{n+1}} |n\rangle\langle n| . \tag{2.42}$$

The expectation value of an operator $\hat{O}$ in a state represented by density matrix is $\langle \hat{O} \rangle = \mathrm{Tr}(\rho \hat{O})$, where Tr denotes a trace. Now, we can easily calculate expectation value and variance of the quadrature operator

$$\langle \hat{X}^\theta \rangle = 0, \qquad Var(\delta \hat{X}^\theta) = \langle n \rangle + \frac{1}{2} \tag{2.43}$$

2.5 Modulation of light

By interaction with its environment, light can experience modification of its amplitude and phase and thus acquire information about the environment. This can be also used to deliberately encode the information on the light beam using modulation techniques briefly described in this section.

Phase modulation

We represent laser beam by a monochromatic scalar light field $\alpha(t) = \alpha_0 \mathrm{e}^{i\omega_0 t}$ with amplitude α_0 and angular frequency ω_0. Amplitude α_0 can be considered to be real as any absolute phase offset cannot be directly measure without a reference beam. Harmonic phase modulation at the frequency ω_m can be described as

$$\alpha_{PM}(t) = \alpha(t) \mathrm{e}^{iM cos(\omega_m t)}, \tag{2.44}$$

where M is the modulation index. To expand the term above we will use following identities

$$\mathrm{e}^{iM\cos\theta} = \sum_{j=-\infty}^{\infty} i^j J_j(M) \mathrm{e}^{ij\theta} \quad \text{and} \quad J_j(M) = \sum_{l=1}^{\infty} \frac{(-1)^l}{l!(l+j)} \left(\frac{M}{2}\right)^{j+2l}, \tag{2.45}$$

where $J_j(M)$ are the *Bessel functions of the first kind* of the order j. For the small modulation depth ($M < 1$) we express phase modulated field using first order sidebands ($j = 1$) as

$$\begin{aligned} \alpha_{PM}(t) &\approx \alpha_0 \mathrm{e}^{i\omega_0 t} \left[J_0(m) + iJ_1(M)\mathrm{e}^{i\omega_m t} + iJ_1(M)\mathrm{e}^{-i\omega_m t} \right] \\ &= \alpha_0 \mathrm{e}^{i\omega_0 t} \left[1 + i\frac{M}{2} \left(\mathrm{e}^{i\omega_m t} + \mathrm{e}^{-i\omega_m t} \right) \right]. \end{aligned} \tag{2.46}$$

The phase modulated light is represented by a sum of three light fields at different frequencies. Field with frequency of unmodulated field ω_0 is called *carrier*. Fields with lower and higher frequency $\omega_0 \mp \omega_m$ are called *lower* and *upper sidebands*, respectively. In general, phase modulation leads to the creation of infinite amount of sidebands.

Frequency modulation

Frequency modulation has the same effect as a phase modulation considering small modulation depth. Frequency ν of a wave is defined as a first derivative of the phase

$$\nu = \frac{\omega}{2\pi} = \frac{d\theta}{dt}. \tag{2.47}$$

Sinusoidally modulated frequency can be described as

$$\omega = M' \sin(\omega_m t), \tag{2.48}$$

which leads to the phase of frequency modulated light

$$\theta = \int M' \sin(\omega_m t) dt = -\frac{M'}{\omega_m} \cos(\omega_m t). \tag{2.49}$$

Formally we obtained the same phase relation as for the phase modulated light given by Eq. 2.44 with modulation index $M = \frac{M'}{\omega_m}$. In the practical cases, modulation index of phase modulated light is typically smaller ($M < 10$) compared to the frequency modulated light ($M > 10^4$). Expansion to the Bessel functions can be still used, but with taking into account many more terms.

Amplitude modulation

Light field which its amplitude is sinusoidally modulated can be expressed as

$$\begin{aligned} \alpha_{AM}(t) &= \alpha(t)(1 + M\cos(\omega_m t)) \\ &= \alpha_0 \mathrm{e}^{i\omega_0 t} \left[1 + \frac{M}{2}\left(\mathrm{e}^{i\omega_m t} + \mathrm{e}^{-i\omega_m t}\right)\right]. \end{aligned} \tag{2.50}$$

We can notice that the amplitude of the carrier field is not affected by modulation. This is the case of active modulation utilized e.g. by modulating

laser pump current. In the case of passive modulation, which is naturally achieved by the attenuation, we can rewrite Eq. 2.50 as

$$\begin{aligned}\alpha_{AM}(t) &= \alpha(t)\left[1-\frac{M}{2}\left(1-\cos(\omega_m t)\right)\right] \\ &= \alpha_0 \mathrm{e}^{-\omega_0 t}\left[1-\frac{M}{2}+\frac{M}{4}\left(\mathrm{e}^{i\omega_m t}+\mathrm{e}^{-i\omega_m t}\right)\right].\end{aligned} \tag{2.51}$$

Unlike the phase (frequency) modulation, amplitude modulation leads always to creation of exactly two sidebands. Furthermore, maximum modulation index ($M = 1$) exists.

2.6 Detection

Now, when we established the properties of the most important states of light, we need describe how they are measured in the experiments. By the measurement - *detection* we mean transferring the optical field to the electronic signal.

2.6.1 Power spectral density

As discussed previously, the information can be imprinted to the phase or amplitude of the light field in the form of sidebands around the unmodulated carrier. We are often interested in resolving those fluctuations in the frequency domain in terms of the power spectral density (PSD). The power spectral density tells us the intensity of the noise at given frequency. For an operator $\hat{\mathcal{O}}$, the PSD can be related to the operator autocorrelation function as [22]

$$S_{\mathcal{O}\mathcal{O}}(\omega) \equiv \lim_{\tau\to\infty}\frac{1}{\tau}\left\langle \hat{\mathcal{O}}_\tau^\dagger(\omega)\hat{\mathcal{O}}_\tau(\omega)\right\rangle, \tag{2.52}$$

where $\mathcal{O}_\tau(\omega)$ is a windowed Fourier transform of $\mathcal{O}(t)$ over an time interval $(-\tau/2;\tau/2)$. The Fourier transform $\mathcal{F}$ and inverse Fourier transform $\mathcal{F}^{-1}$ are defined as follow

$$\mathcal{O}(\omega) = \mathcal{F}\left(\mathcal{O}(t)\right) = \int_{-\infty}^{\infty}\mathcal{O}(t)e^{i\omega t}dt, \tag{2.53}$$

$$\mathcal{O}(t) = \mathcal{F}^{-1}\left(\mathcal{O}(\omega)\right) = \frac{1}{2\pi}\int_{-\infty}^{\infty}\mathcal{O}(\omega)e^{-i\omega t}d\omega, \tag{2.54}$$

yielding the windowed Fourier transform

$$\mathcal{O}_\tau(\omega) = \int_{-\tau/2}^{\tau/2}\mathcal{O}(t)e^{i\omega t}dt. \tag{2.55}$$

Useful relation is provided by a Wiener-Khinchin theorem linking the time autocorrelation function with a PSD. For an operators with a stationary statistics and its conjugate it gives

$$S_{\mathcal{O}\mathcal{O}}(\omega) = \int_{-\infty}^{\infty} d\tau e^{i\omega\tau} \left\langle \hat{\mathcal{O}}^\dagger(\tau)\hat{\mathcal{O}}(0) \right\rangle \tag{2.56}$$

$$S_{\mathcal{O}^\dagger\mathcal{O}^\dagger}(\omega) = \int_{-\infty}^{\infty} d\tau e^{i\omega\tau} \left\langle \hat{\mathcal{O}}(\tau)\hat{\mathcal{O}}^\dagger(0) \right\rangle, \tag{2.57}$$

where $S_{\mathcal{O}\mathcal{O}}(\omega)$ and $S_{\mathcal{O}^\dagger\mathcal{O}^\dagger}(\omega)$ are always real. One must be careful to distinguish in between the quantum PSD described here and a PSD of a classical variable. The latter is always symmetric in frequency i.e. $S_{OO}(\omega) = S_{OO}(-\omega)$ which is not true in general for a quantum PSD. The reason behind is that unlike a classical variable, the quantum operators do not necessarily commute with their value at another time i.e. $[\hat{\mathcal{O}}(t), \hat{\mathcal{O}}(t')] \neq 0$, which leads to asymmetric PSD: $S_{\mathcal{O}\mathcal{O}}(\omega) \neq S_{\mathcal{O}\mathcal{O}}(-\omega)$. As an example, the position operator of quantum harmonic oscillator $\hat{q}(t)$ after a quarter of oscillton perion evolves as $\hat{q}(t+\tau) = \hat{p}$, with $\tau = \pi/2\Omega$, which clearly does not commute with $\hat{q}(t)$ [21].

2.6.2 Linearised operators

In the case of bright optical fields, it is convenient to split an operator to the classical part $\alpha = \langle \hat{a} \rangle$ and fluctuating part $\delta\hat{a}$

$$\hat{a}(t) = \alpha + \delta\hat{a}(t) \tag{2.58}$$

This assumption is valid when the amplitude α is much larger than any operator fluctuation $\delta\hat{a}$, which is a case for a bright laser beams [20]. Detecting the laser beam on a photodiode yields an output photocurrent proportional to

$$\begin{aligned} \hat{n} &= \hat{a}^\dagger\hat{a} \\ &= \left(\alpha + \delta\hat{a}^\dagger(t)\right)(\alpha + \delta\hat{a}) \\ &= \alpha^2 + \alpha\delta\hat{X}_1(t), \end{aligned} \tag{2.59}$$

where we neglected all higher order terms $\delta\hat{a}(t)\delta\hat{a}^\dagger(t)$. From the result above, we see that a detection on a photodiode - e.g. direct detection, effectively measures the amplitude quadrature of light $\hat{X}^q$. Measuring an arbitrary quadrature is possible by introducing another bright reference beam, which is discussed in a homodyne detection section.

2.6.3 Direct detection

The most straightforward approach to measure the optical field is a direct detection on a *photodiode*. Considering optical coherent field with linearised operators (approximation of a bright laser beam) the output photocurent is given as

$$\begin{aligned} i(t) &= g_D \hat{n}(t) = g_D \hat{a}^\dagger(t)\hat{a}(t) \\ &= g_D(\alpha(t) + \delta\hat{a}^\dagger)(\alpha(t) + \hat{a}) \approx g_D(\alpha^2 + \alpha\delta\hat{X}_1(t)) \qquad (2.60) \\ i(\Omega) &= g_D(\alpha^2\delta(\Omega) + \alpha\delta\hat{X}^q(\Omega)). \qquad (2.61) \end{aligned}$$

We see that the the photocurrent is directly proportional to the number of photons with proportional constant g_D representing the gain of the detector and detection efficiency.

2.6.4 Beam splitter

Beam-splitter is simple but powerful tool in quantum optics. In practice, the simplest elements in optical experiments are a mirrors. Dielectric mirrors are made by stacking thin layers of different optically thick materials on a substrate. The mirror either transmits or reflects the input beam, thus there are two output ports for every input beam, hence a beamsplitter. Here, we consider idealised model of a loss-less beam splitter shown in Fig. 2.1. The input field operators can be related to the output fields as

$$\begin{pmatrix} \hat{a}_{out} \\ \hat{b}_{out} \end{pmatrix} = \begin{pmatrix} \sqrt{\eta} & \sqrt{1-\eta} \\ -\sqrt{1-\eta} & \sqrt{\eta} \end{pmatrix} \begin{pmatrix} \hat{a}_{in} \\ \hat{b}_{in} \end{pmatrix}, \qquad (2.62)$$

where η is real and corresponds to the intensity transmittance. From relation 2.62 we see that output of a beam-splitter at each port is linear combination of input operators

$$\begin{aligned} \hat{a}_{out} &= \sqrt{\eta}\hat{a}_{in} + \sqrt{1-\eta}\hat{b}_{in}, \\ \hat{b}_{out} &= \sqrt{\eta}\hat{b}_{in} - \sqrt{1-\eta}\hat{a}_{in}. \qquad (2.63) \end{aligned}$$

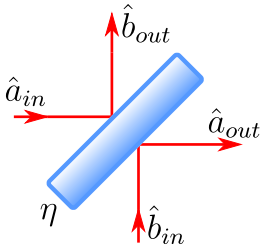

Figure 2.1: Simple beam splitter (beamsplitter) model. The input fields are transformed to the output beam according to the Eq. 2.63.

2.6.5 Homodyne detection

Homodyne detector enables us to measure arbitrary quadrature of the optical field. As illustrated in the figure 2.2, the input state α_{sig} is combined on a beamsplitter with local oscillator α_{LO}. Considering linearised operators, the optical fields at detectors $\hat{d}_1$ and $\hat{d}_2$ reads

$$\hat{d}_1(t) = \frac{1}{\sqrt{2}}\Big[\big(\alpha_{LO} + \delta\hat{a}_{LO}(t)\big)\mathrm{e}^{i\theta} + \big(\alpha_{sig}(t) + \delta\hat{a}_{sig}(t)\big)\Big], \tag{2.64}$$

$$\hat{d}_2(t) = \frac{1}{\sqrt{2}}\Big[\big(\alpha_{sig} + \delta\hat{a}_{sig}(t)\big) - \big(\alpha_{LO}(t) + \delta\hat{a}_{LO}(t)\big)\mathrm{e}^{i\theta}\Big], \tag{2.65}$$

where θ denotes the relative phase between signal and local oscillator fields. The amplified currents at each diode yield

$$\begin{aligned} i_1(t) &= g_D\hat{d}_1^{\dagger}(t)\hat{d}_1(t) \\ &\approx \frac{g_D}{2}\Big[\alpha_{sig}(t)^2 + \alpha_{LO}(t)^2 + 2\alpha_{LO}(t)\alpha_{sig}(t)\cos\theta + , \\ &\alpha_{sig}(t)\big(\delta\hat{X}^q_{sig}(t) + \delta\hat{X}^{-\theta}_{LO}(t)\big) + \alpha_{LO}(t)\big(\delta\hat{X}^q_{LO}(t) + \delta\hat{X}^{\theta}_{sig}(t)\big)\Big], \end{aligned} \tag{2.66}$$

$$\begin{aligned} i_2(t) &= g_D\hat{d}_2^{\dagger}(t)\hat{d}_2(t) \\ &\approx \frac{g_D}{2}\Big[\alpha_{sig}(t)^2 + \alpha_{LO}(t)^2 - 2\alpha_{LO}(t)\alpha_{sig}(t)\cos\theta + , \\ &\alpha_{sig}(t)\big(\delta\hat{X}^q_{sig}(t) - \delta\hat{X}^{-\theta}_{LO}(t)\big) + \alpha_{LO}(t)\big(\delta\hat{X}^q_{LO}(t) - \delta\hat{X}^{\theta}_{sig}(t)\big)\Big], \end{aligned} \tag{2.67}$$

where g_D is the electronic gain. Looking at the sum and the difference of photocurrents while considering $\alpha_{LO} \gg \alpha_{sig}$ so dropping terms not multiplied by α_{LO}, we arrive at

$$i_+(t) = i_1(t) + i_2(t) = g_D\Big(\alpha_{sig}(t)^2 + \alpha^2_{LO}(t) + \alpha_{LO}\delta\hat{X}^q_{LO}(t)\Big), \tag{2.68}$$

$$i_-(t) = i_1(t) - i_2(t) = g_D\Big(2\alpha_{LO}(t)\alpha_{sig}(t)\cos\theta + \alpha_{LO}\delta\hat{X}^{\theta}_{sig}(t)\Big). \tag{2.69}$$

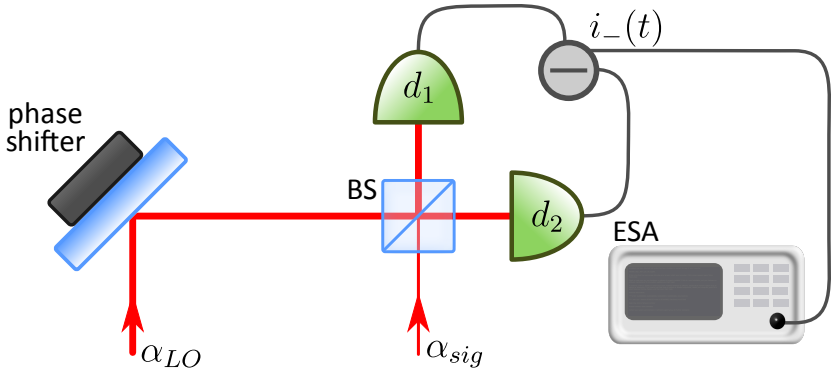

Figure 2.2: Schematics of a homodyne detection.

By taking a Fourier transform of the fluctuations terms, we get the currents sum and difference in frequency domain

$$i_+(\omega) = g_D\alpha(t)\hat{X}^q_{LO}(\omega) \qquad Var(i_+(\omega)) = g_D^2\alpha_{LO}^2 Var(\hat{X}^q_{LO}(\omega)), \tag{2.70}$$

$$i_-(\omega) = g_D\alpha(t)\hat{X}^\theta_{sig}(\omega) \qquad Var(i_-(\omega)) = g_D^2\alpha_{LO}^2 Var(\hat{X}^\theta_{sig}(\omega)). \tag{2.71}$$

We can see that, by measuring the photocurrents difference, we can probe arbitrary field quadrature by setting the relative phase θ. Furthermore, the quadrature is amplified by the local oscillator which is typically 10^3 times stronger that a measured signal. On the other hand, the current sum always measures the amplitude quadrature of the local oscillator independent of the measurement phase.

2.6.6 Optical loss

Losses can have dramatic impact on fragile quantum states. There are many channels through which the losses are introduced to the system. A widespread source of losses in the experiment comes from a Fresnel loss, imperfection of the optics coating, imperfection of photodiodes, or non-perfect modematching. The annihilation operator of the state after the effect of loss is given as

$$\hat{a}_{out}(t) = \sqrt{\epsilon}\hat{a}_{in}(t) + \sqrt{1-\epsilon}\hat{a}_{vac}(t), \tag{2.72}$$

which corresponds to the beam splitter transformation with efficiency given by ϵ and losses $1-\epsilon$. For a negligible losses i.e. $\epsilon \to 1$, the $\hat{a}_{out}(t) \to \hat{a}_{in}(t)$. From Eq. 2.72 we see the twofold effect of the losses - the original state is attenuated and admixed with a vacuum state $\hat{a}_{vac}$. The variance of the general quadrature state subject to the losses reads

$$Var(\hat{X}^\theta_{out}) = \epsilon\hat{X}_{in} + (1-\epsilon), \tag{2.73}$$

recalling that the variance of the vacuum state in any quadrature $\hat{X}_{vac} = 1$.

Chapter 3

Optomechanical interaction

3.1 The optomechanical Hamiltonian

The simple model of an optomechanical system consists of a linear optical cavity, with one of the mirrors suspended on a spring allowing the mirror to oscillate in the direction of the cavity optical axis. Such a system can be describe with the following Hamiltonian

$$\hat{H} = \underbrace{\frac{m_{eff}\Omega_m^2\hat{q}^2}{2} + \frac{\hat{p}^2}{2m_{eff}}}_{\hat{H}_m} + \overbrace{\hbar\omega_c\hat{a}^\dagger\hat{a}}^{\hat{H}_o}, \tag{3.1}$$

where $\hat{H}_m$ denotes the Hamiltonian of the mechanical oscillator with effective mass m_{eff} and resonance frequency Ω_m and $\hat{H}_o$ corresponds to the optical energy stored inside the cavity with resonance frequency ω_c.

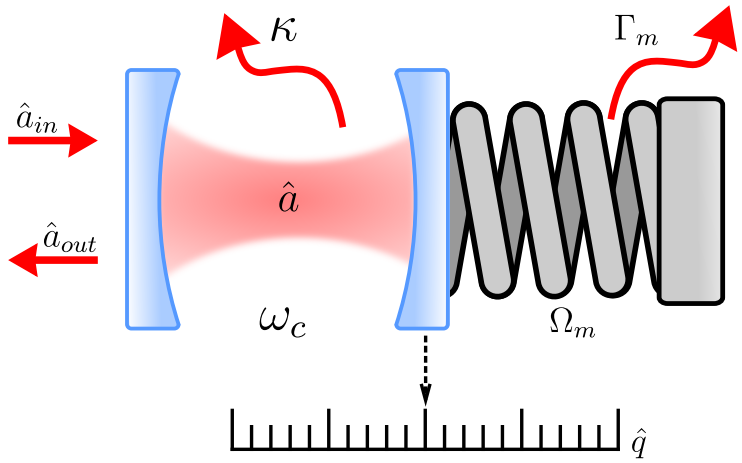

Figure 3.1: Scheme of the optomechanical interaction. The optical field $\hat{a}_{in}$ is coupled the optical cavity with resonance frequency ω_c and decay rate κ. Displacement of the mechanical oscillator $\hat{q}$ with resonance frequency Ω_m and decay rate Γ_m modifies the cavity resonance frequency and thus the intracavity field $\hat{a}$. The mechanical displacement transduced to the optical field is read out through the cavity output field $\hat{a}_{out}$.

So far, we do not see from the Eq. 3.1 interaction in between the optical cavity field and mechanical oscillator. It is introduced by considering a mechanical oscillator deforming the optical cavity by its motion. This means, that the mechanical displacement $\hat{q}$ of the oscillator mode is parametrically coupled to the optical energy stored inside the optical cavity, so the ω_c in Eq. 3.1 is no longer static, but it is a function of the oscillator displacement $\omega_c(\hat{q})$ instead.

The optical cavity resonant frequency can be Taylor expanded as $\omega_c(q) \approx \omega_c + q\partial\omega_c/\partial q + ...$ For a small mirror displacement compared to the cavity length L, keeping the terms to the first order provide a good approximation of the resonant frequency, so

$$\omega_c(\hat{q}) \approx \omega_c - G\hat{q}, \tag{3.2}$$

where we defined an optical frequency shift per displacement as $G = -\partial\omega_c/\partial x$. In case of a linear cavity $G = \omega_c/L$, where L is the cavity length. The whispering gallery mode resonators of radius R yield $G = \omega_c/R$. It is evident, that a cavity with shorter path length yield stronger optomechanical coupling.

The optical Hamiltonian can now be rewritten as

$$\begin{aligned} \hbar\omega_c\hat{a}^\dagger\hat{a} &\approx \hbar(\omega_c - G\hat{q})\hat{a}^\dagger\hat{a} \\ &= \hbar\omega_c\hat{a}^\dagger\hat{a} \underbrace{-g_0\hat{a}^\dagger\hat{a}(\hat{b} + \hat{b}^\dagger)}_{\hat{H}_{int}}, \end{aligned} \tag{3.3}$$

where we used the definition of position operator $\hat{q} = x_{zpf}(\hat{b} + \hat{b}^\dagger)$ and we defined the vacuum optomechanical coupling strength

$$g_0 = Gx_{zpf}, \tag{3.4}$$

which quantifies the coupling between single photon and single phonon. The Hamiltonian in Eq. (3.3) consists of a unperturbed optical Hamiltonian and interaction Hamiltonian $\hat{H}_{int}$ capturing coupling of the mechanical amplitude to the optical field.

3.1.1 Driven Hamiltonian in a rotating frame

Typically, the optomechanical coupling rate is much smaller than the cavity linewidth or mechanical frequency. This is commonly addressed by injecting a bright coherent field driving the optical cavity. The strongly driven cavity contains a large number of photons, greatly increasing the radiation pressure force and leading to an enhanced optomechanical coupling.

While expressing the driven optomechanical Hamiltonian, it is convenient to work in a reference frame rotating at the incident laser frequency ω_L eliminating fast oscillations in the Hamiltonian. It is done by unitary transformation $\hat{H} \rightarrow \hat{U}(\hat{H} - i\hbar\frac{\partial}{\partial t})\hat{U}^\dagger$, where $\hat{U} = \mathrm{e}^{i\omega_c t\hat{a}^\dagger\hat{a}}$. The full driven optomechanical Hamiltonian in the rotating frame reads

$$\hat{H} = \hbar\Omega_m\hat{b}^\dagger\hat{b} + \hbar\Delta_0\hat{a}^\dagger\hat{a} - \hbar g_0\hat{a}^\dagger\hat{a}(\hat{b} + \hat{b}^\dagger) + \hbar E\left(\hat{a}^\dagger + \hat{a}\right), \tag{3.5}$$

where we defined the laser drive detuning

$$\Delta_0 = \omega_c - \omega_L, \tag{3.6}$$

and E is a driving strength, related to the input laser power P as $|E| = \sqrt{2P\kappa/\hbar\omega_L}$.

3.1.2 Radiation pressure force

The coupling of the cavity radiation field to the mechanical motion lies at the core of cavity optomechanics. The interaction is provided by a radiation pressure force imposed on the mechanical element by a momentum transfer of photons. The radiation pressure force is given as the derivative of the interaction Hamiltonian with respect to position [23]

$$\hat{F} = \frac{d\hat{H}_{int}}{d\hat{q}} = \hbar G \hat{a}^\dagger \hat{a} = \hbar \frac{g_0}{x_{zpf}} \hat{a}^\dagger \hat{a}. \tag{3.7}$$

3.2 Quantum Langevin equations of motion

To study the dynamics of the optomechanical system, we introduce the Langevin equations of motion, which describe the time evolution of an open cavity optomechanical system [24]. They are stochastic differential equations containing both damping and random forces. As a consequence of coupling to the environment, the mechanical oscillator is damped with a rate Γ_m. This implies in accordance to the fluctuation-dissipation theorem, that the oscillator is also driven by a corresponding force - Brownian stochastic force represented by a noise operator $\hat{\xi}$. The noise operator $\hat{\xi}$ has a zero mean value and obeys the correlation function [25]

$$\langle \xi(t)\xi(t') \rangle = \frac{\Gamma_m}{\Omega_m} \int \frac{d\Omega}{2\pi} \mathrm{e}^{-i\Omega(t-t')} \Omega \left[\coth\left(\frac{\hbar\Omega}{2k_B T} \right) + 1 \right], \tag{3.8}$$

where k_B is the Boltzmann constant and T the temperature of environment. The noise operator $\hat{\xi}$ is non-Markovian i.e. δ correlated. However, the correlation function can be approximated in the classical limit as [21]

$$\langle \xi(t)\xi(t') \rangle = \Gamma_m \left[(2n_{th} + 1)\delta(t - t') \right]. \tag{3.9}$$

Similarly, the optical cavity decays at the rate κ and is driven by the radiation pressure of the input field represented by an annihilation operator

$\hat{a}_{in}$, whose correlations are given by

$$\langle \hat{a}_{in}(t)\hat{a}^{\dagger}_{in}(t')\rangle = (N(\omega_c)+1)\,\delta(t-t') \approx \delta(t-t'), \tag{3.10}$$

$$\langle \hat{a}^{\dagger}_{in}(t)\hat{a}_{in}(t')\rangle = (N(\omega_c))\,\delta(t-t') \approx 0, \tag{3.11}$$

where we assumed zero thermal occupancy of the optical field $N(\omega_c) \cong 0$. This assumption is valid for a high frequency optical fields at a room temperature and is assumed through out this thesis.

The quantum Langevin equation of motion for the optical and mechanical operators can be derived from the Hamiltonian 3.3 using the Heisenberg equation of motion $\frac{\partial}{\partial t}\hat{\mathcal{O}} = -\frac{i}{\hbar}[\hat{\mathcal{O}}, \hat{H}] + \hat{N}$, where the $\hat{N}$ represents the noise operator of the operator $\hat{\mathcal{O}}$. They read

$$\dot{\hat{a}} = -(\kappa + i\Delta)\hat{a} + ig_0\hat{a}\hat{q} + E + \sqrt{2\kappa}\hat{a}_{in}, \tag{3.12}$$

$$\dot{\hat{q}} = \Omega_m\hat{p}, \tag{3.13}$$

$$\dot{\hat{p}} = -\Omega_m\hat{q} - \Gamma_m\hat{p} + g_0\hat{a}^{\dagger}\hat{a} + \hat{\xi}. \tag{3.14}$$

The optical input field is usually coherently populated, so $\alpha_{in} = \langle \hat{a}_{in}\rangle \neq 0$. In general, the input field can couple to the cavity through several channels. We can distinguish the loss originating from the cavity driving κ_{ex} and other loss channels including the cavity absorption or scattering κ_0. This can be done with substitution [21]

$$\sqrt{2\kappa}\hat{a}_{in} \rightarrow \sqrt{2\kappa_{ex}}\hat{a}_{in} + \sqrt{2\kappa_0}\hat{a}_{vac}, \tag{3.15}$$

where the field entering from the loss channel $\hat{a}_{vac}$ is in vacuum state, so $\langle \hat{a}_{vac}\rangle = 0$.

3.3 Semi-classical dynamics

The Langevin equations can be simplified if we consider large number of intracavity photons. If the coherent driving is sufficiently strong, the system can be described by a semi-classical steady-state. We can split the optical field operator into a semi-classical steady state with small zero-mean fluctuations $\hat{a} \rightarrow \alpha_s + \delta\hat{a}$. To find the steady state we solve the Langevin equations with time derivatives set to zero, yielding

$$q = \frac{g_0|\alpha_s|^2}{\Omega_m}, \tag{3.16}$$

$$\alpha_s = \frac{E}{\kappa + i\Delta}. \tag{3.17}$$

The effect of the bright optical field inside the cavity is to steer the mechanical oscillator by radiation pressure to a new equilibrium position. This leads to definition of a new effective detuning

$$\Delta = \Delta_0 - \frac{g_0^2|\alpha_s|^2}{\Omega_m}. \tag{3.18}$$

Now, we will rewrite the Langevin equations for an operators fluctuations around the steady state we found. Furthermore, we rewrite the cavity field in terms of Hermitian amplitude $\hat{X}$ and phase $\hat{Y}$ quadrature operators yielding

$$\delta\hat{X} \equiv (\delta\hat{a} + \delta\hat{a}^\dagger)/\sqrt{2}, \qquad \delta\hat{Y} \equiv (\delta\hat{a} - \delta\hat{a}^\dagger)/i\sqrt{2}, \tag{3.19}$$

$$\delta\hat{X}_{in} \equiv (\delta\hat{a}_{in} + \delta\hat{a}_{in}^\dagger)/\sqrt{2}, \qquad \delta\hat{Y}_{in} \equiv (\delta\hat{a}_{in} - \delta\hat{a}_{in}^\dagger)/i\sqrt{2}, \tag{3.20}$$

where the $\hat{X}_{in}$ and $\hat{Y}_{in}$ are corresponding Hermitian input noise operators. Finally, we arrive at the linearised equations by neglecting non-linear terms, which is valid assumption in case of a strong optical probe i.e. $|\alpha| \gg 1$

$$\delta\dot{\hat{X}} = -\kappa\delta\hat{X} + \Delta\delta\hat{Y} + \sqrt{2\kappa}\hat{X}_{in}, \tag{3.21}$$

$$\delta\dot{\hat{Y}} = -\kappa\delta Y - \Delta\delta X + g\delta\hat{q} + \sqrt{2\kappa}\hat{Y}_{in}, \tag{3.22}$$

$$\delta\dot{\hat{q}} = \Omega_m\delta\hat{p}, \tag{3.23}$$

$$\delta\dot{\hat{p}} = -\Omega_m\delta\hat{q} - \Gamma_m\delta\hat{p} + g\delta\hat{X} + \hat{\xi}. \tag{3.24}$$

The equations show, that the mechanical mode is coupled to the cavity mode phase fluctuation quadrature by the effective optomechanical coupling

$$g = g_0\sqrt{2}\alpha_s = \frac{2\omega_c}{L}\sqrt{\frac{\kappa P_{in}}{m_{eff}\Omega_m\omega_c(\kappa^2 + \Delta^2)}}, \tag{3.25}$$

which is boosted by the intracavity field amplitude α_s.

3.3.1 On resonance driving

In this section, we present the solution to the linearised Langevin equation with on resonance driving, meaning that the detuning $\Delta = 0$. On resonance driving is done experimentally by tuning the driving laser frequency ω_L or by tuning the cavity length L. From Eqs. 3.21 and 3.22 we can notice, that by zero detuning the stochastic equations describing the optical amplitude and phase are decoupled. This is not the case for equations 3.23 and 3.24

describing the harmonic oscillator, but they can be combined into a single second-order differential equation reading

$$\delta\ddot{\hat{q}} + \Gamma_m \delta\dot{\hat{q}} + \Omega_m^2 \hat{q} = \Omega_m \hat{\xi} - g\Omega_m \delta\hat{X}. \tag{3.26}$$

It is straightforward to solve the resulting set of equations in frequency domain by Fourier transform. From the partial differential equations we get algebraic equations with solutions:

$$\delta\hat{X}(\Omega) = \frac{\sqrt{2\kappa}\hat{X}_{in}(\Omega)}{\kappa - i\Omega}, \tag{3.27}$$

$$\delta\hat{Y}(\Omega) = \frac{\sqrt{2\kappa}\hat{Y}_{in}(\Omega) + 2g\delta\hat{q}(\Omega)}{\kappa - i\Omega}, \tag{3.28}$$

$$\delta\hat{q}(\Omega) = \chi_m(\Omega)\left(\hat{\xi}(\Omega) + \frac{2g\sqrt{2\kappa}\delta\hat{X}(\Omega)}{\kappa - i\Omega}\right), \tag{3.29}$$

where $\chi_m(\Omega)$ is the mechanical susceptibility defined as

$$\chi_m(\Omega) = \frac{\Omega_m}{\Omega_m^2 - \Omega^2 + i\Gamma_m\Omega}. \tag{3.30}$$

Substituting the optical amplitude quadrature from Eq. 3.27 into Eq. 3.29, we get expression for the mechanical position

$$\delta\hat{q}(\Omega) = \chi_m(\Omega)\left(\hat{\xi}(\Omega) - \sqrt{4\Gamma_m C_{eff}}\hat{X}_{in}(\Omega)\right), \tag{3.31}$$

where we defined the *effective optomechanical cooperativity*

$$C_{eff}(\Omega) \equiv \frac{C}{(1 - 2i\Omega/\kappa)^2}, \tag{3.32}$$

with C being the *optomehanical cooperativity*

$$C \equiv \frac{4g^2}{\kappa\Gamma_m}. \tag{3.33}$$

3.3.2 Mechanical power spectral density

The power spectral density of the mechanical displacement is derived from the Eq. 3.31. While assuming that the optical and mechanical baths are independent, we find

$$\begin{aligned} S_{qq} &= \int_{-\infty}^{\infty} \langle \delta\hat{q}(\Omega)\delta\hat{q}(\Omega'\rangle \, d\Omega' \\ &= |\chi_m|^2 \left(2\Gamma_m(n_{th}+1) + 4\Gamma_m|C_{eff}(\Omega)|S_{x_{in}x_{in}}\right), \end{aligned} \tag{3.34}$$

where we used the following correlations in the frequency domain for the thermal force operator

$$\langle\hat{\xi}(\Omega)\hat{\xi}(\Omega')\rangle = 2\Gamma_m(n_{th}+1)\delta(\Omega+\Omega'), \tag{3.35}$$

$$\langle\hat{\xi}(-\Omega)\hat{\xi}(\Omega')\rangle = 2\Gamma_m(n_{th}+1)\delta(\Omega-\Omega'). \tag{3.36}$$

The first term in Eq. 3.34 is due to the thermal bath driving with the thermal noise spectrum given by

$$S_{FF}^{th} = \int_{-\infty}^{\infty} \langle\hat{\xi}(\Omega)\hat{\xi}(\Omega')\rangle \, d\Omega' = 2\Gamma_m(n_{th}+1). \tag{3.37}$$

The second term in Eq. 3.34 is a contribution from the optical field back-action, driving the mechanical oscillator by the radiation pressure. The back-action noise spectral density is given by

$$S_{FF}^{ba} = 4\Gamma_m \frac{C}{1-\Omega^2/\kappa^2} = 4\Gamma_m|C_{eff}(\Omega)|. \tag{3.38}$$

Taking the noise spectra above, we can rewrite the power spectra density of the mechanical displacement as

$$S_{qq} = |\chi_m|^2 \left(S_{FF}^{th} + S_{FF}^{ba}\right). \tag{3.39}$$

3.4 Input-output relation

In the previous sections, we studied the optomechanical interaction from the intracavity field point of view. While the intracavity field is responsible for the optomechanical interaction, it is not experimentally accessible. Therefore, we need to find relations in between experimentally accessible input and output fields and the studied intracivity field. The linking element is provided by the *input-output* formalism. For a single-sided optical cavity it gives [26]

$$\hat{a}_{out}(t) = \sqrt{2\kappa}\delta\hat{a}(t) - \hat{a}_{in}(t), \tag{3.40}$$

which can be translated to the field amplitude and phase quadratures as

$$\hat{X}_{out}(\Omega) = \sqrt{2\kappa}\delta\hat{X}(\Omega) - \hat{X}_{in}(\Omega), \tag{3.41}$$

$$\hat{Y}_{out}(\Omega) = \sqrt{2\kappa}\delta\hat{Y}(\Omega) - \hat{Y}_{in}(\Omega). \tag{3.42}$$

Using the input-output formalism given be the equations above, we translate the intracavity amplitude and phase fluctuations given by Eqs. 3.27 and 3.28

to the output quadratures:

$$\delta\hat{X}_{out}(\Omega) = -\frac{\kappa + i\Omega}{\kappa - i\Omega}\hat{X}_{in}, \tag{3.43}$$

$$\delta\hat{Y}_{out}(\Omega) = -\frac{\kappa + i\Omega}{\kappa - i\Omega}\hat{Y}_{in} - 2\sqrt{\Gamma_m C_{eff}}\delta\hat{q}(\Omega) \tag{3.44}$$

$$= -\frac{\kappa + i\Omega}{\kappa - i\Omega}\hat{Y}_{in} - 2\sqrt{\Gamma_m C_{eff}}\chi_m\left[\hat{\xi}(\Omega) + 2\sqrt{\Gamma_m C_{eff}}\hat{X}_{in}(\Omega)\right]. \tag{3.45}$$

We see, that with on resonance driving ($\Delta = 0$), the information about the mechanical displacement is fully imprinted to the phase quadrature of the output field. The magnitude of the optomechanical transduction is determined by the characteristic measurement rate [21]

$$\mu = \Gamma_m|C_{eff}| = \Gamma_m\frac{C}{1 + 4(\Omega/\kappa)^2}. \tag{3.46}$$

In the *sideband unresolved* ("bad cavity") regime, where $\Omega \ll \kappa$, the characteristic rate can be approximated as $\mu = 4g^2/\kappa$. Contrary, in the case of *sideband resolved* regime $\Omega/\kappa \to \infty$ so $\mu \to 0$ and the information about mechanical motion imprinted to the optical field become asymptotically small. This is important in the feedback cooling chapter, as the feedback cooling relies on the measurement rate being sufficiently large compared to the system decoherence rate $\Gamma_{th} = \Gamma_m n_{th}$ [27].

Information about the mechanical displacement can be extracted from the optical phase quadrature with homodyne detection. The detected mechanical position $\delta\hat{q}_{det}$ obtained by renormalising the output phase quadrature given by Eq. 3.44 to the mechanical displacement units reads

$$\delta\hat{q}_{det} \equiv \frac{\hat{Y}_{out}(\Omega)}{2\sqrt{\Gamma_m C_{eff}}} \tag{3.47}$$

$$= \underbrace{\delta\hat{q}^0(\Omega)}_{\text{mechanics}} \underbrace{- \frac{1}{2\sqrt{\Gamma_m C_{eff}}}\left(\frac{\kappa + i\Omega}{\kappa - i\Omega}\right)\hat{Y}_{in}(\Omega)}_{\text{measurement noise}} - \underbrace{2\sqrt{\Gamma_m C_{eff}}\chi(\Omega)\hat{X}_{in}(\Omega)}_{\text{back-action noise}}. \tag{3.48}$$

From the result above we see that the mechanical displacement measurement is affected by both the measurement noise arising from the input field phase fluctuations and the back-action noise from fluctuations of the probe beam amplitude quadrature.

Chapter 4

Experimental techniques and assemblies

4.1 On-chip membrane oscillator

The mechanical oscillator utilized in the feedback cooling experiment is an on-chip, stressed silicon nitride (Si_3N_4), nanogram-scale tethered membrane. Through the thin and ultra-stressed membranes design, a low dissipation rate and thus a large mechanical quality factor $Q_m \approx 1 \cdot 10^7$ is achieved for a fundamental mode with resonance at $\Omega_m \approx 130\,\mathrm{kHz}$.

Figures of merit of the optomechanical device

- The necessary condition for observing quantum effects is that the $Q_m \cdot f_m$ product ($f_m = \Omega_m/2\pi$) is sufficiently large, thus the quality factor and resonant frequency are the most important parameters of the mechanical oscillator we are considering [28]. How large the $Q_m \cdot f_m$ needs to be depends on the system and the protocol to be implemented. Generally, it is required, that the oscillator undergoes many cycles before one thermal phonon joins the system. This condition means that the decoherence rate Γ_{dec} must satisfy [29]

$$\Gamma_{dec} = \Gamma_m n_{th} < \Omega_m, \tag{4.1}$$

  where the phonon occupancy equals $n_{th} \sim k_B T/\hbar\Omega_m$ in the limit of high temperature T and $\Gamma_m = \Omega_m/Q_m$. The, same condition can be rewritten as

$$Q_m \cdot f > k_B T/h \approx 6 \cdot 10^{12}, \tag{4.2}$$

  where we considered $T = 300\,K$. Finally, the necessary condition for a ground state cooling is often expressed as $Q_m > n_{th}$ [30, 31].

- The mechanical frequency normalized to the optical cavity linewidth

$$\overline{\Omega}_m = \frac{\Omega_m}{\kappa} \tag{4.3}$$

  is used to distinguish between the "good cavity" (sideband resolved) regime when $\overline{\Omega}_m > 1$ and a "bad cavity" (sideband unresolved) regime when $\overline{\Omega}_m < 1$. The feedback cooling of the mechanical oscillator is most effective in the sideband-unresolved regime (see sec. 3.4) [32]. Given the linewidth of our optical cavity $\kappa \sim 3 \cdot 10^9$, this condition is easily satisfied for a fundamental mode.

- The zero point motion $x_{zpm} = \sqrt{\hbar/2m_{eff}\Omega_m}$ depends on the effective mass m_{eff} and the mode resonance frequency. The x_{zpm} should be as large as possible to maximize the optomechanical coupling, it is therefore desirable to work with an oscillator with a small effective mass.

Quality factor

The loss of mechanical excitations is quantified by the energy dissipation rate $\Gamma_m = \Omega_m/Q_m$ [23]. The quality factor Q_m corresponds to the ratio of stored energy versus lost energy during one cycle of vibration. The overall quality factor of the oscillator is given as

$$\frac{1}{Q_{tot}} = \sum \frac{1}{Q_i}, \tag{4.4}$$

where Q_i corresponds to individual loss channels. This relation shows that the Q_{tot} will be limited by the predominant loss channel. The main loss mechanisms are listed bellow.

- *Gas damping* losses are caused by the interaction with the surrounding gas atoms. In the high pressure environment surrounding gas acts like a *viscous* force damping the oscillator [33]. The air damping is not a limiting factor to us, as it can be minimized in a low pressure environment provided by a vacuum chamber, as discussed in section 4.1.2.

- *Acoustic radiation* losses are caused by the dissipation of the elastic waves into the substrate and possibly to the oscillator supporting structures such as a sample holder [34]. The design of the tethered membrane minimizes the radiation loss by creating a large mismatch between the membrane and the substrate [14]. Other succesful designs minimizing the dissipation involve *phononic shielding* by periodic structures creating bandgaps in the phonon dispersion [13, 35, 36].

- *Intrinsic damping* losses relate to the material properties. High stresses in the material have been shown as an important factor enhancing the Q_m [37]. The intrinsic losses are dominating when the resonator is perfectly decoupled from the environment. As the air damping is easily removed in a vacuum chamber and clamping losses are minimized by optimizing the oscillator geometry, the intrinsic losses are dominating in the case of tethered membranes.

4.1.1 Fabrication

We adapted the design of the mechanical resonators from the Gröblachers group. The fabrication of the samples used in this thesis was done at DTU facilities (DTU Danchip) by the the PhD student Dennis Høj with help of cleanroom engineer Kristian Hagsted Rasmussen following the R. Norte recipe [14].

Dennis Høj customized the membrane parameters to be the best suitable for our experiment. The dimensions of the sample used for a feedback cooling experiment are highlighted in figure 4.3.

4.1.2 Mechanical properties

The mode spectrum of the tethered membrane is shown in figure 4.1. The effective mass of the modes is inferred from a finite element simulation in COMSOL. The effective mass of the fundamental mode at $\Omega_m \approx 134\,\mathrm{kHz}$ yields $m_{eff} = 3.56\,\mathrm{ng}$.

Ring-down measurement

Due to the narrow linewidth of the resonance modes and limited resolution of the spectrum analyser we use ($\mathrm{RBW}_{\min} = 1\,\mathrm{Hz}$) we use a transient measurement to estimate the dissipation rate and consequently the quality factor of the resonant modes. The trajectory of a damped oscillator with resonant mode frequency Ω_m and initial phase φ_0 is given as

$$x(t) = x_0 \exp(-t/\tau) \cos(\Omega_m t + \varphi_0), \tag{4.5}$$

where x_0 is an initial amplitude and $\tau = 2/\Gamma_m$ is a time constant, with Γ_m the damping rate. By substituting the quality factor $Q = \Omega_m/\Gamma_m$ to the equation above we get

$$x(t) = x_0 \exp\left(-\frac{\Omega_m t}{2Q}\right) \cos(\Omega_m t + \varphi_0), \tag{4.6}$$

where the exponential term corresponds to the decaying envelope. The mechanical motion is transduced to the phase of the laser probe beam reflected from the membrane through the optomechanical coupling, which allows the detection of the damped motion.

The optical setup for a ring-down measurement, shown in figure 4.2, is an optical-fibre based interferometer, with a free-space part for probing the oscillations of the membrane. The experiment is sourced by a fibre coupled laser (Pure Photonics PPCL500), which is split on a fibre coupler to the signal and local oscillator (LO) paths. The signal arm is routed through an amplitude modulator (Thorlabs LN82S-FC) to a circulator (Thorlabs 6015-3-APC) and outcoupled to the free-space. The beam is then focused with an aspheric lens (f=9.9 mm) to the membrane, placed inside the vacuum chamber. The mechanical oscillations are imprinted in the phase of the reflected probe beam which is collected through the fibre in/out coupling lens and

separated from the incident beam on the circulator. Afterwards, the signal is interfered with the LO on a balanced fibre beam-splitter connected to the homodyne detector (HD). The phase between the interfering beams is actively stabilized with a feedback loop actuating phase shifter (fibre stretcher) maintaining a $\pi/2$ relative phase difference corresponding to the phase quadrature measurement. The error signal is derivated from a DC part of the HD output signal, while the AC part containing information of the mechanical signal is measured via an electronic spectrum analyser (ESA, Agilent N9000A).

Wile the vacuum chamber is pumped down to pressure $P \sim 3 \cdot 10^{-7}$ mbar, we measure the power spectra density of the trampoline Brownian motion. To measure the ring-down time, we resonantly excite the mechanical mode by the radiation pressure of the intensity modulated probe beam. Practically, we send a harmonic signal at a frequency corresponding the resonant frequency of the mechanical mode Ω_m from a function generator to the amplitude modulator and monitor the HD output on the ESA set to the zero-span mode with RBW filter centred at Ω_m. When the amplitude of the membrane motion reaches its maximum, the driving force (amplitude modulation) is switched off and the oscillator amplitude decays to the steady-state. The ring-down data of the fundamental mode is shown in figure 4.2.

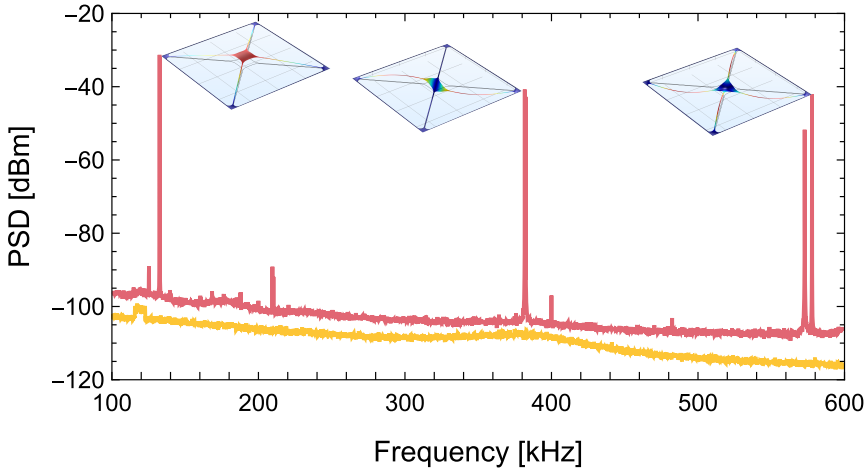

Figure 4.1: Mode spectrum of the trampoline oscillator. Plot shows the power spectral density of the Brownian noise (red trace), detection noise (yellow trace) and the mode shape obtained from COMSOL.

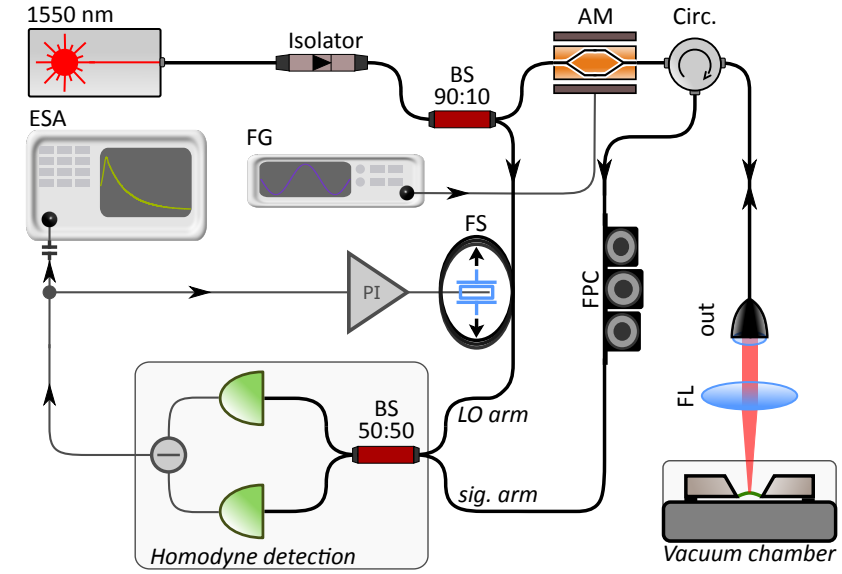

(a)

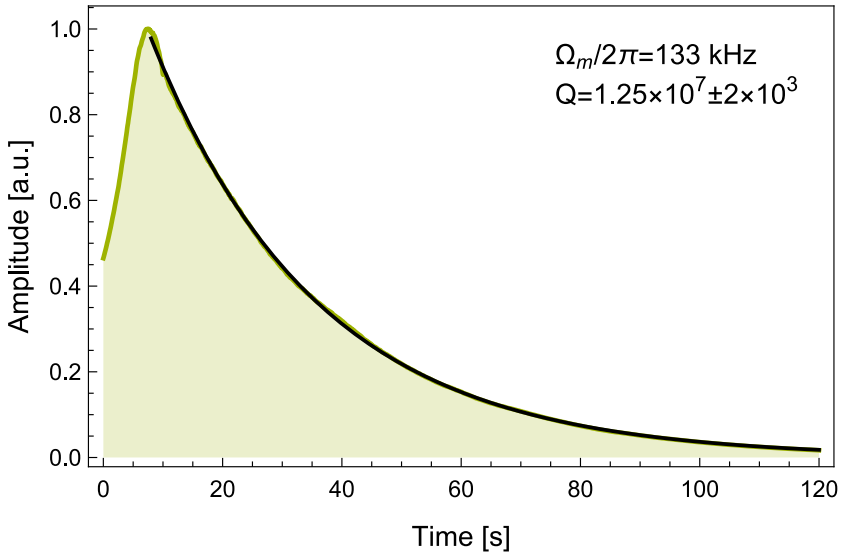

(b)

Figure 4.2: Ring-down measurement of the fundamental mode. (a) Schematic of the measurement setup. BS: beamsplitter, AM: amplitude modulator, Circ.: circulator, out: fibre in/out coupler, FL: focussing lens, FPC: fibre polarization controller, PI: proportional integral controller (servo), FG: function generator, ESA: electronic spectrum analyser. (b) Ring-down of the fundamental vibration mode $\Omega_m = 133\,\mathrm{kHz}$ of the tethered membrane. Data (green trace) measured with ESA in zero-span mode and RBW 5 Hz are fitted with function 4.6 (black line) yielding the mechanical quality factor Q of $1.25 \cdot 10^7$.

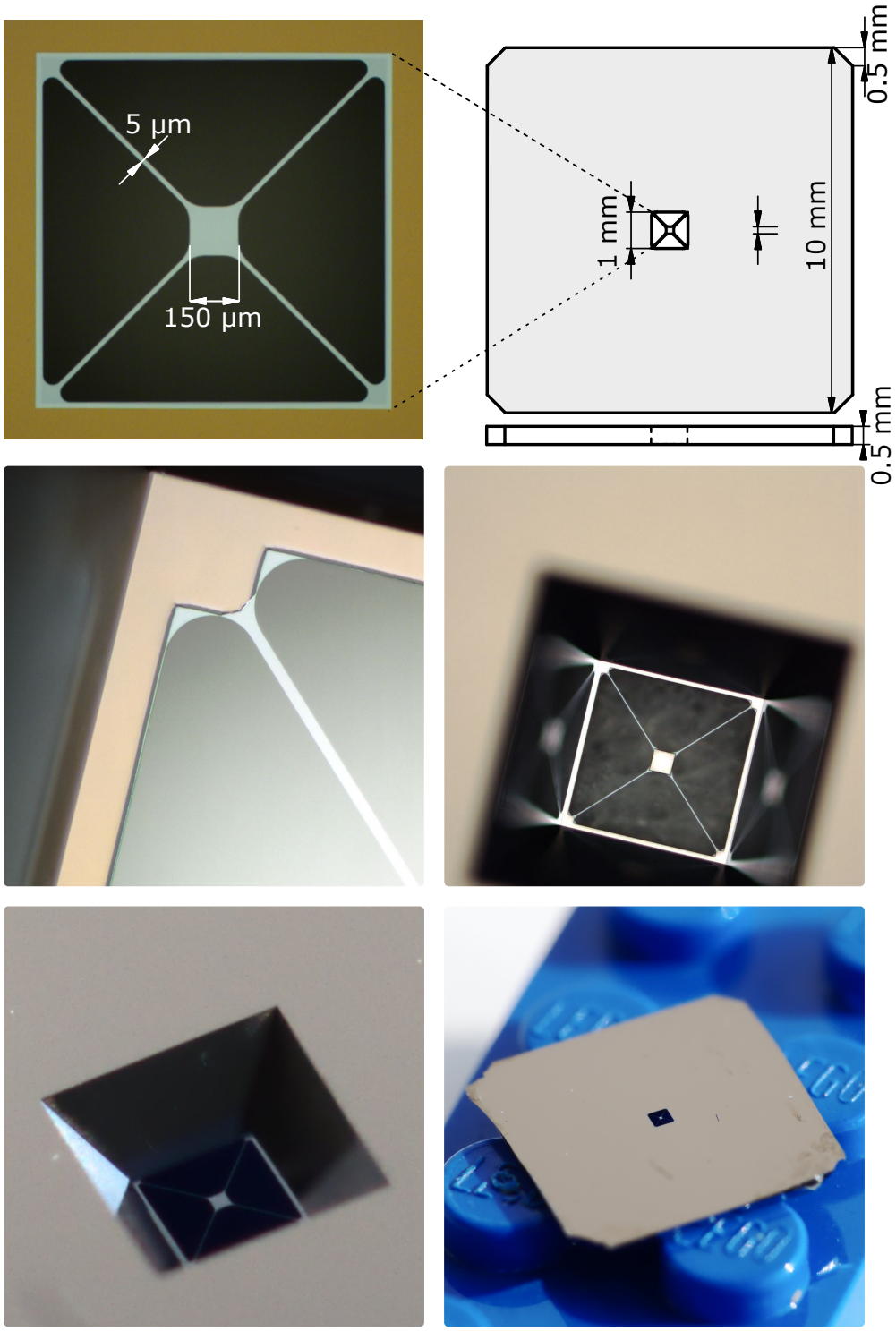

Figure 4.3: (top) Dimensions of the tethered-membrane used in a feedback cooling experiment (middle, bottom) Pictures of the chip with suspended membrane. The tethered-membrane is also referred as *trampoline* [15], which is fairly justified by the pictures.

Using the same setup, we measured dependency of the mechanical quality factor Q_m on the pressure. The results are shown in figure 4.4.

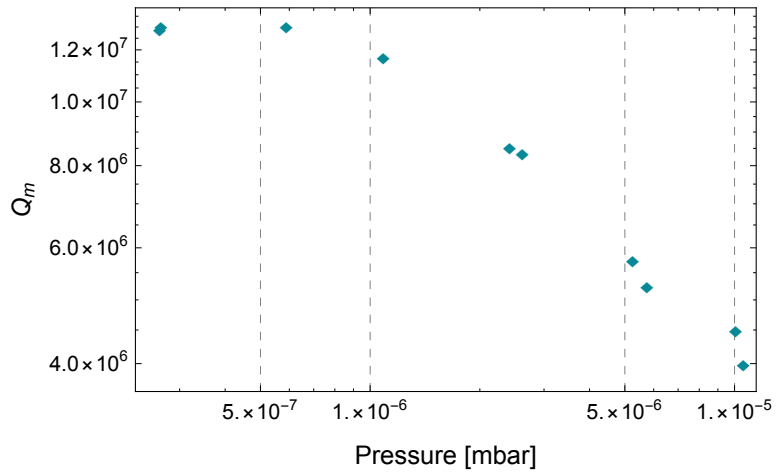

Figure 4.4: The mechanical quality factor of the fundamental mode as a function of pressure. The quality factor starts to saturate at pressures lower than $1 \cdot 10^{-6}$ mbar. At pressures below $5 \cdot 10^{-7}$ mbar the quality factor is completely saturated, meaning that that the dissipation rate is dominated by other loss mechanisms than air damping.

4.2 Optical resonator

An optical resonator (cavity) can confine and store electromagnetic (EM) fields at some specific frequencies for a given time. The EM field "fitting" to the cavity is referred as a cavity mode and its frequency is referred as a resonant frequency. The most basic example of the optical resonator - so called Fabry Pérot (FP) resonator, FP cavity or FP etalon - is formed by two parallel mirrors facing each other. Other types of resonators exist. Examples of resonators consisting of more than two mirrors is ring resonators and bow-tie resonators.

In this thesis, the F.P. type of resonator and microtoroid type of resonator are used. The microtoroid resonator is a type of dielectric resonator which makes use of the total internal reflection at the boundary of two low-loss mediums with different optical density. The microtoroids are types of whisper-gallery modes resonators [38].

Resonance condition

In general, the cavity modes are found as a solution of Maxwell equations with appropriate boundary conditions [39]. Here, we consider a simple F.P. resonator formed by two mirrors separated by distance L. The monochromatic wave with wavelength $\lambda = 2\pi c/\omega$ and complex amplitude $U(\mathbf{r})$ incident on one of the mirrors has a form

$$E(\mathbf{r}, t) = U(\mathbf{r}) \exp(i\omega t). \tag{4.7}$$

For loss-less planar mirrors, the boundary conditions dictate that the transverse components of the electric field must be equal to zero at the mirror surfaces, so $U(\mathbf{r}) = 0$ at $z = 0$ and $z = L$, where z is the longitudinal propagation direction of the wave. The solution of the Maxwell (Helmholtz) equation satisfying those boundary condition can be found in a form of standing waves $U(\mathbf{r}) = A \sin(kz)$, where A is a constant and $kL = q\pi$, where q is an integer. This condition yields, that only frequencies satisfying $\nu_q = q\frac{c}{2L}$ are resonant with the cavity. Frequency separation of two adjacent frequencies is called free spectral range and for a FP cavity reads

$$FSR_{FP} = \frac{\Delta\omega_{FSR}}{2\pi} = \frac{c}{2L}. \tag{4.8}$$

Note, that for a toroidal cavity considered in the magnetometry chapter

$$FSR_{tor} = \frac{c}{L}. \tag{4.9}$$

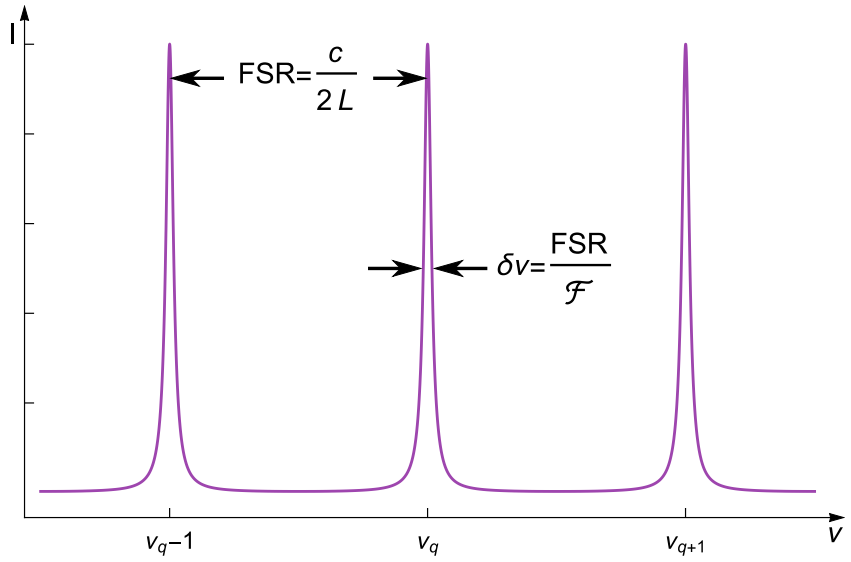

Figure 4.5: Longitudinal modes of the optical resonator.

Effect of optical loss

In reality, mirrors are never perfectly reflective (which is essential to couple the light to the cavity in the first place). We consider mirrors with the intensity reflection coefficients R_1 and R_2. Then, the round-trip amplitude attenuation factor equals to $h = |r| \exp(-i\phi)$, where $r = \sqrt{R1R2}$. After n round trips the complex amplitude becomes

$$U = \sum_n h^n U_0 = \frac{U_0}{1-h}. \tag{4.10}$$

The intensity of the light in the resonator after substituting for h yields

$$I = |U|^2 = \frac{I_{max}}{1 + (2 * \mathcal{F}/\pi)^2 \sin^2(\pi\nu/FSR)}, \tag{4.11}$$

$$I_{max} = \frac{I_0}{(1-|r|)^2}, \tag{4.12}$$

where $I_0 = |U_0|^2$ is the incident intensity and $\mathcal{F}$ is the cavity finesse

$$\mathcal{F} = \frac{\pi\sqrt{r}}{1-|r|} = \frac{\pi\sqrt[4]{R1R2}}{1-\sqrt{R1R2}}. \tag{4.13}$$

In the usual case of a high finesse cavity $\mathcal{F} \gg 1$ the spectral width $\delta\nu$ of the individual resonator mode is

$$\delta\nu = \frac{\kappa}{2\pi} \approx \frac{FSR}{\mathcal{F}}, \tag{4.14}$$

where κ is the cavity loss rate. In analogy to the mechanical oscillator we can define cavity quality factor as

$$Q_{cav} = \frac{\omega_{cav}}{\kappa}. \tag{4.15}$$

As illustrated in figure 4.5, the losses relax the strict resonant frequency condition. The cavity with lower quality factor yields broader resonances.

Photon lifetime

We can define the photon lifetime, or photon survival time from a photon survival probability P_S. For cavity mirrors with reflectance $R_{1,2}$ the photon survival probability is given by

$$P_S = R_1 R_2. \tag{4.16}$$

The probability that the photon is lost during one round trip is simply $1-P_S$. This treatment can be generalized considering other sources of losses that occur at discrete locations ("lumped losses"). As the time for a photon roundtrip is given as $\tau_{rt} = 1/FSR$, the lifetime of a photon inside the cavity τ_P is a product of the roundtrip time and the average number of round trips that the photon survives

$$\tau_P = \frac{1}{FSR(1 - P_S)}. \tag{4.17}$$

Cavity coupling regimes

The cavity total loss rate can be broken down to the component associated with the light incoupling (outcoupling) κ_{ex} and a second component attributed to the internal losses κ_0

$$\kappa = \kappa_{ex} + \kappa_0. \tag{4.18}$$

We distinguish three coupling regimes with regard to the losses distribution. The cavity is said to be:

- *Undercoupled*: when $\kappa_0 \gg \kappa_{ex}$. In the undercoupled regime the total losses are dominated by the cavity intrinsic losses. This regime is usually undesirable as it leads to en effective loss of information [23]. However, we employed this regime in a squeezing-enhanced magnetometry experiment, as we tried to minimize the overall losses acting on the squeezed light probe (including the incoupling losses) [40].

- *Overcoupled*: when $\kappa_{ex} \approx \kappa \gg \kappa_0$. In this regime the photons emerges from the cavity without being absorbed or transmitted through the second mirror.

- *Critically coupled*: when $\kappa_{ex} = \kappa_0$. In the critically coupled (impedance matched) regime, all incoupled light is either dissipated inside the resonator or transmitted.

Resonator eigenmodes

In the previous section we found longitudinal (axial) modes of the linear resonator. Now we consider the resonance frequency and spatial intensity distribution. We drop the assumption that the cavity is formed by plane mirrors. In that configuration the resonator is marginally stable [38], which require both mirrors to be perfectly parallel to each other and that the incident beam is perfectly aligned with the optical axis, otherwise the modes decouple from the cavity after a number of round trips. Instead, we consider the more relevant case to this work that the cavity is formed by spherical mirrors with radius of curvature $R_{C_{1,2}}$. For a plane mirror $R_C = \infty$, concave a convex mirrors yield $R_C < 0$ and $R_C > 0$ respectively. The stable resonator is formed when

$$0 \leq g1g2 \leq 1 \tag{4.19}$$

is satisfied, where, $g_{1,2} = 1 + L/R_{C_{1,2}}$. Saturating this inequality yields a marginally stable resonator as mentioned above. The solution to the Helmholtz equation with boundary condition given by a spherical mirrors can be described by Hermite-Gaussian (H-G) modes [41]

$$E_{m,n}(\mathbf{r}, \mathbf{t}) = E_0 X_m(x, z) Y_n(y, z) \exp\left(-ik(z - L/2)\right) \exp\left(i\omega t\right) + c.c., \tag{4.20}$$

$$X_m(x, z) = \frac{w_0}{\sqrt{w(z)}} H_m\left(\frac{\sqrt{2x}}{w(z)}\right) \exp\left(-\frac{x}{2}w^2(z) - i\frac{kx^2}{2R(z)} + i\frac{2m+1}{2}\Psi(z)\right), \tag{4.21}$$

$$Y_n(y, z) = \frac{w_0}{\sqrt{w(z)}} H_n\left(\frac{\sqrt{2y}}{w(z)}\right) \exp\left(-\frac{y}{2}w^2(z) - i\frac{ky^2}{2R(z)} + i\frac{2n+1}{2}\Psi(z)\right), \tag{4.22}$$

where

$$\begin{aligned} w(z) = w_0\sqrt{1+\left(\frac{z}{z_R}\right)^2} &: \text{mode radius} \\ w_0 &: \text{mode waist} \\ z_R = \frac{\pi}{\lambda}w_0^2 &: \text{Rayleigh length} \\ R(z) = z\left[1+\left(\frac{z_R}{z}\right)^2\right] &: \text{wavefront curvature} \\ \Psi(z) = \arctan\left(\frac{z}{z_R}\right) &: \text{Guoy phase} \end{aligned} \tag{4.23}$$

The $H_m\left(\sqrt{2}\frac{x}{w}\right)$ and $H_n\left(\sqrt{2}\frac{y}{w}\right)$ are Hermite polynomials of order m and n and resulting cavity modes are referred as transverse electro magnetic modes of order m and n, i.e. $\mathrm{TEM_{mn}}$. In order to be resonant with the cavity, the Hermite-Gaussian beam wavefront curvature $R(z)$ must match the radius of curvature of the cavity mirrors R_c. From Eq. 4.20 we see that the $R(z)$ does not depend on a mode numbers, thus a resonator with a given geometry supports $\mathrm{TEM_{mn}}$ modes independent of m and n. The same equations show that a Guoy phase is dependent on a mode numbers. As a consequence, the resonant frequency is generally non-degenerate for H-G modes and depends on a mode numbers as follows [41]

$$\nu_{l,m,n} = \frac{c}{2L}\left[l + \frac{1+m+n}{\pi}\arccos\left(\pm\sqrt{g_1 g_2}\right)\right], \tag{4.24}$$

where l is a longitudinal mode number and m, n are transverse mode numbers. We are mostly interested in the fundamental mode $\mathrm{TEM_{00}}$ - Gaussian mode, as it has the most uniform intensity distribution and because the higher order modes are associated with losses. Recalling that $H_0(x) = 1$ we can write the electric field of a Gaussian beam as

$$E_{Gb}(r,z) = E_0\frac{w_0}{w(z)}\exp\left(-\frac{r^2}{w^2(z)} - i\frac{kr^2}{2R(z)} + i\Psi(z)\right)\exp(-ik(z-L/2)+c.c. \tag{4.25}$$

where $r^2 = x^2 + y^2$. We refer to the overlap between the Gaussian beam and the cavity mode as a cavity mode-matching (MM). To achieve the maximal possible mode-matching, a set of mode-matching lenses is used to form the input beam parameters.

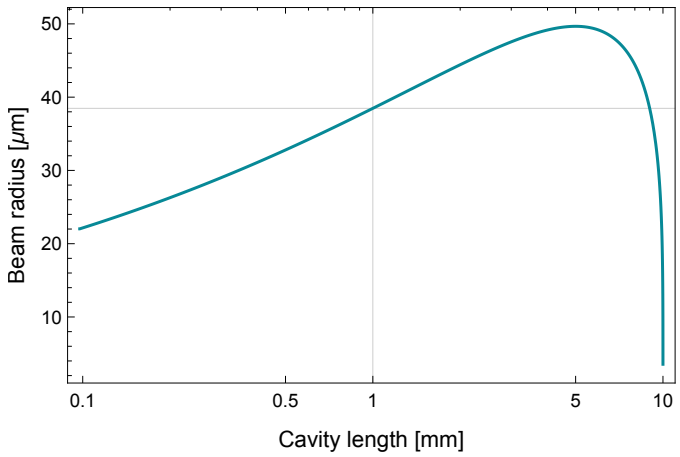

(a)

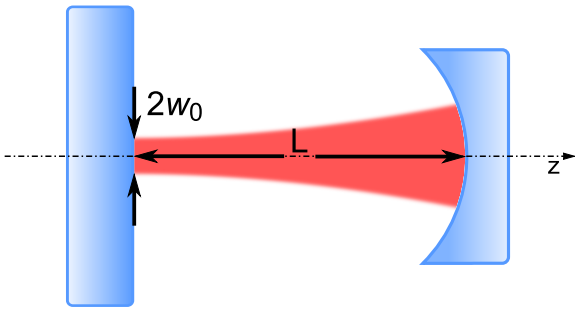

(b)

Figure 4.6: (a) Input beam waist as a function of the cavity length obtained from Eq. 4.26. (b) For a hemispherical cavity, the Gaussian beam waist is in a position of the plane mirror. The beam wavefront radii of curvature at a waist position $R(z_{w0}) \to \infty$. The spherical mirror is in position where the beam wavefront curvature match the mirror radius of curvature $R(z) = R_c$.

4.2.1 Optical cavity design

The optical cavity for a feedback cooling experiment is an approximately 1 mm long, linear, hemispherical cavity. The main requirements on the cavity geometry are that the cavity needs to be suitable to accommodate the on-chip oscillator with maximal spatial overlap in between the optical mode and oscillator vibrational mode. From a construction point of view, the cavity needs to be stable and able to operate under high (HV) or ultra-high (UHV)

vacuum conditions.

Design of the prototype cavity - the cavity used in this work - reflects the following reasoning. The choice of hemispherical geometry is given by the way we place the on-chip mechanical oscillator inside the cavity. To avoid possible losses to the oscillator quality factor due to the chip clamping [36], we keep the possibility of holding the chip inside the cavity by gravity. Therefore, the cavity is oriented vertically (optical axes of the cavity is perpendicular to the optical table) and the chip is supported by a bottom - plane cavity mirror ($R_c = \infty$). The second mirror is a concave spherical mirror ($R_c = -10mm$) enhancing the resonator stability. The short cavity length provides a large frequency pull parameter $G \sim 1/L$. When we fix the radius of curvature of the cavity mirrors, we can calculate the input beam waist as a function of the cavity length L. Using the relations given in Eq. 4.23, the input waist w_0 must satisfy

$$w_0^2 = \frac{\lambda}{\pi}\sqrt{(R_c - L)L}. \tag{4.26}$$

The minimal cavity length is constrained by the dimensions of the chip and mirrors and yields $L_{min} \sim 0.8\,\mathrm{mm}$. There is an another constrain on the input beam waist, as it must overlap with the $150\,\mu m \times 150\,\mu m$ trampoline oscillator pad. Input beam waist as a function of the cavity length is shown in a figure 4.6(a). The designed length $L = 1\,mm$ yields the input beam waist $w_0 \approx 38.5\,\mu m$ and $g_1 g_2 = 0.9$ which satisfy the stability condition defined in Eq. 4.19.

Optomechanical cavity assembly

The render of the optomechanical cavity is shown in figure 4.7. Materials and components used as cavity parts need to be suitable for usage under a high vacuum. In general, we need to avoid materials with high a rate of outgassing in vacuum. Common choice of vacuum compatible material is a stainless steel or aluminium/aluminium alloys. We are using commercially available components graded for a HV usage and custom made stainless steel parts.

The cavity incoupling plane mirror is attached to the cavity structural plate and held on a place by a clamp. The fluorocarbon (Viton) o-ring is fitted in between the mirror and the clamp. The square cut-out at the top of the plate allows to align the oscillator chip on the mirror with a precision of $\pm 0.1\,\mathrm{mm}$. Furthermore, the cavity structural cylinder is attached to this plate.

For a precise control of the resonator length the spherical mirror is attached to a low voltage piezo actuator (Piezomechanik HPSt). The actuator

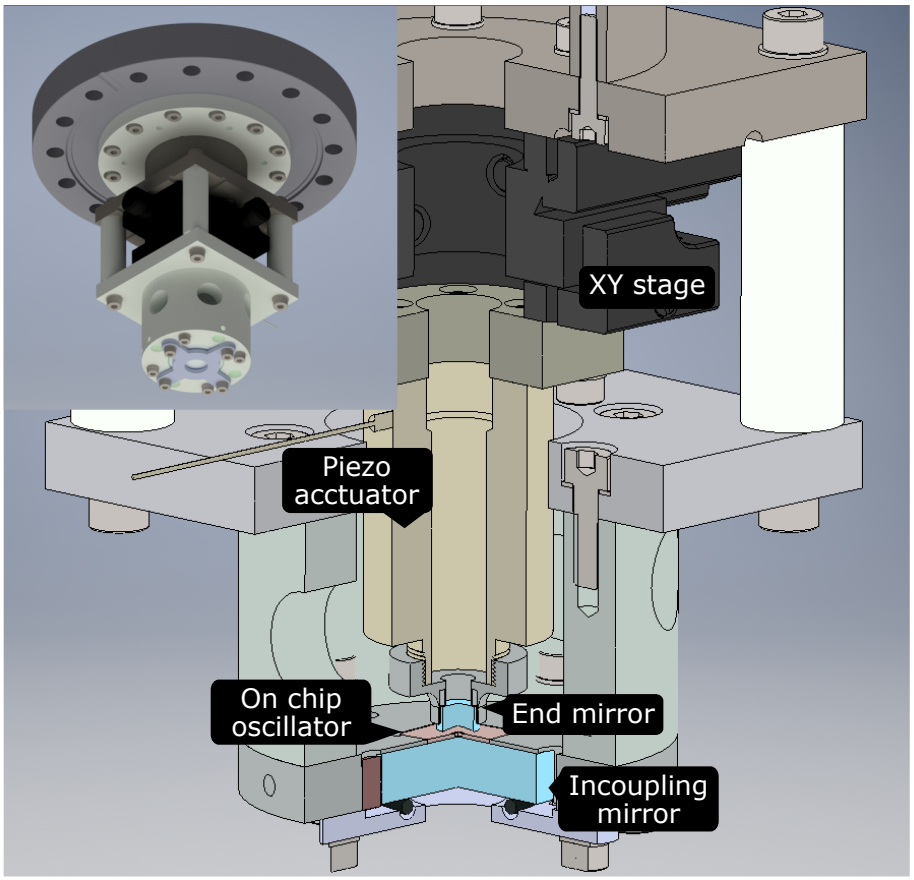

Figure 4.7: Renders of the optomechnical cavity. The main figure shows a three quarter section view, revealing the main cavity components. The commercially available components are an XY stage, a piezo actuator and the mirrors. The remaining support structures are custom made from stainless steel. The figure insert shows a render of the cavity bottom view. The cavity assembly is mounted to bottom of a ConFlat flange, providing that the cavity can be inserted into the vacuum chamber.

maximal stroke is $\Delta z_{max} \sim 16\,\mu$m and the resonance frequency with no weight load attached $\nu_{res} = 30\,$kHz. The plane mirror which is supporting the chip with oscillator is not piezo actuated to prevent coupling of the voltage noise to the oscillator motion.

Degrees of freedom in the transverse directions are provided by a manual XY stage (OWIS MKT 40B-D15-SH-V6) attached to the piezo actuator.

All components have an aperture in the direction of the cavity optical axis, providing optical access to the cavity from both sides.

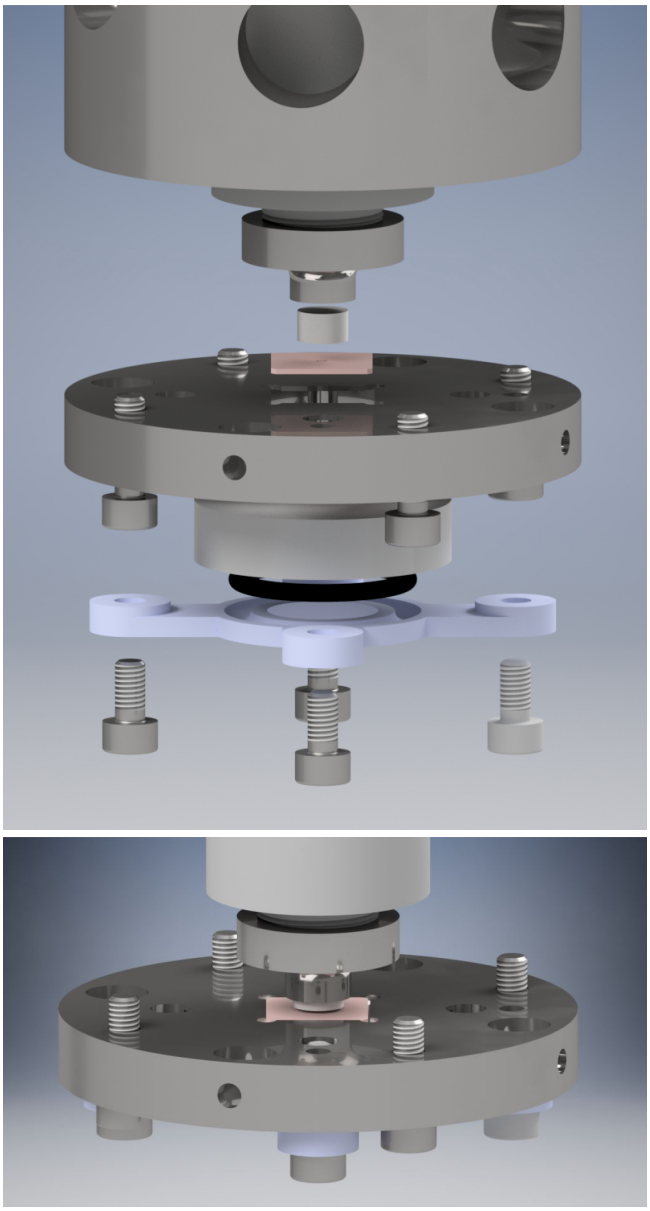

Figure 4.8: Detailed view of the optomechanical cavity. (top) Exploded view of the optical cavity and on-chip oscillator (in light-red color). Assembly goes as follows: firstly, the incoupling plane mirror is clamped to the cavity structural plate. Then, the on-chip oscillator is placed on top of the plane mirror. The square cut-out in the structural plate provides the rough alignment of chip position ($\pm 0.1mm$). Eventually, the structural plate is attached to the steel cylinder which supports the end mirror assembly. Finally, the spherical mirror is attached to the piezo actuator which is mounted to the XY stage. The XY stage is used to align the center of the cavity over the trampoline. (bottom) Final configuration of 1 mm long cavity (The steel cylinder is omitted in this view).

Figure 4.9: View of the optical cavity inside the vacuum chamber.

4.3 Characterization of the optical cavity

The most important cavity parameters are cavity finesse, length and incoupling efficiency.

Cavity linewidth

The cavity spectrum can be directly measured by scanning the frequency of a laser coupled to the cavity and measuring the reflected/transmitted intensity. However, in our experimental setup the laser frequency is fixed, so we scan the cavity length with the piezo actuator instead. By scanning the cavity length and detecting the transmitted light on a photodide, we observe on the oscilloscope the cavity lineshape in a time domain. To obtain the results in absolute frequency, we generate calibration sidebands which will serve as frequency markers. The sidebands are created by a fibre EOM (iXBlue MPZ-LN-10), modulating the phase at frequency $\nu_{mod} = 2\,\mathrm{GHz}$.

On the measurement record shown in figure 4.10, we see three peaks, appearing at the times when the probe beam carrier and the first sideband cross the cavity resonance. When the scan speed is sufficiently slow compared to the cavity ring down time $\sim 1/\kappa$, the peaks in the photodiode voltage (neglecting any DC offset) have a Lorentzian lineshape

$$U(t) = \frac{\tau^2 U_p}{\tau^2 + 4(t_0 - t)^2}, \tag{4.27}$$

where U_p is a peak voltage, τ is a FWHM linewidth and t_0 corresponds to the peak position. We fit the data with a sum of three Lorentzian functions given by Eq. 4.27 and extract t_0 of sidebands and carrier from the fit. Relating the modulation frequency Δ^{ν}_{SB} and time delay in between carrier and sideband detection time Δ^{t}_{SB}, we obtain a frequency change per unit time $\Delta' = \Delta^{\nu}_{SB}/\Delta^{t}_{SB} \approx 2\,[\mathrm{GHz}]/30.12 \cdot 10^{-5}\,[\mathrm{s}] \approx 6.64\,\mathrm{THz} \cdot \mathrm{s}^{-1}$. Then we rescale the fitted peak linewidth $\tau \approx 68.1\,\mu s$ to frequency units as

$$\delta\nu = \kappa/2\pi = \Delta'\tau \approx 451.8\,\mathrm{MHz}. \tag{4.28}$$

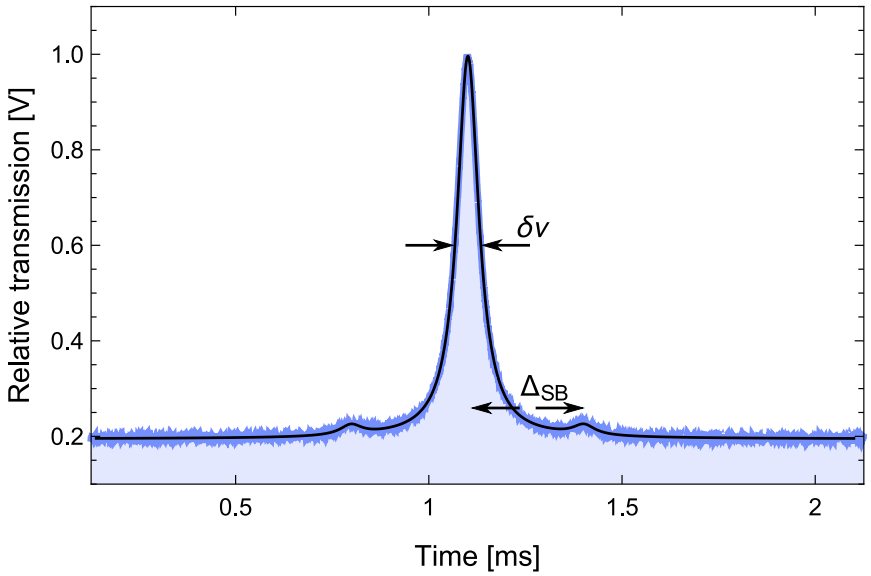

Figure 4.10: Measurement of the TEM_{00} mode linewidth. Data (blue trace) are fitted with a triple Lorentzian function given by Eq. 4.10 (black line). Phase modulation sidebands are created as frequency markers, allowing to rescale lineshape in time units to frequency units and to extract the mode linewidth $\delta\nu$.

Cavity length estimation

The length of the optical resonator is designed to be 1 mm. The effective cavity length is in fact slightly longer than the physical length of a resonator due to the penetration of the intracavity electromagnetic field into the dielectric layers of the mirror coating. The resulting cavity length is also affected by the tolerances in the fabrication process and cavity assembly. Therefore, the real cavity length needs to be estimated by measurement.

The cavity length can be measured in a similar fashion as the cavity linewidth. A straightforward approach is to scan the cavity length (laser frequency) across several (at least two) longitudinal resonances and to use Eq.4.8 yielding $L = c/2FSR$. In our case the range of the piezo actuated mirror covers several FSRs. However, in general the piezo actuators tend to respond in non-linear fashion to the applied voltage over an extended scanning distance. As we do not know the exact response of the actuator to applied voltage, we can at least minimize the measurement error by minimizing the scanning distance.

In order to calculate the cavity length L, we use the frequency non-degeneracy of $TEM_{m,n}$ modes. Eq. 4.24 yields the resonant frequency differ-

ence between the TEM_{00} and TEM_{10} modes in a hemispherical resonator is

$$\Delta\nu = |\nu_{1,1,0} - \nu_{1,0,0}| = \frac{1}{\pi}\frac{c}{2L}\arccos\left(\sqrt{1-\frac{L}{R_c}}\right) \tag{4.29}$$

The first higher order mode is introduced by slightly misaligning the cavity probe beam. To transform the time domain measurements to absolute frequency, we use the same approach as in the linewidth measurement described above. The frequency markers are generated using an EOM with modulation frequency $\nu_{mod} = 3\,\mathrm{GHz}$. The measurement data are in figure 4.11. From a data fit, we obtain the time delay of TEM_{00} and TEM_{10} modes. The sideband marker is used to convert the time delay to the frequency $\Delta\nu$. By plugging $\Delta\nu$ and $R_C = -10\,\mathrm{mm}$ to equation 4.29 and solving the equation numerically for form L, we obtain the estimated cavity length $L = 1.02\,\mathrm{mm}$.

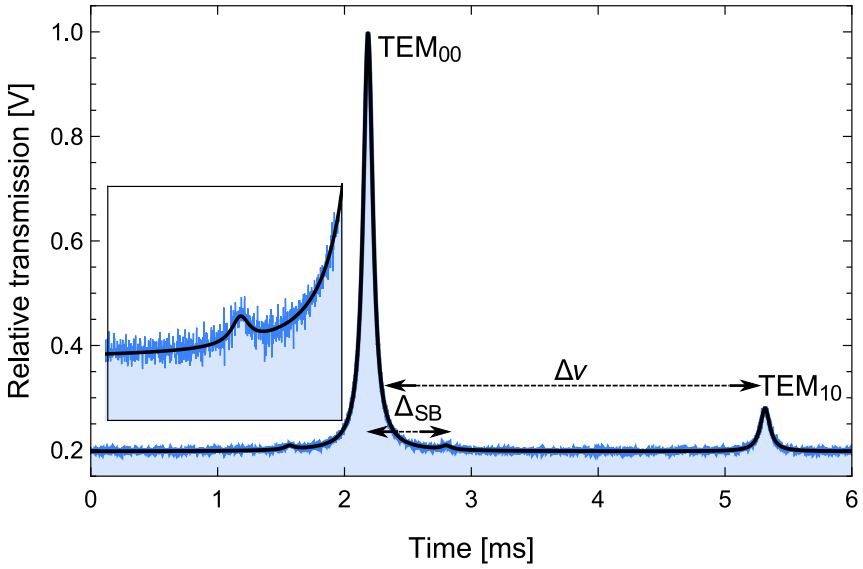

Figure 4.11: Measurement of the cavity length. Transmission of the cavity recorded while sweeping the cavity length (blue trace) is fitted with a sum of four Lorentzian functions defined by Eq. 4.27 (black line). The difference of a TEM_{00} and TEM_{10} modes resonance frequency $\Delta\nu$ reflects the cavity length by Eq. 4.29. The plot inset shows a detail of the modulation sideband next to the TEM_{00} mode, used to calibrate time domain measurement to the frequency units.

Cavity finesse and FSR

Once we know know the exact cavity length, we can use Eq.4.8 to calculate the cavity free spectral range

$$FSR = \frac{c}{2L} \approx 147\,\text{GHz}. \tag{4.30}$$

Finally, combining the previous result with the cavity linewidth measurement, we can estimate the cavity finesse. Using Eq.4.14 the cavity finesse yields

$$\mathcal{F} = \frac{FSR}{\delta\nu} = 326.2. \tag{4.31}$$

4.3.1 Cavity with the mechanical oscillator

In here, we investigate the optical properties of the cavity when the on-chip oscillator is placed inside the cavity. In particular, we are interested in how the total cavity loss rate changes due to the trampoline. The cavity overall loss rate κ is extracted from a linewidth measurement. We measure the linewidth in the same way as in the case of an empty cavity. From the measurement shown in figure 4.12, we extracted

$$\delta\nu = \kappa/2\pi \approx 492.3\,\text{MHz}, \tag{4.32}$$

$$\mathcal{F} = \frac{FSR}{\delta\nu} = 298.8. \tag{4.33}$$

Comparing the results in Eq. 4.28 and Eq. 4.32 we see that the presence of the on-chip trampoline inside the cavity results in the overall loss rate increase by $\approx$ 9%. Those losses may be attributed to the trampoline absorption, diffraction on the trampoline structure, loss due to cavity contamination or due to the modified transmission of the newly formed mirror-trampoline etalon.

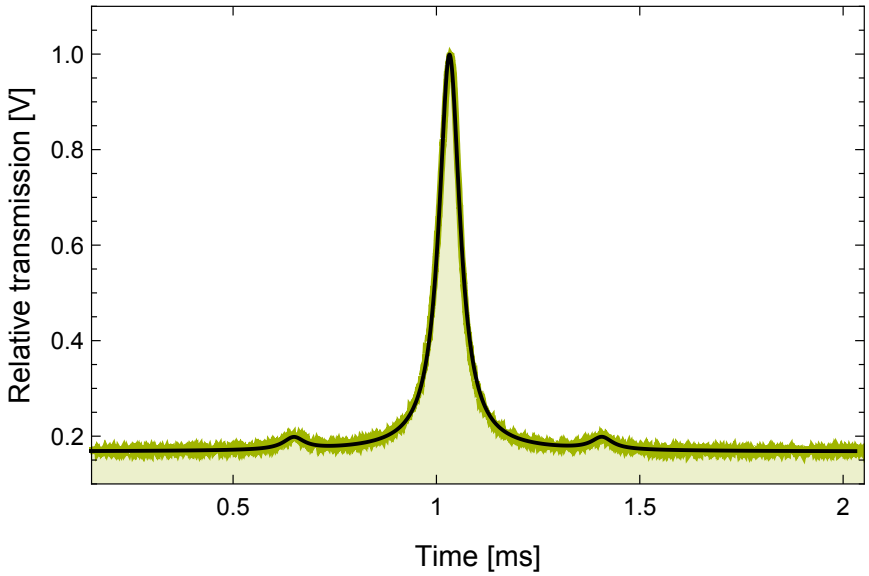

Figure 4.12: Measurement of the TEM_{00} mode linewidth with the trampoline oscillator inside the cavity. Data (Green trace) are fitted with a sum of three Lorentzian function given by Eq. 4.10 (black line). Phase modulation sidebands separated by $\nu_{mod} = 3\,\mathrm{GHz}$ from the carrier (main peak) serve as frequency markers, allowing to rescale the lineshape in time units to frequency units.

Because the simple cavity transmission measurement does not provide information of the cavity losses distribution, but rather quantifies the overall losses rate (together with the FSR measurement), we need to take another measurement to distinguish the intrinsic losses due to the trampoline from the modified mirror transmission.

We denote the transmission of the incoupling and end mirrors T_1 and T_2 respectively and the remaining losses δ. The overall losses are related with the cavity finesse as follows

$$\mathcal{F} = 2\pi\frac{FSR}{\kappa} = \frac{2\pi}{T1 + T2 + \delta}, \tag{4.34}$$

where the finesse was estimated by measurement as $\mathcal{F} = 298.8$ and the nominal values of the mirrors transmission are $T_1 = 19\,000\,\mathrm{ppm}$, and $T_2 = 10\,\mathrm{ppm}$. From Eq. 4.34 we can find that

$$T_1 + \delta = 20\,693\,\mathrm{ppm}. \tag{4.35}$$

We are considering, that by placing the trampoline inside the cavity, transmission of the incoupling mirror T_1 and losses δ are modified, so we need

another relation including T_1 and δ to be able to solve the problem. This relation can be provided by comparing the power transmitted by the cavity with the reflected power in respect to the incident power. Figure 4.13 shows the TEM_{00} lineshape measured in transmission and reflection. It should be noted, that only the fraction of input power ϵP_{in} is coupled to the TEM_{00} mode, where ϵ denotes the modematching factor while $(1-\epsilon)P_{in}$ is wasted. In the further analysis, we use the elegant solution proposed by Kimble [42] witch rules out the mode matching factor. Following the reference we arrive at the expression

$$\frac{P_r - P_{in}}{P_t} = \left(\frac{(\delta + T_2 - T_1)^2}{(\delta + T_2 + T_1)^2} - 1 \right) \frac{(\delta + T_1 + T_2)^2}{4T_1T_2}, \tag{4.36}$$

where P_{in} is the incident power and P_r, P_t are the powers reflected and transmitted on cavity resonance. The optical power is proportional to the photodiode output voltage and since the same photodiode was used to measure transmitted and reflected field we can make a substitution $P \to V_{det}$ in the Eq.4.36. The measured values are $V_t = 3.5\,\mu\mathrm{W}$, $V_{in} = 1.59\,\mathrm{mW}$ and $V_r = 1.46\,\mathrm{mW}$, where the values obtained from the cavity reflection were multiplied by a factor of $1/0.82$ to compensated for losses on mainly originating from a circulator (overall detection efficiency in reflection is $\eta = 0.82$).

Then, we use coupled equations 4.35 and 4.36 to find a solution for T_1 and δ

$$T_1 + \delta = 20\,693\,\mathrm{ppm}, \tag{4.37}$$

$$\frac{V_r - V_{in}}{V_t} = \left(\frac{(\delta + T_2 - T_1)^2}{(\delta + T_2 + T_1)^2} - 1 \right) \frac{(\delta + T_1 + T_2)^2}{4T_1T_2}, \tag{4.38}$$

yielding $T_1 = 20\,285\,\mathrm{ppm}$ and $\delta = 353\,\mathrm{ppm}$. We use this result to estimate the cavity incoupling efficiency η_c. From Eq. 4.34 we see

$$\kappa = \underbrace{FSRT_1}_{\kappa_{ex}} + \underbrace{FSR(T_2 + \delta)}_{\kappa_0}, \tag{4.39}$$

which yields the cavity coupling efficiency

$$\eta_c = \kappa_{ex}/\kappa \approx 96.5\%. \tag{4.40}$$

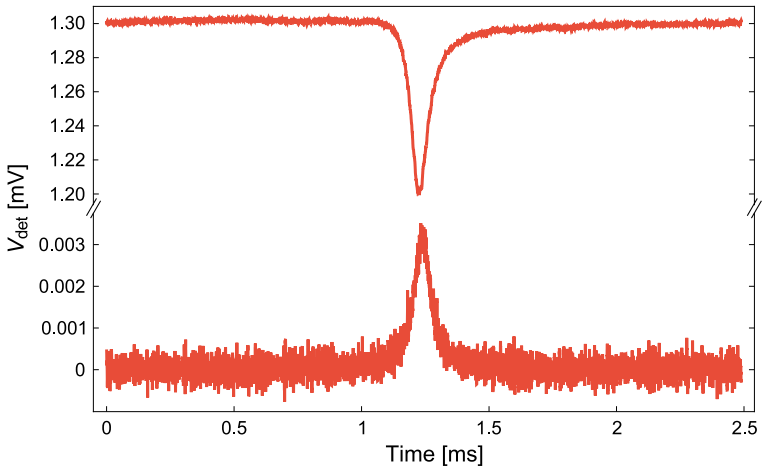

Figure 4.13: Measurement of the TEM_{00} mode in transmission and reflection. Data were obtained in two runs by slowly scanning the cavity length across the resonance. In the first run, the photodiode was placed after the optical cavity, thus measuring its transmission. In the second run, we used the same detector to measure the cavity reflection. The detector was placed after the circulator, separating the probe beam from the beam reflected from a cavity. The circulator works with efficiency $\eta = 0.82$, which needs to be taken into account while evaluating the cavity reflection data.

4.4 Vacuum setup

The optomechanical cavity is placed inside a vacuum chamber, which is essential for removing viscous damping of the trampoline oscillator. The vacuum setup components and their layout is captured in figure 4.14. All vacuum components are fitted together with ISO-CF (conflat) flanges. The CF flanges use a copper gasket and a knife-edge flange to achieve ultra-high vacuum seals down to 10^{-13} mbar. While working with the prototype cavity, we installed a quick-access door to the vacuum chamber, greatly reducing the time needed to reach inside the chamber. The door is sealed with a fluorocarbon (Viton) o-ring providing a seal down to 10^{-9} mbar .

Prior to the experiment, the vacuum chamber is pumped down with a turbo pump backed with a dry diaphragm pump. The ultimate vacuum limit of our turbo pump is $5 \cdot 10^{-8}$ mbar. Running the turbo pump causes acoustic noise and vibrations which are translated to the cavity and optical table through the vacuum hose. While we have not noticed any additional noise in the measurements due to the acoustic noise ($< 56\,\mathrm{dB}$ spec. value) and the mechanical vibrations are greatly reduced by an in-line vibration damper placed in a pumping line, the turbo pump is switched off during all measurements to prevent remaining vibrations to couple to the system. The turbo pump is switched off after reaching a pressure, when the viscous damping of the trampoline oscillator has no significant effect on its quality factor ($P < 10^{-7}\,\mathrm{mbar}$). Prior to switching off the turbo pump, the ion and NEG (non evaporable getter) pumps (ultimate pressure $< 10^{-11}$ mbar) are engaged. Those pumps with no moving parts then maintain the vacuum during the experiment. The turbo pump line is sealed off with an all-metal valve mounted to the vacuum chamber before the pump is switched off.

There are several viewports fitted to the vacuum chamber. The viewports providing optical access to the cavity are located at the top and the bottom flange. The cavity is probed from the bottom, so the whole vacuum chamber is lifted above the optical table to accommodate mode-matching optics as shown in figure 4.15. The top viewport is used for imaging purposes and for cavity transmission measurements.

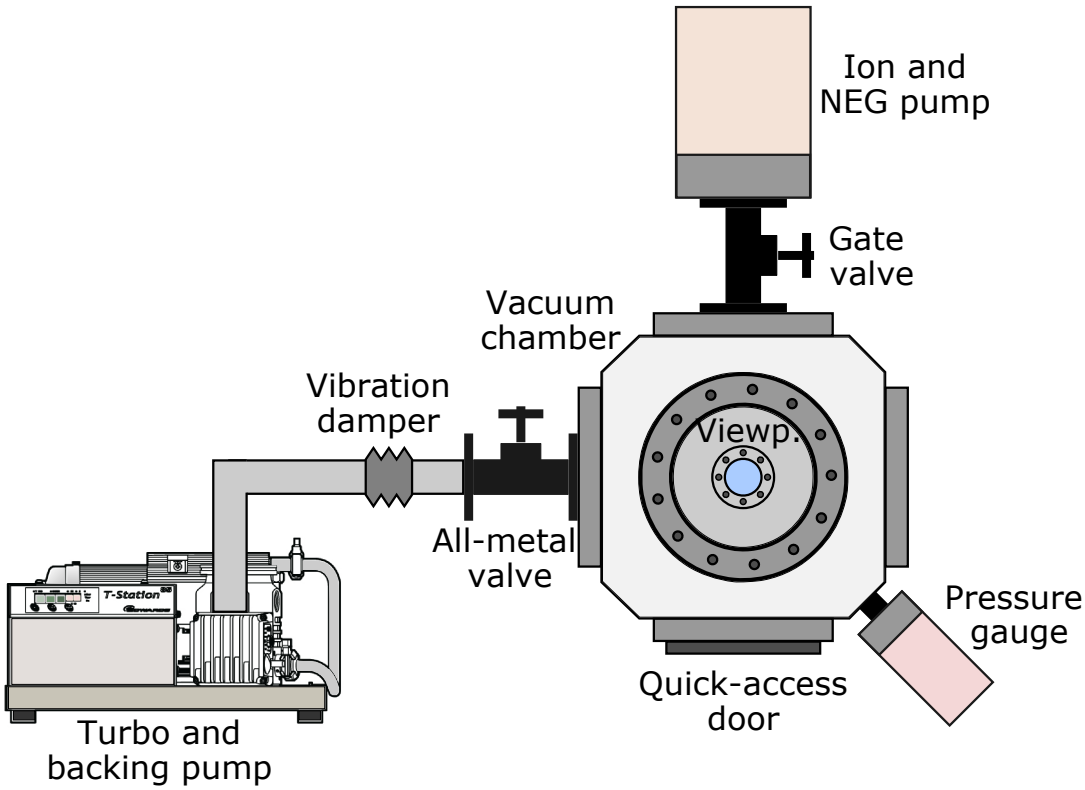

Figure 4.14: Schematic of the vacuum system components. The vacuum chamber (Kimball P. MCF600-SphCube-F6C8) is primarily pumped with a turbo pump station (Edwards T-station 85). When the desired pressure is reached, the turbo pump is switched off and sealed off with an all-metal valve (Leybold) and the chamber is pumped by the ion and NEG pumps (Gamma Vacuum 5S), which are sealed off with a gate valve (LewVac GF-40CF) while not operating. The pressure is monitored with a pirani/cold cathode gauge (Pfeiffer PKR 361). The optical cavity is hanged from the top flange. To easy access the chamber inside, a quick-access door is mounted on the chamber side (Pfeiffer vac.). Optical access is provided via viewports (Thorlabs VPCH42-C) mounted on the top and bottom flanges.

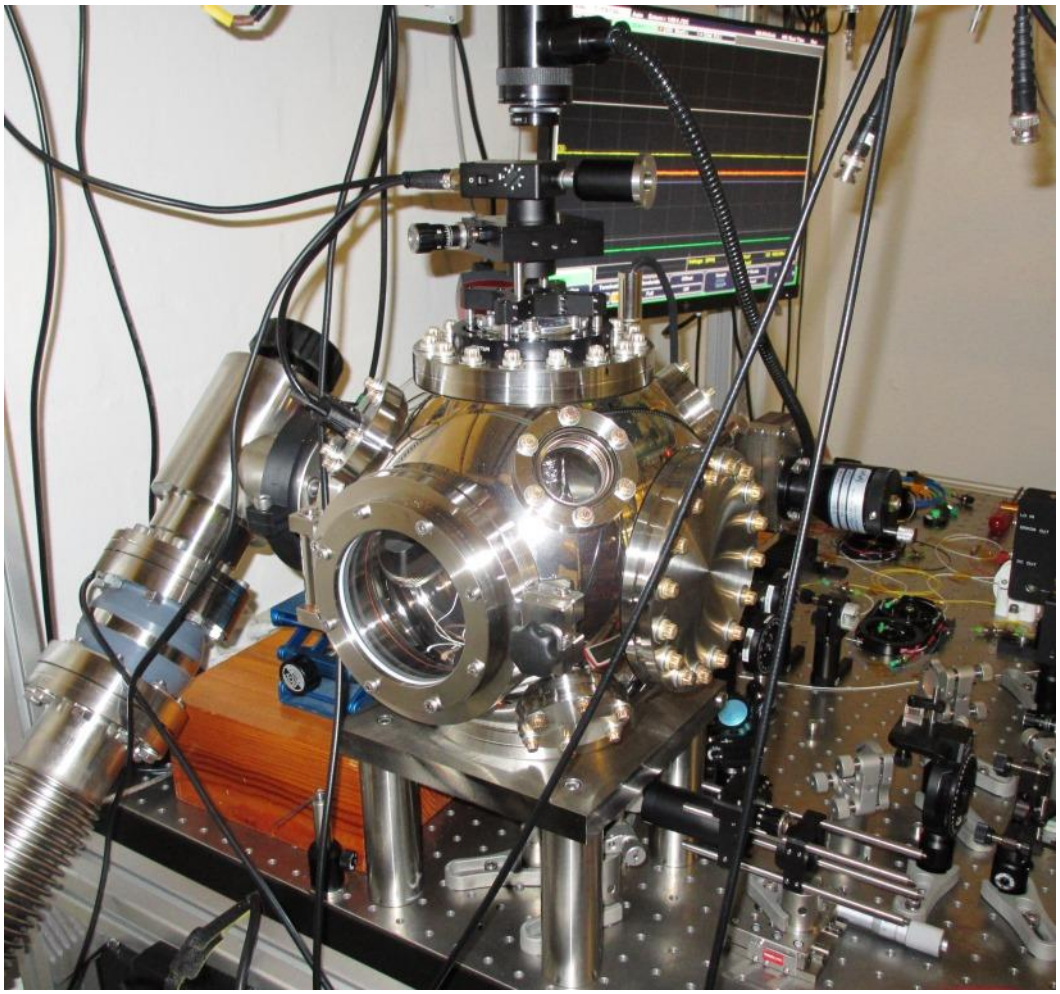

Figure 4.15: Picture of the vacuum chamber on the optical table. On the left side we see the angle valve connected through vibration damper to the turbo pump (out of sight). On the front side of the chamber a quick-access door with viewport is mounted. The whole chamber is lifted, providing optical access via the bottom flange with optical viewport. The optical cavity is hanged from a top flange, where another viewport is fitted. The top viewport is used for imaging purposes or to measure cavity transmission as captured on the picture. On the back side of the chamber (out of view), ion and NEG pumps are fitted through a gate valve (visible at center-right side of the picture). The pressure is monitored with a pirani/cold cathode pressure gauge (out of view).

4.5 Calibration of the EOM

The electro-optical modulator (Pockels cell) plays twofold a role in our experiments. Firstly, the laser is phase modulated for the cavity PDH locking scheme. Secondly, we use the fibre electro-optical modulator to generate a calibration tone for the optomechanical coupling rate estimation. To have control over both processes, we need to know how much phase modulation we get for a given modulation signal amplitude sent to the modulator.

The electro optical modulators utilize the Pockels effect - birefringece induced by an electric field. The index of refraction $n(E)$ is then a function of the applied electric field E and can be expressed as

$$n(E) = n - \frac{1}{2} r n^3 E, \tag{4.41}$$

where r is the Pockels coefficient. In terms of voltage applied to the modulator, we can express the electrically induced phase change of a light field travelling through the Pockels cell as

$$\Delta\phi \approx -\pi \frac{V_{in}}{V_\pi}. \tag{4.42}$$

The parameter V_π is the half-wave voltage - i.e. applied voltage needed to induce phase change by π. The amount of modulation is indicated by a modulation depth β and is equal to the peak phase deviation

$$\beta = \Delta\phi_{max}. \tag{4.43}$$

One way of measuring weak phase modulation is through the interference. We put the EOM to one arm of the Mach-Zehnder interferometer (MZI) to convert phase modulation to amplitude modulation. The MZI is formed by two balanced fiber beam-splitters as outlined in figure 4.16. The other arm of the interferometer contains a fiber-stretcher which allows to change the relative phase between both arms by several π. The output power of the MZI, which is detected on photodiode at one of the outputs, can be expressed as [43]

$$P_{out}(V_{in}) = \alpha \frac{P_{in}}{2} \left[1 + \cos\left(\frac{V_{in}}{V_\pi} \right) \right], \tag{4.44}$$

where α is the insertion loss, P_{in} is the input power, V_{in} is input voltage. The input voltage has two components

$$V_{in}(t) = V_{bias} + V_{mod}(t), \tag{4.45}$$

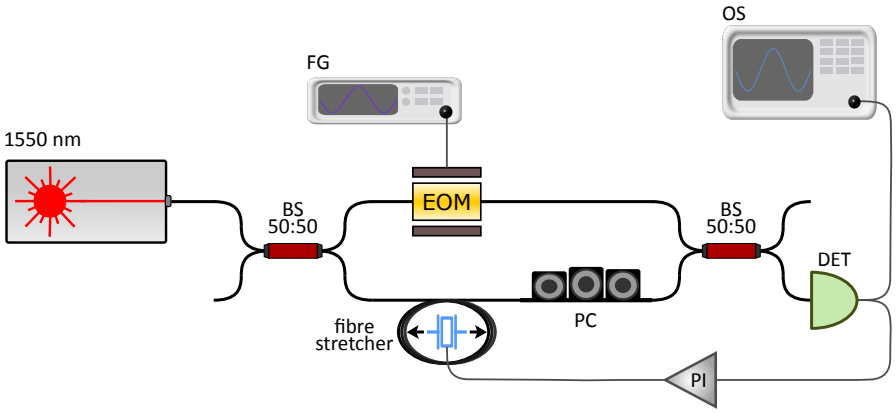

Figure 4.16: Layout of the EOM calibration experiment. A fiber coupled laser is split at a balanced beam-splitter (BS). The phase modulation induced by an EOM is transduced to an amplitude modulation and measured with a photodiode. A feedback loop is used to lock a $\pi/2$ phase difference in the interferometers arms and to stabilize slow phase drifts by minimizing a DC output of a detector. The nearly unity interference visibility is achieved due to the single mode fibers and polarization controller (PC).

where the V_{bias} denotes DC voltage applied to the fiber-stretcher and $V_{mod}(t) = V_{mod}\sin(\Omega_{mod}t)$ is an AC signal driving the EOM with amplitude V_{mod} and angular frequency Ω_{mod}. A linear sweep of bias voltage results in an interference fringe as shown with a red trace in figure 4.17. To achieve undistorted amplitude modulation with the highest extinction ration we set V_{bias} to be equal to $\pm V_\pi/2$. While the bias voltage is maintained by a feedback loop, we modulate the phase with the EOM around that working point on a transfer curve resulting in an amplitude modulation proportional to an input modulation signal.

Figure 4.18 shows the measured interference fringe at the output port of the MZI. Traces of several output signals with different modulation amplitudes V_{mod} are shown in figure 4.19. We extract the maximal phase deviations $\Delta\phi_{max}$ of each trace by evaluating the inverse transfer function of MZI with modulation amplitudes extracted from the fits. Then we use Eq.4.43 to estimate the modulation depth for each modulation amplitude. The frequency of the modulation signal is chosen to be close to the resonant frequency of the fundamental mode of the trampoline oscillators $\Omega_{mod}/2\pi \approx 132\,\mathrm{kHz}$.

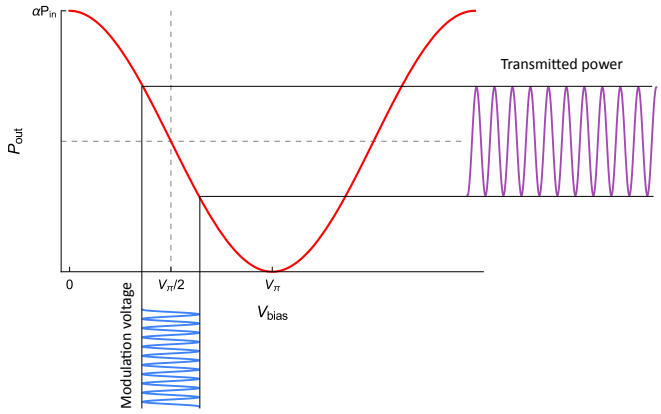

Figure 4.17: Schematic of the phase to amplitude modulation conversion utilizing Mach-Zehnder interferometer.

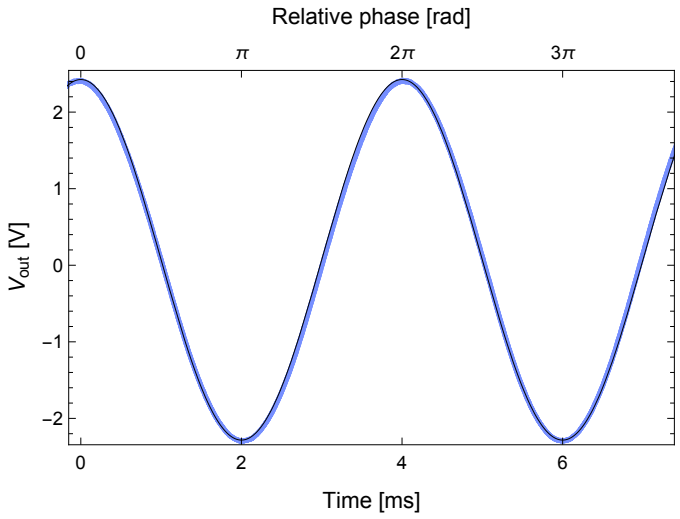

Figure 4.18: Interference fringe at the output of the Mach-Zehnder interferometer. Data (blue dots) are fitted with a cosine function (black line). Data are recorded in a time domain, the relative phase is inferred from a fit.

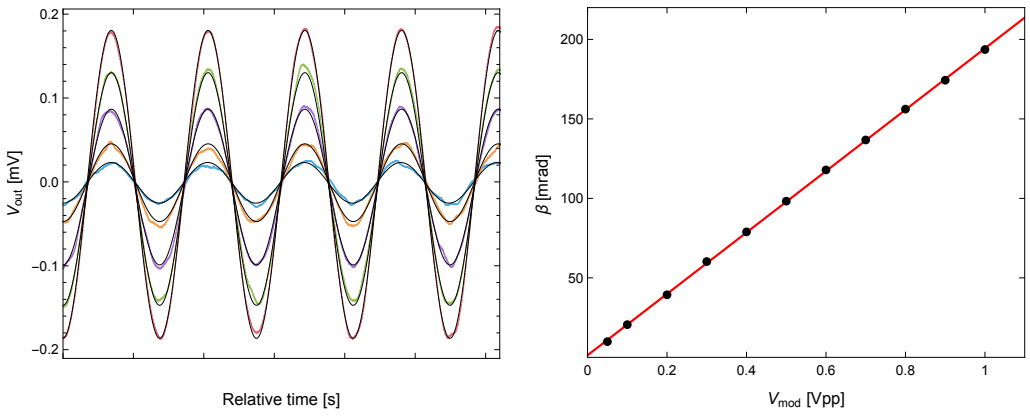

(a) (b)

Figure 4.19: Figure (a): Output of the MZI for different phase modulation amplitudes. The modulation amplitudes V_{mod} are from the top trace: 0.8, 0.6, 0.4, 0.2 and 0.1 V_{pp}. Figure (b): Calculated modulation depth as a function of the EOM driving voltage. The red line is a linear fit to the measured data - black circles.

4.6 Optomechanical vacuum coupling rate

To measure the optomechanical coupling rate g_0 we follow the straightforward procedure proposed by [44]. We saw earlier that the mechanical motion of the oscillator placed inside the cavity is imprinted to the interacting optical field. The oscillator displacement fluctuations S_{xx} are transduced to the cavity resonant frequency fluctuations $S_{\omega\omega}$ via the optomechanical coupling rate

$$S_{\omega\omega}(\Omega) = \frac{g_0^2}{x_{zpf}^2} S_{xx}(\Omega). \tag{4.46}$$

Calculating the variance of the intra-cavity resonance frequency fluctuations, we get the useful relation

$$\sigma_\omega^2 = \int_{-\infty}^{\infty} S_{\omega\omega}(\Omega) \frac{d\Omega}{2\pi} = 2g_0^2 \frac{k_B T}{\hbar\Omega} = 2 \langle n_m \rangle g_0^2, \tag{4.47}$$

which shows that knowing the cavity frequency fluctuations and mechanical occupation number is sufficient to estimate the g_0. We can estimate the number of mechanical quanta $n_m \approx \frac{k_B T}{\hbar\Omega_m}$, valid for a probe beam of small optical power, thus neglecting a back-action heating. Now we need to relate the cavity frequency fluctuations to the experimentally available quantities.

We are performing phase sensitive homodyne measurements, measuring the detector output fluctuations on a spectrum analyser. From a phase frequency relation $\Omega = \dot{\theta}$ we can rewrite Eq. 4.46 in terms of phase fluctuations

$$S_{\theta\theta}(\Omega) = \frac{1}{\Omega^2}\frac{g_0^2}{x_{zpf}}S_{xx}(\Omega). \tag{4.48}$$

The voltage fluctuations S_{VV} measured with the spectrum analyser are related to the actual mechanical displacement through the transduction function $K(\Omega)$

$$S_{VV}(\Omega) = \frac{K(\Omega)}{\Omega^2}\frac{g_0^2}{x_{zpf}^2}S_{xx}(\Omega). \tag{4.49}$$

To calibrate the $K(\Omega)$ we will use a phase modulated laser probe with known modulation depth β. Spectral density of the pure phase modulated monochromatic laser is given as

$$S_{\psi\psi} \propto \beta^2\delta(\Omega - \Omega_{mod}), \tag{4.50}$$

where Ω_{mod} is the modulation frequency. The spectrum analyser convolves the input signal with its bandwidth filter function $F(\Omega)$. The filter function lineshape depends on the spectrum analyser and has a Gaussian lineshape in our case. The filter function is normalised such as $F(0)ENBW = 1$, where $ENBW$ stands for the equivalent noise bandwidth, which is also device dependent and is slightly higher than the SA resolution bandwidth in our case. The detected voltage spectra density from both modulated laser and the mechanics yields:

$$S_{VV}(\Omega) = 2F(\Omega)K(\Omega)\left(S_{\theta\theta}(\Omega) + S_{\psi\psi}(\Omega)\right). \tag{4.51}$$

Providing that the dominating signal at Ω_{mod} frequency is the signal from the laser phase modulation we can approximate the equation above as

$$S_{VV}(\Omega_{mod}) \propto \frac{\beta^2 K(\Omega_{mod})}{2ENBW}, \tag{4.52}$$

where all parameters except $K(\Omega_{mod})$ are known. Finally, we assume that the system transfer function is constant over a small frequency band around the mechanical resonance frequency, so $K(\Omega_m) \approx K$. This assumption is well justified in our deeply sideband unresolved regime and with a broad-band detection. To estimate the g_0 we start by combining Eq.4.46 and Eq.4.49

$$S_{VV}(\Omega)\frac{\Omega_m^2}{K(\Omega)} = S_{\omega\omega}(\Omega). \tag{4.53}$$

Integrating the left side of the equation we get

$$\int_{-\infty}^{\infty} S_{VV}(\Omega)\frac{\Omega^2}{K(\Omega)}\frac{d\Omega}{2\pi} \approx \frac{\Omega_m^2}{K}\int_{-\infty}^{\infty} S_{VV}(\Omega)\frac{d\Omega}{2\pi} = \frac{\Omega_m^2}{K}\sigma_V^2, \tag{4.54}$$

where σ_V^2 is the variance of detected voltage fluctuations. Finally by combining Eq.4.47 and Eq.4.54 we can estimate the g_0 as

$$g_0^2 \propto \frac{\Omega_m^2}{K}\frac{\sigma_V^2}{2\langle n_m\rangle}. \tag{4.55}$$

Calibration data

In figure 4.20 we see the results of the calibration measurement. The experimental setup is presented in the feedback cooling chapter. The green trace was recorded on a spectrum analyser using 420 nW of optical probe power (before coupling to the optical cavity) and 1.2 mW of local oscillator power. Direct output of the SA yields the power spectral density in dBm units as shown on the right scale. The left scale is in displacement units inferred through calibration of the system transduction function K. The central Lorentzian shaped peak is due to the thermal motion of the trampoline. The calibration tone on the left corresponds to the phase modulation with modulation depth $\beta = 0.052$. Using the Eq. 4.55 we estimated $g_0/2\pi = 0.75$ Hz. This value also reflects the spatial overlap between the optical mode inside the cavity and the trampoline mechanical mode.

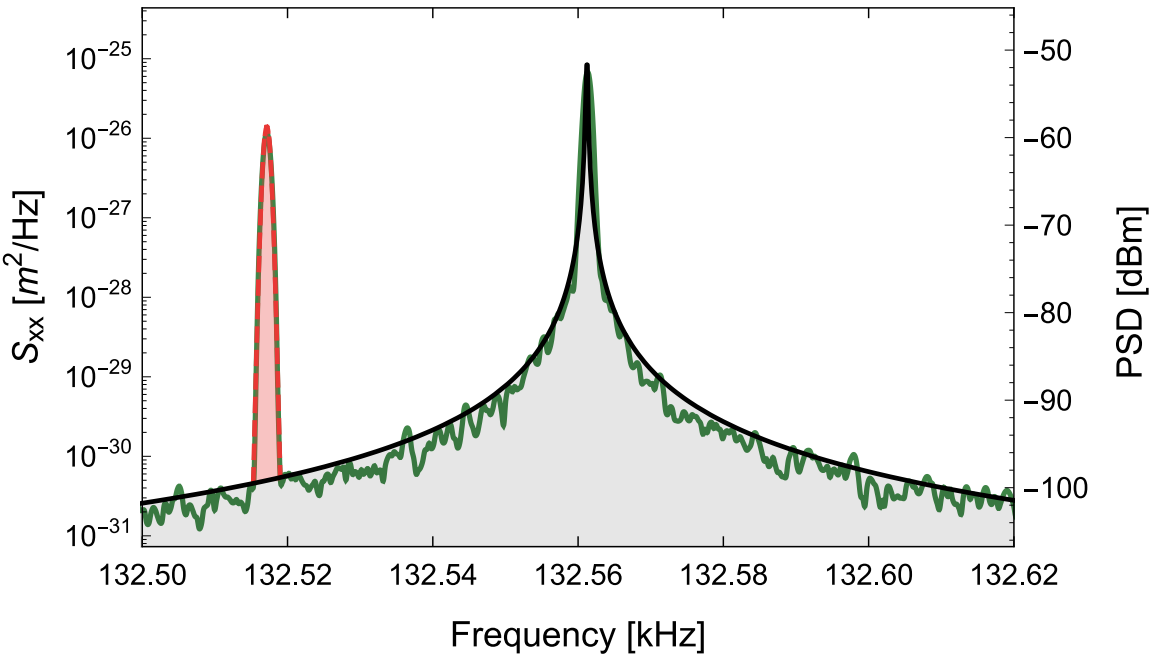

Figure 4.20: Power spectral density of the mechanical fundamental mode (data - green line, fit - black line) and calibration tone (data - green line, fit - red dashed line). The scale on the right shows voltage fluctuations as measured with the spectrum analyser. The scale on the left shows the inferred displacement spectrum of the oscillator. Comparing the area under the mechanical mode to the area under the known phase modulation is used to deduce the vacuum optomechancal coupling rate.

Chapter 5

Feedback Cooling

5.1 Introduction

Thermal noise is limiting factor in many optomechanical system. The ability to cool down a mechanical system is important in application ranging from high sensitivity force measurements [45], large-scaled gravitational wave detectors [46, 47] to observing quantum phenomena in macroscopic systems [48]. A prior requirement to observe quantum behaviour of the oscillator is to cool it down near to the motional ground state [4, 49, 50]. Depending on the system parameters, different approaches would lead to the most effective cooling.

Perhaps the most straightforward is a *passive cryogenic cooling* through a low temperature thermal bath. However, even in the dilution refrigerator reaching $T \sim 10\,\mathrm{mK}$ cooling to the ground state is not possible unless the mechanical frequency is in the GHz range [23]. As the oscillation frequency usually scales with inverse proportionally to the oscillating mass, passive cryogenic cooling is not feasible on its own for reaching ground state of a macroscopic systems.

Radiation pressure cooling (sideband cooling), derived from laser cooling of atoms and ions [51] is based on a resonance enhancement of the upper (anti-Stokes) motional sidband and its filtering from its lower (Stokes) counterpart. This dynamical backaction cooling scheme is most effectively done by a high Q optical cavity with linewidth (κ) narrower than the oscillator mechanical frequency (Ω_m). It has been demonstrated in various optomechanical systems [52–54] including semiconductor nanomemembranes [55]. Cooling to ground state employing sideband cooling was experimentally demonstrated using silicon nanoresonators [12] pre-cooled to $T \sim 10\,\mathrm{K}$ in a helium cryostat.

In a *Feedback cooling* protocol [56], which is the subject of this chapter, the oscillator position is estimated in a real time measurement and the measurement output is converted to the feedback force steering the oscillator towards the ground state. Feedback cooling to the ground state was recently demonstrated with cyogenically pre-cooled SiN membranes with a phononic shielding[13].

5.2 Theoretical framework

The feedback cooling (also known as *cold damping*) protocol relies on a continuous measurement of oscillator position and applying a negative derivative force damping its motion without increasing the thermal noise. The oscillator position is transduced to the phase of the probe optical field which is detected with phase sensitive measurement. The output of a measurement is used to derive a negative feedback and fed back to the oscillator minimizing the displacement. In the most conventional schemes, the feedback force is proportional to the time derivative of a measurement (i.e. oscillator velocity) leading to a viscose damping of a oscillator motion. The feedback actuation implementation varies depending on a physical system being cooled and involves dielectric gradient force [40, 57], piezo-driven cantilevers [58] or coil actuators [59].

In this thesis, we consider cooling of the fundamental vibrational mode of the nano trampoline by radiation pressure force. The optical cavity provides a high sensitivity displacement readout and enhances the optomechanical interaction through a multi-pass interaction with the oscillator.

System dynamics

We start the description of the system by considering a harmonic oscillator, whose instantaneous position is described by $\hat{x}(t)$. The mechanical displacement $\hat{x}(\Omega)$ of the oscillator in frequency domain subjected to the total force $\hat{F}_{tot}$ is given as

$$\underbrace{(\Omega_m^2 - \Omega - i\Omega\Gamma_m)}_{\equiv \chi_m^{-1}} \hat{x}(\Omega) = m_{eff}^{-1} \hat{F}_{tot}(\Omega), \tag{5.1}$$

where χ_m is mechanical susceptibility, Ω_m is angular frequency, Γ_m intrinsic damping and m_{eff} is the effective mass of the mechanical mode. When the mechanical motion is optically probed in absence of feedback, the resonator is driven by a thermal force $\hat{F}_{th}$ and by a back-action force $\hat{F}_{ba}$ due to the probe beam radiation pressure shot noise. The total force then reads

$$\hat{F}_{tot} = \hat{F}_{th} + \hat{F}_{ba}; \tag{5.2}$$

The feedback force is proportional to the outcome of the displacement measurement $\hat{y}(\Omega) = \hat{x}(\Omega) + \hat{x}_{imp}(\Omega)$, where $\hat{x}_{imp}(\Omega)$ is effective displacement noise and is given by

$$\hat{F}_{fb}(\Omega) = m_{eff}\chi_{fb}(\Omega)\hat{y}(\Omega), \tag{5.3}$$

where $\chi_{fb}(\Omega)$ is the feedback controller transfer function, characterizing gain and phase delay of the feedback loop. By tuning feedback parameters we can achieve cooling or heating of the oscillator. Closing the feedback loop results in oscillators dynamics bellow

$$\begin{aligned}\hat{x}(\Omega) &= m_{eff}^{-1}\chi_m(\Omega)\left(\hat{F}_{tot}+\hat{F}_{fb}\right)\\ &= m_{eff}^{-1}\chi_m(\Omega)\left(\hat{F}_{tot}+m_{eff}\chi_{fb}(\Omega)\hat{y}(\Omega)\right)\\ &= m_{eff}^{-1}\chi_m(\Omega)\left(\hat{F}_{tot}+m_{eff}\chi_{fb}(\Omega)(\hat{x}(\Omega)+\hat{x}_{imp}(\Omega))\right)\\ &= m_{eff}^{-1}\chi_{eff}(\Omega)\left(\hat{F}_{tot}+m_{eff}\chi_{fb}(\Omega)\hat{x}_{imp}\right), \end{aligned} \tag{5.4}$$

where we introduced the effective susceptibility of the oscillator under the feedback

$$\chi_{eff}(\Omega) = \frac{\chi_m}{1-\chi_{fb}(\Omega)\chi_m(\Omega)}. \tag{5.5}$$

From Eq. 5.4 we see that the feedback cooling alters the dynamics of the oscillator by modifying its susceptibility. Rewriting the effective susceptibility as

$$\chi_{eff}^{-1}(\Omega) = \left[\left(\Omega^2 - \Re\left[\chi_{fb}(\Omega)\right] - \Omega_m^2\right) - i\Omega\Gamma_m\left(1+\Im\left[\chi_{fb}(\Omega)\right]/\Omega\Gamma_m\right)\right], \tag{5.6}$$

reveals that the real part of feedback susceptibility modifies the resonant frequency as $\Omega_{fb}^2 = \Omega_m^2 - \Re[\chi_{fb}]$ and the imaginary part modifies the dissipative coupling to the environment. We model the feedback control transfer function as

$$\chi_{fb}(\Omega) = G_{fb}\Omega\Gamma_m \exp(i\Omega_m\tau_{fb}), \tag{5.7}$$

where G_{fb} is the dimension-less gain and τ_{fb} is a feedback loop time delay. From Eq. 5.6 we see that setting the delay as $\Omega_m\tau_{fb} = \frac{\pi}{2}$ modulo 2π results in optimal dissipative cooling with modified effective damping rate

$$\Gamma_{eff} = \Gamma_m(1+G_{fb}), \tag{5.8}$$

with $\Gamma_{fb} = \Gamma_m G_{fb}$ being the damping due to the feedback cooling.

Displacement spectrum

The power spectral density of the oscillator's actual position under a feedback loop can be derived from Eq. 5.4. Assuming that the noise sources are uncorrelated, the PSD reads

$$S_{xx} = \langle|\hat{x}(\Omega)|^2\rangle = |\chi_{eff}(\Omega)|^2(m_{eff}^{-2}S_{FF}^{tot}(\Omega) + |\chi_{fb}(\Omega)|^2 S_{xx}^{imp}(\Omega)). \tag{5.9}$$

where S_{FF}^{tot} is the spectral density of the effective thermal force and S_{xx}^{imp} is spectral density of the measurement noise $\hat{x}_{imp}$ being fed back to the oscillator. Using the beforementioned model of feedback controller given by Eq. 5.7 and oscillator effective susceptibility χ_{eff} defined in Eq. 5.5 we can expand the PSD as follows:

$$S_{xx}(\Omega) = \left[\frac{1/m_{eff}^2}{(\Omega_m^2 - \Omega^2)^2 + ((1+G_{fb})\Omega\Omega_m/Q_m)^2}\right] S_{FF}^{tot}(\Omega) + \left[\frac{(\Omega G_{fb}\Gamma_m)^2}{(\Omega_m^2 - \Omega^2)^2 + ((1+G_{fb})\Omega\Omega_m/Q_m)^2}\right] S_{xx}^{imp}(\Omega), \quad (5.10)$$

where $Q_m = \Omega_m/\Gamma_m$ is the quality factor of the mechanical oscillator. In the same way, we express the PSD of the measured displacement $\hat{y} = \hat{x} + \hat{x}_{imp}$

$$S_{yy}(\Omega) = \left[\frac{1/m_{eff}^2}{(\Omega_m^2 - \Omega^2)^2 + ((1+G_{fb})\Omega\Omega_m/Q_m)^2}\right] S_{FF}^{tot}(\Omega) + \left[\frac{(\Omega_m^2 - \Omega^2)^2 + (\Omega\Gamma_m)^2}{(\Omega_m^2 - \Omega^2)^2 + ((1+G_{fb})\Omega\Omega_m/Q_m)^2}\right] S_{xx}^{imp}(\Omega). \quad (5.11)$$

Note that with a zero gain, the $S_{xx}(\Omega)$ has a Lorentzian profile with FWHM corresponding the damping Γ_m. The temperature T of the mechanical mode can be extracted from PSD using equipartition theorem

$$\langle x^2 \rangle = k_B T / m_{eff}\Omega_m^2, \quad (5.12)$$

where the position fluctuations are proportionals to the area under the curve [60]

$$\langle x^2 \rangle = \int_{-\infty}^{\infty} S_{xx}(\Omega)\frac{d\Omega}{2\pi}. \quad (5.13)$$

With a low feedback gain ($G_{fb} \ll 1$), the physical displacement spectrum can be obtained by subtracting of the measurement noise floor from the measured spectrum $S_{xx}(\Omega) = S_{yy}(\Omega) - S_{xx}^{imp}(\Omega)$. This is still valid for larger gains, if an imprecision noise is below the measured displacement power $S_{xx}^{imp} \ll \frac{Q_m}{G_{fb}} m_{eff}\Omega_m^2$ [58].

By increasing the feedback gain, the oscillator motion become correlated with the imprecision noise which eventually leads to the intensity *squashing* in measurement spectrum [61]. The noise *Squashing* manifests itself in measured data as a negative peak below the measurement noise. Considering

that the temperature is proportional to the integral of PSD, this would lead to the negative temperature estimation, which is clearly unphysical. Therefore, it is important to distinguish from an *out-of-loop* spectrum and *in-loop* spectrum given by Eq. 5.10 and Eq. 5.11 respectively, when infering the oscillator temperature.

Experimentally, the *out-of-loop* spectrum can be obtained using two independent probes for temperature estimation a feedback force derivation, e.g. by using two detuned laser beams.

Driving forces

The driving terms in eq. 5.9 can be expressed in terms of the thermal noise equivalent quanta. The ambient bath temperature T with which the oscillator equilibrates adds n_{th} thermal phonons to the mechanical state

$$n_{th} = \frac{1}{2}\coth\left(\frac{\hbar\Omega_m}{2k_BT}\right). \tag{5.14}$$

The remaining driving terms due to the measurement noise n_{imp} and stochastic probe fluctuation n_{ba} are given by [27]

$$n_{imp} = S_{xx}^{imp}(\Omega)/2S_{xx}^{zpm}(\Omega_m), \tag{5.15}$$

$$n_{ba} = S_{FF}^{ba}(\Omega)/\frac{m_{eff}^2}{|\chi_m(\Omega_m)|^2}2S_{xx}^{zpm}, \tag{5.16}$$

where S_{xx}^{zpm} corresponds to the peak position spectral density of the ground state and is given by

$$S_{xx}^{zpm} = \frac{4x_{zpm}^2}{\Gamma_m}. \tag{5.17}$$

Now we can rewrite the driving force in Eq. 5.9 as

$$S_{FF}^{tot} = (n_{th} + n_{ba} + \frac{1}{2})\frac{m_{eff}^2}{|\chi_m(\Omega_m)|^2}2S_{xx}^{zpm}(\Omega_m), \tag{5.18}$$

which will be useful in further discussion of the thermal occupancy limit.

In case of shot-noise limited amplitude quadrature, the *back-action noise* originating from the probe beam intensity fluctuations is given by

$$n_{ba} = C_0 n_{cav}, \tag{5.19}$$

where n_{cav} corresponds to the intra-cavity photon number and C_0 is the single-photon cooperativity,

$$C_0 \equiv \frac{4g_0}{\kappa\Gamma_m}. \tag{5.20}$$

The *imprecision noise* transduced from the probe phase noise into a homodyne detector with quantum efficiency (quantum efficiency of photodiodes) η_d is given by [27]

$$n_{imp} = (16\eta_t C_0 n_{cav})^{-1}, \tag{5.21}$$

where $\eta_t = \eta_o\eta_c\eta_d$ is the total optical detection efficiency, η_o corresponds to efficiency of all optical components and η_c is the cavity outcoupling efficiency.

The *intra-cavity photon number* in case of on resonance excitation valid in our experiment and with optical power P_{in} entering the cavity of linewidth κ is given by

$$n_{cav} = \frac{4\eta_c}{\kappa}\frac{P_{in}}{\hbar\omega_c}. \tag{5.22}$$

Eqs. 5.21 and 5.19 imply that the oscillator position measurement is bound by the imprecision-back action product

$$4\sqrt{n_{imp}n_{ba}} \geq 1. \tag{5.23}$$

Thermal occupancy limit

Main goal of a feedback cooling is to minimize mean phonon occupancy of the harmonic oscillator $\langle n_m \rangle$ given as [31]

$$\langle n_m \rangle = \int \frac{S_{xx}(\Omega)}{x_{zp}^2}\frac{\mathrm{d}\Omega}{2\pi} - \frac{1}{2}. \tag{5.24}$$

When $\langle n_m \rangle < 1$ is reached, we consider that the oscillator (more precisely the vibrational mode being cooled) is in a motional ground state. Requirements to achieve a ground state cooling are discussed more in details in [32].

Calculating the Eq.5.24 using expression for a driving force given by 5.15 yields the phonon occupancy of the cooled oscillator

$$\langle n_m \rangle = \frac{(n_{th} + n_{ba} + 1/2) + n_{imp}G_{fb}^2}{1 + G_{fb}} - \frac{1}{2}. \tag{5.25}$$

The optimal gain which minimizes the thermal occupancy in Eq.5.25 is

$$G_{fb}^{opt} = \sqrt{\frac{n_{th} + n_{ba}}{n_{imp}}}, \tag{5.26}$$

which yields the minimum thermal occupancy

$$\langle n \rangle_{min} \approx 2\sqrt{n_{imp}(n_{th} + n_{ba})} - \frac{1}{2}. \tag{5.27}$$

From the equation above, we can express the condition for a ground state cooling as

$$n_{imp} < \frac{9}{16}\frac{1}{n_{th} + n_{ba}}. \tag{5.28}$$

In the case of quantum-limited sensing (i.e. saturating the inequality on Eq.5.23) we arrive to the ultimate requirements for reaching the quantum ground state

$$n_{imp} < \frac{1}{16 n_{th}}\left(9 - \frac{1}{\eta_t}\right), \tag{5.29}$$

$$\eta_t > \frac{1}{9}. \tag{5.30}$$

The results above yield the threshold value for the total detection efficiency η_t and measurement noise.

Effective temperature

The effective temperature of the cooled oscillator T_{fb} can be related to the temperature of an oscillator being in thermal equilibrium with its environment at temperature T_0. This corresponds to the feedback loop switched off (G_{fb} =0). Assuming that the oscillator under feedback retain Lorentzian profile with effective resonant frequency Ω_{fb} and effective damping Γ_{eff} and using the equipartition theorem as previously, we can express the effective temperature as [40]

$$\frac{T_{fb}}{T_0} = \frac{\int_{-\infty}^{\infty} \langle|\hat{x}(\Omega)|^2\rangle \, \mathrm{d}\Omega}{\int_{-\infty}^{\infty} \langle|\hat{x}(\Omega)|^2\rangle_{G_{FB}=0} \, \mathrm{d}\Omega} = \frac{\Gamma_{eff} \langle|\hat{x}(\Omega_{fb})|^2\rangle}{\Gamma_m \langle|\hat{x}(\Omega_m)|^2\rangle_{G_{FB}=0}} \tag{5.31}$$

Using the experimentally accessible parameters we can express the effective temperature as

$$\frac{T_{fb}}{T_0} = \left(1 + \frac{G_{fb}^2}{SNR}\right)\frac{1}{1 + G_{fb}}, \tag{5.32}$$

where the signal-to-noise-ratio (SNR) can be directly extracted from the measured PSD as the ratio of on-resonance to off-resonance noise levels

$$SNR = \frac{\langle|\hat{x}(\Omega_m)|^2\rangle_{G_{fb}=0}}{\langle|\hat{x}_{noise}(\Omega)|^2\rangle}. \tag{5.33}$$

From Eq. 5.32 we can find an optimal gain $G_{fb}^{opt} = \sqrt{1 + SNR}$ which minimize the effective temperature achievable considering constant SNR over measurement

$$T_{fb}^{min} = 2T_0\frac{\sqrt{1 + SNR} - 1}{SNR}. \tag{5.34}$$

5.3 Feedback cooling experimental setup

Figure 5.1 shows the schematic of the feedback cooling experiment. The experiment is sourced by continuous-wave fiber coupled laser (NKT E15) outputting linearly polarized light at central wavelength $\lambda = 1550$ nm. The laser maximum output power is around 40 mW. Optical power is controlled at several places in the setup using combination of half-wave plates and polarization beam splitting cubes. The laser output is split into two arms on a 90:10 fiber coupler. The larger portion of the light serves as a bright *local oscillator* (LO) for homodyne detection, the remaining 10% is used as a *probe/cooling beam* (also referred as a *signal beam*).

Probe beam is sent through a fiber electro-optical modulator (EOM) and fiber amplitude modulator (AM) and out-coupled to the free space. The beam is then routed through the circulator to the single-sided optical cavity with linewidth $\kappa/2\pi = 492.3\,\mathrm{MHz}$. The cavity contains a trampoline resonator with fundamental mode resonance frequency $\Omega_m/2\pi = 132.6\,\mathrm{kHz}$. Signal reflected from the cavity is separated from incident beam on a circulator and routed to the homodyne detector. Circulator consist of a two polarisers sandwiching a Faraday rotator.

Part of the reflected signal is tapped off to be detected on a avalanche photodiode (Thorlabs APD130C) and down-mixed with an electronic local oscillator to generate an error signal for cavity locking. The phase modulation needed for a Pound-Drever-Hall (PDH) locking scheme [62] employed in our setup is provided by fiber EOM. The signal for a phase modulation and signal demodulation is generated with a dual channel function generator. Both channels are frequency locked at $\omega_{PDH}/2\pi = 28$ MHz and the relative phase in between both channels is set to optimize the error signal. The error signal is sent to a proportional-integral controller and after amplifying to the piezo actuator inside the cavity.

For a calibration purposes described in a previous section we can send a second calibration tone to the EOM along with the locking tone. In that case, the both signals are combined at power combiner.

Feedback loop is used to stabilize the relative phase difference of $\pi/2$ in between LO and signal beam at the homodyne detector. The error signal obtained from a homodyne detector DC output is sent through the PI controller to the piezo actuated fiber stretcher located in LO arm.

Single mode fibers are utilized in all fiber components in the setup. With the exception of the fiber stretcher, all fibers are also polarization maintaining.

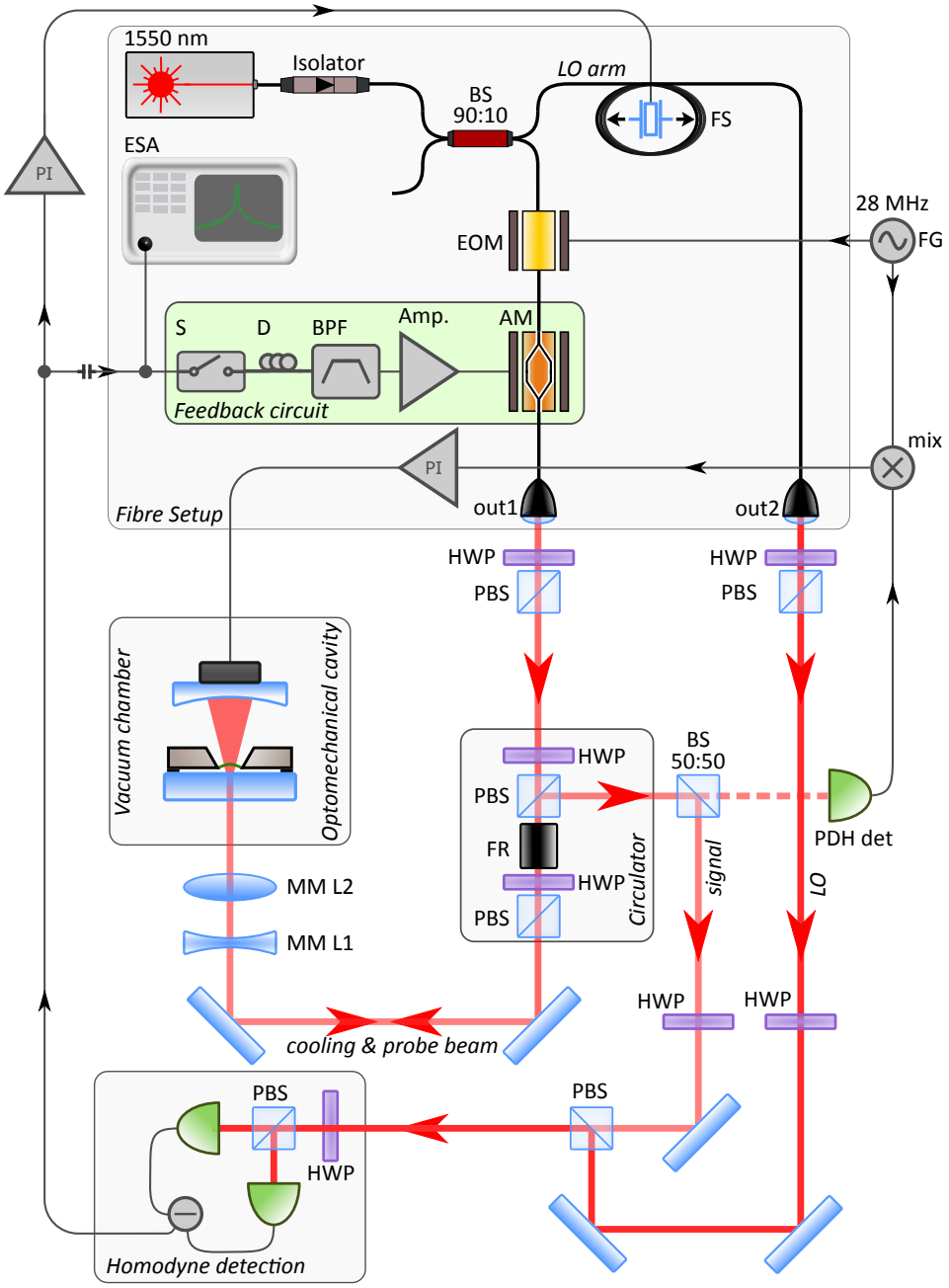

Figure 5.1: Schematics of the feed-back cooling experiment layout. Acronyms: beam splitter (BS), fiber stretcher (FS), electro-optical modulator (EOM), amplitude modulator (AM), outcoupler (out), half-wave plate (HWP), polarisation beam splitter (PBS), lens (L), proportional integral controller (PI), function generator (FG), switch (S), delay line (D), amplifier (Amp), band-pass filter (BPF), electronic spectrum analyser (ESA).

The fluctuations of the trampoline are transduced to the phase of the probe beam and detected on a homodyne detector. The AC output of the HD is used to record oscillator displacement spectrum and as an input signal to feedback cooling electronic circuit. Band-passed and amplified feedback signal is sent to the fiber amplitude modulator. By adjusting the signal phase delay, we can achieve friction cooling of the mechanical mode by cooling beam radiation pressure.

List of main components

Table 5.1 provides an overview of the main components used in the feedback cooling experiment. Optical loss of the components contributing to the total detection efficiency are marked with *. Note that due to the single-sided cavity design, before detection, light goes through some components - e.g. mode-matching lenses, vacuum chamber viewport or Faraday rotator twice.

Component	Product	Optical loss
fiber coupler	Thorlabs PN1550R2A2	$< 7\%$
EOM	iXBlue MPZ-LN-10	44%
AM	iXBlue MXAN-LN-10	55%
Outcoupler	Thorlabs TC12FC-1550	$< 0.5\%$
Mirror HR	Laser Optics HR	$< 0.01\%^*$
Mirror	Thorlabs BB1-E04	$< 1\%$
Faraday rotator	Thorlabs IO-5-1550-HP	$8\%^*$
MM lens1	Thorlabs (c coated)	$0.5\%^*$
MM lens2	Thorlabs (c coated)	$0.5\%^*$
Halfwave plate	Thorlabs WPH05M-1550	$< 0.5\%^*$
PBS	Thorlabs PBS25-1550	$< 5\%^*$ (trans.), $< 0.5\%^*$ (refl.)
Chamber viewport	Thorlabs VPCH42-C	$< 1\%^*$

Table 5.1: Main optical components used in a feedback cooling experiment outlined in figure 5.1. Components contributing to the detection loss are marked with *.

Feedback cooling circuit

Block diagram of feedback cooling circuit is illustrated in figure 5.2. The feedback loop is sourced with an AC output of the homodyne detector. Signal is firstly low-passed filtered and then split on a BNC T-piece into data acquisition and feedback signals. A low-pass filter with cut-off frequency at 1.9 MHz removes high frequency optical phase noise originating predominantly

from a PDH phase modulation at 28 MHz. Then, the signal is band-passed filtered, delayed, amplified and sent to the RF input port of the amplitude modulator.

Purpose of the band-pass filter is to separate the actuated mechanical mode from the rest of the measurement spectrum. We use a FPGA-based digital filter (Red Pitaya 125) to implement a variable band-pass filter with variable phase delay. The filter is implemented via an integrated IQ module which is programmed through a python open-source software module [63]. The center frequency of the filter is set to $\Omega_{fb}^{BP}/2\pi = 132.34$ kHz with the bandwidth $\Gamma_{fb}^{BP}/2\pi = 4.8$ kHz. The phase of the filter is adjusted according to the theory introduction to yield $arg(\chi_{fb}) \approx \pi/2$, which approximately corresponds to the oscillator velocity. The phase delay is found experimentally. We set a fixed gain and sweep the phase with step of 1 deg. until the maximal cooling is achieved.

The band-passed signal is amplified on a low noise pre-amplifier (SRS SR 560). The gain can be set from 1 to 50 000 and the output saturates at $10\,V_{pp}$. Filtered and amplified signal is sent to the fiber amplitude modulator (iXBlue MXAN-LN-10).

Figure 5.3 shows the S_{21} transfer function of the variable bandpass filter, measured with the electronic network analyser (Agilent E5061B).

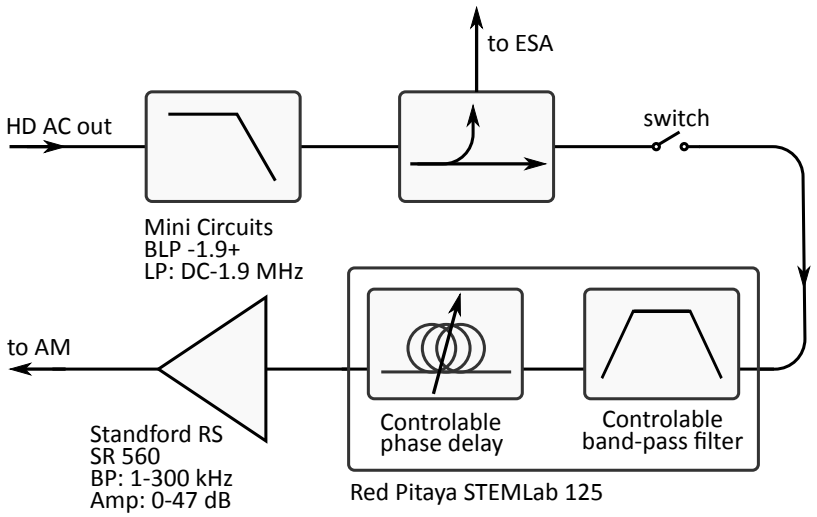

Figure 5.2: Block diagram of the feedback electronic circuit.

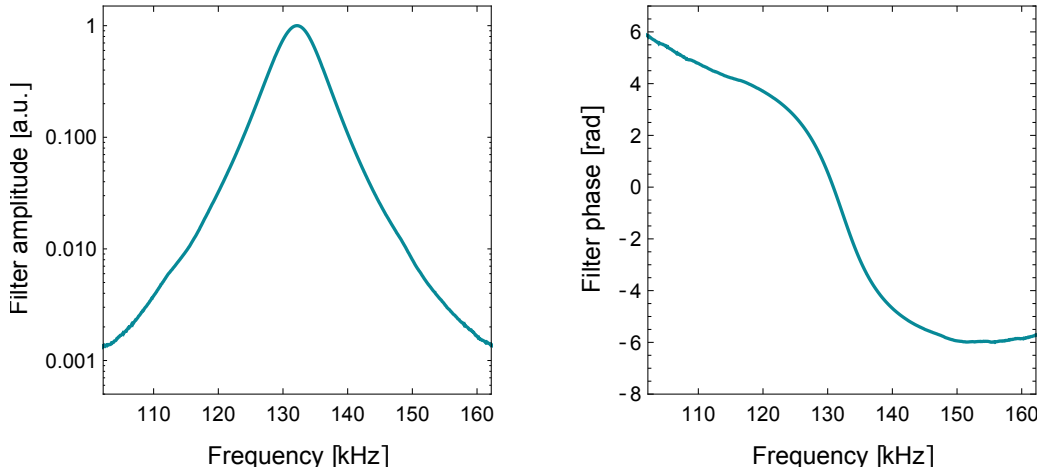

(a) (b)

Figure 5.3: Measurement of the variable band-pass filter transfer function, (a): filter amplitude response, (b): filter phase response with arbitrary phase offset. The filter phase response is a limiting factor for high effective cooling. Due to the broadening of the effective mode resonance $\Gamma_{eff} = \Gamma_m(1 + G_{fb})$ at very high cooling gains, the tails of the highly cooled mode experience non-optimal phase shift leading to heating instead of cooling.

5.4 Experimental results

This section provides with the results of the feedback cooling experiment. Applying the feedback to the trampoline resulted in in-loop displacement PSD shown in figure 5.4. The effective temperature as a function of the feedback gain is plotted in figure 5.6. System parameters are summarised in table 5.2.

Data acquisition

The power spectral densities presented in this chapter were acquired with electronic spectrum analyser Agilent N9000A with resolution bandwidth set to $RBW = 1$ Hz. Each trace was averaged 40 times. The feedback cooling experiment is conducted as follows.

Firstly, we lock the cavity length to be resonant with the laser probe beam of input power $P_{in} = 100\,\mu$W. Secondly, we lock the phase in homodyne detection, so the measurement outcome corresponds to the phase quadrature of probe beam (relative phase of $\pi/2$ between probe and LO beams). The LO optical power is $P_{LO} = 1.2\,$mW. At this point we can perform cooling

and record the displacement spectrum of the oscillator. The feedback cooling is initialized by switching on the switch in the electronic feedback circuit.

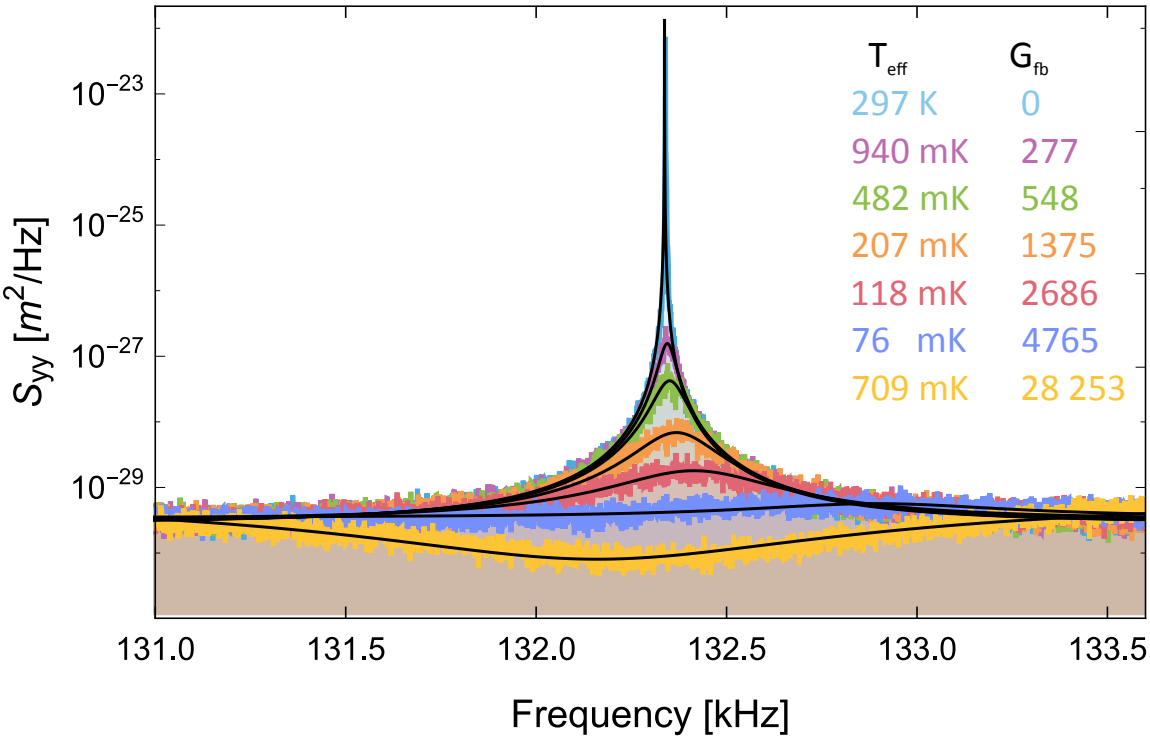

Figure 5.4: In-loop displacement spectrum of the mechanical oscillator fundamental mode under feedback actuation (color traces). The light blue trace acquired with the cooling gain switched off is used to calibrate the measured power spectrum to the displacement units as described in the main text. Calibrated in-loop displacement spectrum is fitted with Eq.5.11 (black lines). The plot legend shows inferred effective temperature T_{eff} and corresponding feedback gain G_{fb} for each trace. The bottom orange trace shows the effect of noise squashing due to the feedback gain being larger than SNR ($G_{fb} > SNR$).

Effective temperature of feedback cooled oscillator

Figure 5.6 shows inferred effective temperature as a function of the feedback gain G_{fb}. Parameters Ω_m, G_{fb}, and noise PSD are obtained from fitting measured (in-loop) spectra $S_{yy}(\Omega)$ given by eq. 5.11, where $\Gamma_m = 2\pi \cdot 0.13\,\mathrm{Hz}$ obtained from a ring-down measurement is set as a parameter. Fitted parameters are then entered into the displacement spectrum $S_{xx}(\Omega)$ given by Eq. 5.10 and the effective temperature is calculated with the relation provided

by the equipartition theorem

$$T_{eff} = \frac{m_{eff}\Omega_m^2}{k_B 2\pi} \int S_{xx}(\Omega)\mathrm{d}\Omega. \tag{5.35}$$

The maximum cooling was achieved with a feedback gain $G_{fb} = 4765$, yielding the effective temperature $T_{min} = 76\,\mathrm{mK}$. The corresponding thermal occupancy calculated with Eq.5.24 $\langle n_m \rangle \sim 150 \cdot 10^3$. Cooling to lower temperature was limited by imprecision noise in the measurement, which could in principle be lowered by higher probe powerpower. Such an improvement was not possible in this setup, since higher optical powers induce cavity to undergo instability and jump out of lock. Further analysis needs to be done to investigate this behaviour, which might likely stem from the inefficiency of the home-built PI (servo) controller & amplifier employed in the cavity locking.

Calibration of the displacement spectra

Eq. 5.35 also provides us with calibration of the measured voltage PSD to the units of mechanical displacement. As discussed in the section 4.6, the voltage fluctuations measured by the spectrum analyser are related to the oscillator displacement as

$$S_{VV}(\Omega) \approx \underbrace{\frac{K(\Omega_m)}{\Omega_m^2}\frac{g_0^2}{x_{zpf}^2}}_{cal} S_{xx}(\Omega), \tag{5.36}$$

where we used $cal = (K(\Omega_m)g_0)/(\Omega_m^2 x_{zpf}^2)$ to denote all constant terms, that reflect the optomechanical transduction and the detection-amplification chain. If the temperature is known, combining the Eqs.5.35 and 5.36 directly relate the area under the measured trace with the oscillator displacement. The calibration constant *cal* is obtained from the measured power spectrum with $G_{fb} = 0$ at temperature $T_{eff} = T_0 = 296.5\,\mathrm{K}$. Then we use the calibration constant and Eq. 5.36 to rescale all measured traces $S_{VV}(\Omega)$ in figures 5.4 and 5.5 to the displacement units.

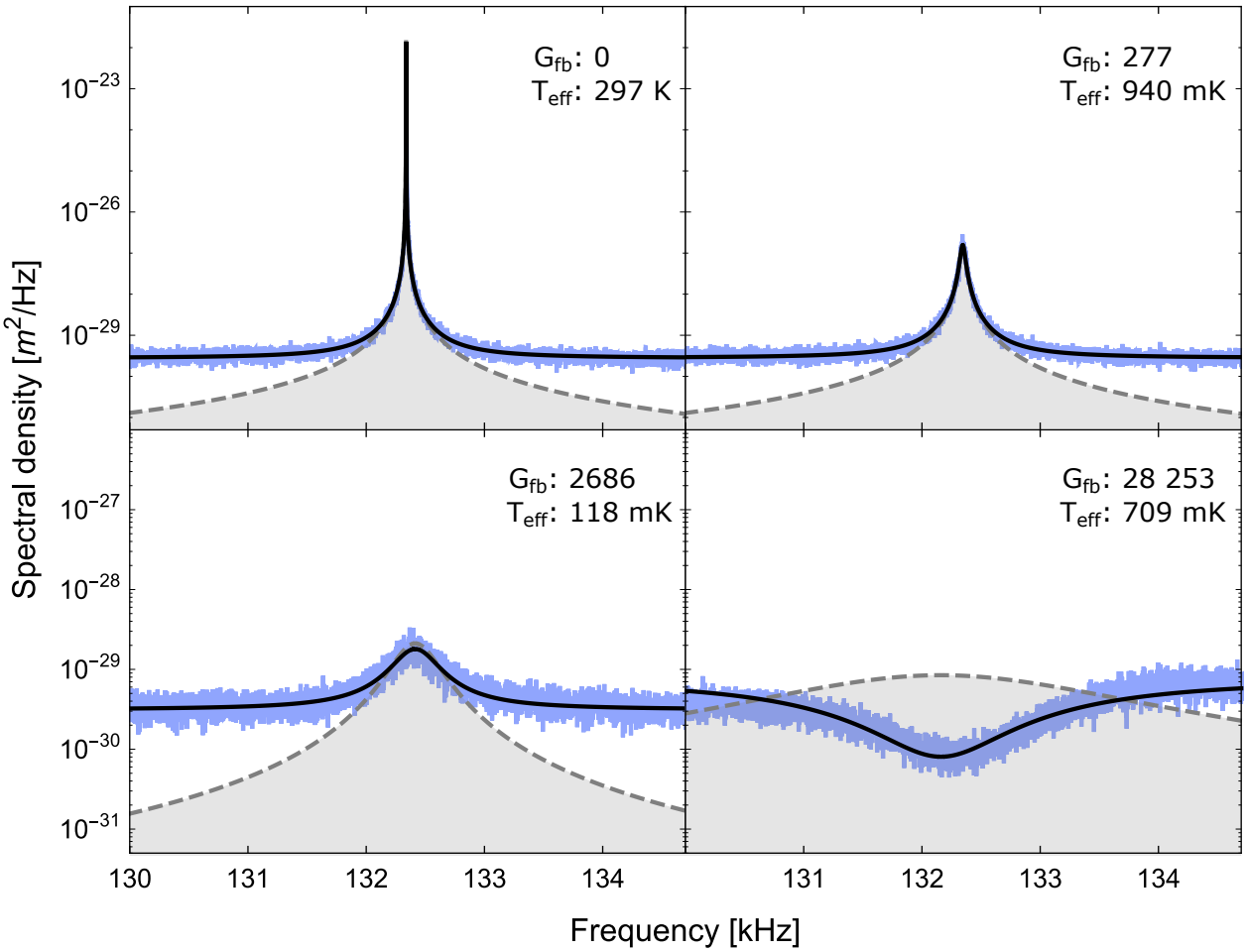

Figure 5.5: Power spectral density of the mechanical oscillator under the feedback actuation with various gains G_{fb}. Measured in-loop displacement spectra S_{yy} (blue traces) are fitted by Eq.5.11 (black lines). Fitted parameter are then used to plot the corresponding out-of-loop spectrum S_{xx} defined with Eq.5.10. Suppression of the thermal noise below the measurement noise - squashing is apparent in the bottom right plot.

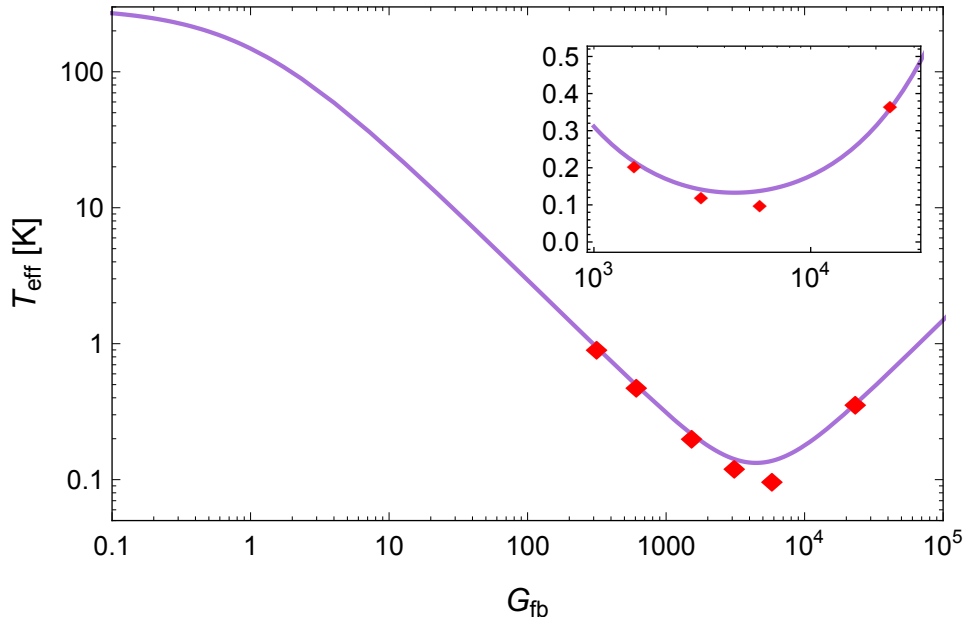

Figure 5.6: The inferred effective temperature of the fundamental mode as a function of the feedback gain (red diamonds). The purple line shows the effective theoretical temperature as a function of the feedback gain (Eq.5.32) corresponding to SNR = 70.9 dB measured in the absence of feedback actuation.

Symbol	Expression	Value	Measurement method
λ		1550 nm	Laser controller readout.
P_{in}		100 μW	Measured by optical power meter.
κ		$2\pi \cdot 492$ MHz	Calibration measurement (Sec. 4.3.1).
κ_{ex}		$2\pi \cdot 475$ MHz	Calibration measurement (Sec. 4.3.1).
η_c	κ_{ex}/κ	96.5 %	Inferred form κ and κ_{ex}.
T_0		296.5 K	Reading from a thermistor.
Ω_m		$2\pi \cdot 132.6$ kHz	Fit to the Brownian noise peak.
Γ_m		$2\pi \cdot 0.13$ Hz	Mechanical ring down measurement.
Q_m	Ω_m/Γ_m	10^6	Inferred from Ω_m and Γ_m.
$n_{th}(T_0)$	$k_B T_0/\hbar\Omega_m$	$4.7 \cdot 10^7$	Inferred from T_0 and Ω_m.
m_{eff}		3.56 ng	Inferred from COMSOL simulation
g_0		$2\pi \cdot 0.75$ Hz	Calibration measurement (Sec. 4.6).
p		$3.6 \cdot 10^{-6}$ mbar	Readout from a pressure gauge.

Table 5.2: Parameters of the optomechanical system.

5.5 Conclusion

In this chapter, we presented a theoretical analysis of the feedback cooling protocol and its implementation to our system consisting of a tethered membrane nano-oscillator inside a Fabry Pérot cavity. With this experiment, we introduced a new optomechanical platform into our research group, previously focused on experiments with micro toroid resonators [40, 64, 65].

We achieved cooling of the fundamental mode from the initial phonon occupancy at room temperature $\langle n_{th} \rangle = 4.7 \cdot 10^7$ down to $\langle n_m \rangle \sim 150 \cdot 10^3$ corresponding to the effective mode temperature $T_{eff} = 76\,\mathrm{mK}$. Further cooling was limited by SNR of the in-loop displacement spectrum which resulted in squashing of the measurement noise instead of mode cooling with high feedback gain ($G_{fb} >$ SNR). The SNR can be improved in several ways. One could simply increase the probe beam optical power, which was in our case prohibited by cavity instabilities. The reason why such instabilities make the cavity go out of lock need to be further investigated. Improvements can be pursed in the cavity mechanical stability and PDH electronics stabilizing the cavity length, especially the home-built PI (servo) controller & amplifier. An alternative route to increase the SNR would be represented by moving to a higher-finesse cavity.

Probing the mechanical motion with phase-squeezed light would result in higher SNR as well. This method was demonstrated in our group in the case of feedback cooling of a micro-toroid resonator [40]. Implementing this method in our scheme would require careful inspection of the losses in the system. The current cavity design is favorable in this direction, with single-sided excitation and high coupling efficiency $\eta_c \approx 98\,\%$. However, some changes including separation of the probe beam from a cooling beam would be required to avoid optical losses on the most inefficient component, e.g. intensity modulator. Finally, a squeezed-light source at 1550 nm is already available in our group [66].

Significant room for improvement lays in the optimization of the optomechanical transduction. Current cavity design allows only limited possibilities to align the trampoline chip inside the optical cavity.

It is important to note, that cooling to the ground state from room temperature is a major challenge for oscillators with resonance frequency below 1 MHz (it is challenging for oscillators with even much higher frequencies). An average occupancy of one phonon corresponds to cooling of the mechanical mode to temperature $T_{gs} = ln(2)\hbar\Omega_m/k_B \approx 4.4\,\mu\mathrm{K}$, where we took into account the resonance frequency of the trampoline fundamental mode $\Omega_m \approx 130\,\mathrm{kHz}$. This would require resolving the oscillator motion with SNR of 162.6 dB and corresponding feedback gain $G_{fb} \approx 1.3 \cdot 10^8$, which is four or-

ders of magnitude higher than what we achieved. Under such feedback gain the effective damping rate Γ_{eff} broadens from a room temperature value $\Gamma_m/2\pi \approx 0.1\,\mathrm{Hz}$ to hundreds of megahertz. This would require the feedback gain and delay phase to be uniform over a large bandwidth. Therefore, ground state cooling of membranes similar to ours is a great challenge and was not demonstrated without cryogenic pre-cooling up to date.

Chapter 6

Quantum-enhanced magnetometry

6.1 Introduction

In this chapter we present a proof-of-concept demonstration of the squeezed light enhanced magnetic field sensing with a cavity optomechanical magnetometer. The ability to detect a magnetic field with high sensitivity plays an important role in multiple fields including magnetic resonance imaging [67], geology, archaeology, material testing and medicine [68].

Cavity optomechanical field sensors serve as effective magnetometers with high sensitivity under ambient conditions, a spatial resolution in the order of tens of microns and microwatt optical power requirements [69]. They are based on a magnetostrictive effect, where the magnetic field induces deformation in the material, which is transduced to the resonator structure. The resulting motion modifying the cavity condition is read out optically. Compared with other magnetometers based on the magnetostrictive effect [70, 71], the cavity magnetometer benefits from the resonant enhancement of the optical and mechanical response. Currently, the cavity optomechanical magnetometers operate at the thermomechanical noise limit, achieveing a sensitivity up to $\sim 500\,\mathrm{pT}/\sqrt{\mathrm{Hz}}$ with a bandwidth in the kilohertz range, and a sensitivity comparable to theat of SQUIDS was theoretically predicted [72]. During work on this thesis, the design of the silicon on-chip toroid magnetometers improved, allowing a scalable production. Early designs of cavity magnetometers (the one presented in this work) incorporated grain of magnetostrictive Terfenol-D manually placed and epoxy-bounded to the toroidal structure, which significantly reduced the fabrication scalability. Recently, the method of sputter coating of a magnetostrictive film onto high quality toroidal micro-resonators was demonstrated, allowing reproducable and scalable fabrication [73].

The magnetometry experiment described here was done in collaboration with the group of Warwick P. Bowen at University of Queensland. In particular with Beibei Li who, visited DTU for three months and brought the chip with magnetometers and tapered fibres used to couple the light into the micro-resonator. By the time of the magnetometry experiment, the squeezed light source used in this work was already built on the optical table. Details about the squeezer can be found in the PhD thesis of Clemens Schäfermeier [74], alternatively the squeezed light source benchmarking can be found in [75].

The squeezing enhanced magnetic field sensing is the most recent experiment done in our group in the series of experiments interfacing squeezed light with micro-resonators. The foundations of the experiments in optomechanics were placed by the PhD work of Ulrich B. Hoff in 2015 [76]. The first experimental work studied the quantum-enhancement of mechanical transduction

sensitivity in microcavity optomechanics [64]. The next contribution to the field was theoretical study determining the theoretical limits to squeezing-enhanced measurement sensitivity of mechanical motion in a cavity optomechanical system [77] followed by the squeezed light enhanced feedback cooling of the micro-toroid [40].

6.2 Publication

This section was published in Optica with the title of "Quantum enhanced optomechanical magnetometry " as follows [65].

Author contributions

U.L.A. and W.P.B. conceived the idea while B.B.L., J.B., U.B.H., L.S.M., T.G., W.P.B., U.L.A. devised the experiment; B.B.L. and J.B. performed the experiment with the help from U.B.H, T.G., L.S.M., C.S., S.F. and V.P.; B.B.L. and J.B. analyzed the data with help from W.P.B.; B.B.L. and J.B. wrote the manuscript with help from W.P.B.; All authors contributed to the discussion and provided useful feedback on the paper; W.P.B. led the device fabrication part and U.L.A. led the optical measurement part; T.G., W.P.B. and U.L.A. supervised the whole work.

Bei-Bei Li and Jan Bílek contributed equally to this work.

Research Article Vol. 5, No. 7 / July 2018 / Optica 850

Quantum enhanced optomechanical magnetometry

Bei-Bei Li,[1,2] Jan Bílek,[3] Ulrich B. Hoff,[3] Lars S. Madsen,[1] Stefan Forstner,[1] Varun Prakash,[1] Clemens Schäfermeier,[3] Tobias Gehring,[3] Warwick P. Bowen,[1,*] and Ulrik L. Andersen[3]

[1]School of Mathematics and Physics, The University of Queensland, St Lucia, QLD 4072, Australia
[2]Qian Xuesen Laboratory of Space Technology, Beijing 100094, China
[3]Department of Physics, Technical University of Denmark, Fysikvej 309, 2800 Kgs. Lyngby, Denmark
*Corresponding author: w.bowen@uq.edu.au

Received 30 April 2018; revised 21 June 2018; accepted 22 June 2018 (Doc. ID 330447); published 12 July 2018

The resonant enhancement of both mechanical and optical response in microcavity optomechanical devices allows exquisitely sensitive measurements of stimuli, such as acceleration, mass, and magnetic fields. In this work, we show that quantum correlated light can improve the performance of such sensors, increasing both their sensitivity and their bandwidth. Specifically, we develop a silicon-chip-based cavity optomechanical magnetometer that incorporates phase squeezed light to suppress optical shot noise. At frequencies where shot noise is the dominant noise source, this allows a 20% improvement in magnetic field sensitivity. Furthermore, squeezed light broadens the range of frequencies at which thermal noise dominates, which has the effect of increasing the overall sensor bandwidth by 50%. These proof-of-principle results open the door to apply quantum correlated light more broadly in chip-scale sensors and devices.

OCIS codes: (120.4880) Optomechanics; (270.6570) Squeezed states; (140.3945) Microcavities; (140.4780) Optical resonators; (280.4788) Optical sensing and sensors; (130.3120) Integrated optics devices.

https://doi.org/10.1364/OPTICA.5.000850

1. INTRODUCTION

Cavity optomechanics [1–3] has attracted increasing research interest for both fundamental studies and practical applications. Strong radiation pressure coupling between high quality mechanical and optical resonances has enabled the demonstration of a range of interesting quantum behaviors, such as ground state cooling of macroscopic mechanical oscillators [4–7], quantum squeezing of mechanical motion [8–11], and the production of squeezed light [12,13], while the combination of resonance enhanced mechanical and optical response [14] has enabled precision sensors [15] ranging from kilometer-sized laser interferometer gravitational wave detectors [16,17] to micro/nanoscale silicon-chip-based force [18], mass [19], acceleration [20,21], and magnetic field [22–25] sensors.

The precision of cavity optomechanical sensors is generally constrained by three fundamental noise sources: thermal noise from the environment, shot noise from the photon number fluctuations of the light used to probe the system, and quantum backaction noise arising from the radiation pressure of the probe light. The noise floor can be engineered using quantum correlated light. For instance, squeezed light [26–28] allows the shot noise to be suppressed [29], thereby improving the sensitivity if the shot noise is dominant. Squeezed light has been used, for example, to improve the precision of gravitational wave interferometry in both the Laser Interferometer Gravitational-Wave Observatory (LIGO) and the GEO600 [30–32], and it has also been used in nanoscale measurements of biological systems [33], laser beam positioning [34,35], and magnetic field measurement using atomic magnetometers [36,37]. In cavity optomechanics, it has been used to enhance measurements of thermal noise [38], improve both feedback [39] and sideband cooling [40], and study the backaction from the radiation pressure force [41]. However, it has not previously been used to improve cavity optomechanical sensors of external stimuli. Here, we demonstrate the first application of squeezed light in such a sensor, specifically, in a cavity optomechanical magnetometer [22,23]. At frequencies where shot noise is dominant, squeezed light suppresses the noise floor, improving the magnetic field sensitivity. Moreover, by increasing the range of frequencies over which thermal noise is dominant, the sensor bandwidth is also increased. A squeezed light enhanced sensor bandwidth [42] is of importance in applications that need good sensitivity in a broadband range, e.g., in magnetic resonance imaging.

2. THEORETICAL ANALYSIS

Figure 1(a) shows a conceptual schematic of a cavity optomechanical magnetometer, comprised of an optical cavity, coupled to a mechanical oscillator. The mechanical oscillator is driven by a force F_B induced by a magnetic field via the magnetostrictive effect [22] along with thermal and backaction noise forces. The mechanical motion of the oscillator changes the cavity length and, thus, the optical resonance. This modulates the phase of an injected squeezed probe field and can therefore be read out via an optical phase measurement. In our case, the optical cavity is a microtoroid, whose circumference is modified by mechanical

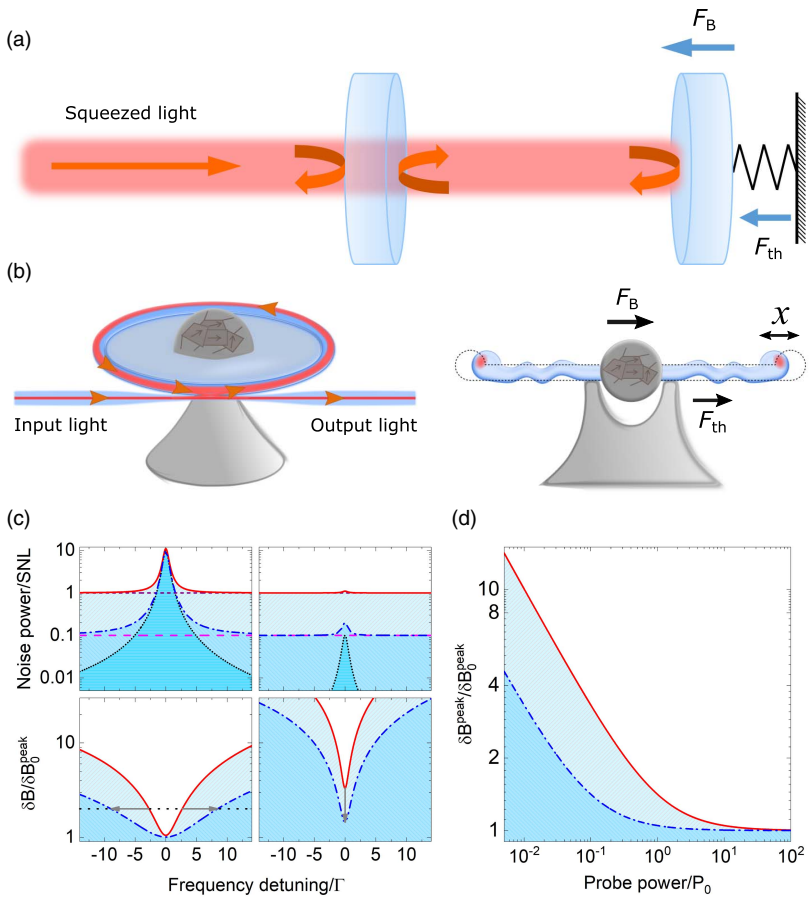

Fig. 1. (a) Conceptual schematic of a cavity optomechanical system probed with squeezed light. Here, F_B and F_{th} denote the magnetic field induced force and the thermal force on the mechanical oscillator. (b) Left: a schematic of a microtoroid magnetometer coupled with a nanofiber. Right: the cross section of a microtoroid, of which the optical field is distributed along the inner surface. The mechanical motion changes the circumference of the cavity and, thus, shifts the optical resonance. (c) and (d) Theoretical result for squeezing enhanced performance of the magnetometer. Here, we use a squeezing factor of 10 dB. In (c), top-left and bottom-left plots correspond to the strong probe power case, where $P = 10P_0$, with P_0 defined as the power when the thermal noise on mechanical resonance equals the shot noise level (SNL), i.e., $\bar{n} = 1/(16\eta C)$, while top-right and bottom-right plots correspond to the weak probe power case, where $P = 0.1P_0$. (c) Top left and top right, the noise power spectrum normalized to the SNL. Black short-dotted curve, thermal noise; purple short-dashed line, vacuum shot noise for coherent probe; magenta dashed line, squeezed vacuum noise for squeezed probe; red solid curve, total noise for coherent probe; blue dash-dotted curve, total noise for squeezed probe. Bottom left and bottom right, the sensitivity as a function of frequency for coherent (red solid curves) and squeezed (blue dash-dotted curves) probe, respectively, normalized to δB_0^{peak}, which is the peak sensitivity for the squeezed probe in the strong probe power case. (d) The peak sensitivity δB^{peak} (normalized to δB_0^{peak}) as a function of the probe power P for coherent (red solid curve) and squeezed (blue dash-dotted curve) probes, respectively.

motion, as illustrated in Fig. 1(b). Our experiments operate in the unresolved sideband regime, where the optical decay rate κ is much larger than the mechanical resonance frequency Ω. In this regime, the thermal force noise dominates the backaction noise when $\bar{n} > V_{anti}^{cavity} C$ [3], where $\bar{n}$ is the thermal phonon occupancy of the mechanical oscillator, V_{anti}^{cavity} is the variance of the anti-squeezed field in the optomechanical cavity, and C is the optomechanical cooperativity, which quantifies the strength of radiation pressure optomechanical coupling relative to the mechanical and optical dissipation rates and is proportional to the probe laser power. For the few megahertz frequencies we use, $\bar{n} \sim 10^6$ at room temperature; while with the optical and mechanical properties of our optomechanical microresonator, and for the maximum optical power, we use $C \sim 1000$. Consequently, the mechanical force noise is dominated by thermal noise, and we neglect backaction noise henceforth.

The displacement x of the mechanical oscillator in response to an external force F is quantified in the frequency domain by the mechanical susceptibility $\chi(\omega)$. To illustrate the physics, we consider the simple case of a single mechanical resonance, for which $\chi(\omega) = 1/(m_{eff}(\Omega^2 - \omega^2 - i\omega\Gamma))$, where m_{eff} is the effective mass of the mechanical oscillator, and Γ is its damping rate, enhancing the mechanical response to near resonant forces [see top left and top right of Fig. 1(c)]. Quite generally, in cavity optomechanical sensors, away from resonance, optical shot noise is dominant, allowing squeezed light enhanced sensitivity; while for

a single-sided cavity in the unresolved sideband regime, thermal noise dominates shot noise at resonance if $\bar{n} > 1/(16\eta C)$, where η is the optical detection efficiency.

A magnetic field is resolvable when the signal it induces is larger than the total noise floor. Neglecting backaction noise, this leads to a minimum detectable force δF,

$$\delta F = \sqrt{2m_{\mathrm{eff}}\Gamma k_{\mathrm{B}} T}\left[1 + \frac{V_{\mathrm{sqz}}}{16\bar{n}\eta C}\left|\frac{\chi(\Omega)}{\chi(\omega)}\right|^2\right]^{1/2}. \quad (1)$$

In this equation, k_{B} and T are the Boltzmann constant and the temperature, respectively. The first term in the bracket on the right hand side represents the thermal noise, while the second term represents the optical noise with V_{sqz} as the variance of the detected squeezed field. Introducing an actuation constant $c_{\mathrm{act}} = F/B$, which characterizes how well the magnetic field B is converted into an applied force F on the mechanical oscillator [22], the magnetic field sensitivity is $\delta B = \delta F/c_{\mathrm{act}}$.

From Eq. (1), we see that the peak sensitivity occurs on mechanical resonance. In the case where thermal noise is dominant at mechanical resonance frequency ($\bar{n} > 1/16C$), squeezed light does not significantly change the peak sensitivity, instead extending the frequency range over which thermal noise dominates, and, therefore, the sensor bandwidth [bottom left of Fig. 1(c)]; while in the case where optical noise is dominant on resonance ($\bar{n} < 1/16C$), both the peak sensitivity and bandwidth are improved by squeezed light [bottom right of Fig. 1(c)]. The saturation of sensitivity to the optimal (thermal noise limited) sensitivity as probe powers increase is shown in Fig. 1(d). It can be seen that squeezed light reduces the probe power required to reach the optimal sensitivity. We note that similar sensitivity and bandwidth improvements could also be achieved by increasing the probe power. However, this strategy cannot be pursued infinitely due to deleterious effects from the probe, such as detector saturation and absorption heating of the optomechanical device. Of particular relevance to optomechanics, at high probe power, dynamic backaction causes parametric instabilities that degrade sensitivity [43]. These instabilities are especially problematic for the high quality mechanical resonators desirable for precision optomechanical sensing.

3. EXPERIMENT AND RESULTS

A. Measurement of the Optomechanical System

In our experiments, the optomechanical magnetometer is a microtoroid cavity embedded with a grain of magnetostrictive material (terfenol-D) [22,23], as sketched in Fig. 1(b). In such magnetometers, the magnetic field deforms the microcavity via the magnetostrictive expansion and shifts the optical resonance. In the case of an alternating current (AC) magnetic field, the magnetostrictive material exerts a periodic force on the mechanical oscillator, which can drive the mechanical motion of the toroid. When the microcavity is excited on optical resonance, the mechanical motion translates into a pure phase modulation of the transmitted light at the mechanical frequency, which is read out with a homodyne detector and recorded using a spectrum analyzer.

The measurement setup for squeezed light enhanced magnetometry is shown in Fig. 2. A neodymium-doped yttrium aluminum garnet (Nd:YAG) laser is used to produce squeezed light at a wavelength of 1064 nm. Phase-squeezed light is generated through a parametric down conversion process in a 10 mm

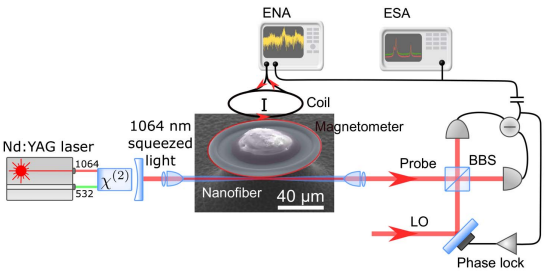

Fig. 2. Measurement setup for squeezed light enhanced cavity optomechanical magnetometry. Squeezed light at a wavelength of 1064 nm is used to probe the magnetometer. The magnetometer is a microtoroid with terfenol-D embedded inside, as shown in the scanning electron microscope picture. The optical Q factor of the toroid mode is about 1×10^6, corresponding to an optical damping rate of $\kappa/2\pi \sim 300$ MHz. The mechanical motion of the toroid is measured by performing homodyne detection. LO, local oscillator; BBS, balanced beam splitter, comprised of two polarization beam splitters and a half wave plate; ESA, electronic spectrum analyzer; ENA, electronic network analyzer.

periodically poled potassium titanyl phosphate (PPKTP) crystal enclosed in a linear cavity [39]. As shown in Fig. 2, both the 532 nm light (the pump light) and the 1064 nm light (the seed light) are injected into the cavity. To generate phase-squeezed light, the pump phase is locked to the seed beam amplification. The light is coupled into the microtoroid evanescently through an optical nanofiber with a diameter of about 700 nm. The optical resonance of the cavity is thermally tuned to match the wavelength of the laser. The cavity phase is actively locked using a feedback system [44]. A coil is used to produce an AC magnetic field to test the magnetic field response of the magnetometer. The mechanical motion of the toroid is measured by performing homodyne detection. The balanced homodyne detector combines two inputs: a relatively weak probe, which couples with the microcavity, and a relatively strong local oscillator (LO), which comes from the same laser but without going through the microcavity. An electronic spectrum analyzer (ESA) is used to record the noise power spectrum. In order to measure the response of the magnetometer to magnetic fields at different frequencies, we drive the coil with the output of an electric network analyzer (ENA) and measure the magnetic field response at each frequency with the same ENA.

B. Characterization of the Squeezed Light

To characterize the squeezed state transmitted through the fiber, we decouple the microtoroid from the nanofiber and measure the homodyne detection signal of the field quadratures by linearly sweeping the LO phase θ. As shown in the dark gray curve in Fig. 3(a), when θ is swept continuously, the noise power changes periodically, following the equation $V = V_{\mathrm{sqz}} \cos^2\theta + V_{\mathrm{anti}} \sin^2\theta$, with V_{anti} being the anti-squeezed quadrature variance. The black solid curve is the fitted result based on this equation, yielding $V_{\mathrm{sqz}} = 0.56$ and $V_{\mathrm{anti}} = 6.3$. Ideally, the product $V_{\mathrm{sqz}} V_{\mathrm{anti}} = 1$, satisfying the Heisenberg uncertainty limit, but, in reality, this limit is not reached, due to loss of the squeezed light during propagation in the setup. The squeezed light source has a squeezing of about 11 dB (corresponding to a squeezing factor of $V_{\mathrm{sqz}} = 0.08$), which

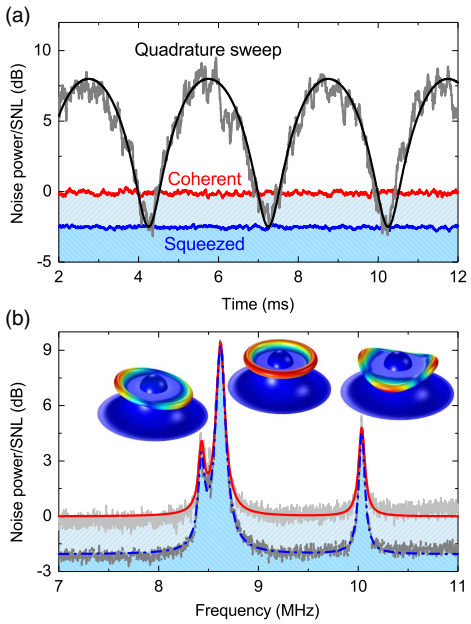

Fig. 3. (a) Characterization of the squeezed state before coupling to the microtoroid. The dark gray curve shows the noise power when sweeping the LO phase continuously with its theoretically fitted result shown in the black solid curve. The red and blue solid curves are the noise power with coherent and squeezed probes when the LO phase is locked at the phase quadrature. (b) The measured noise power from the microtoroid with both coherent (light gray curve) and squeezed (dark gray curve) probes, respectively. The red solid and the blue dashed curves are the fitted results for the measured ones. The three peaks correspond to three mechanical resonance modes (from left to right: tilting mode, flapping mode, and crown mode) with the profiles shown in the inset, obtained using COMSOL Multiphysics.

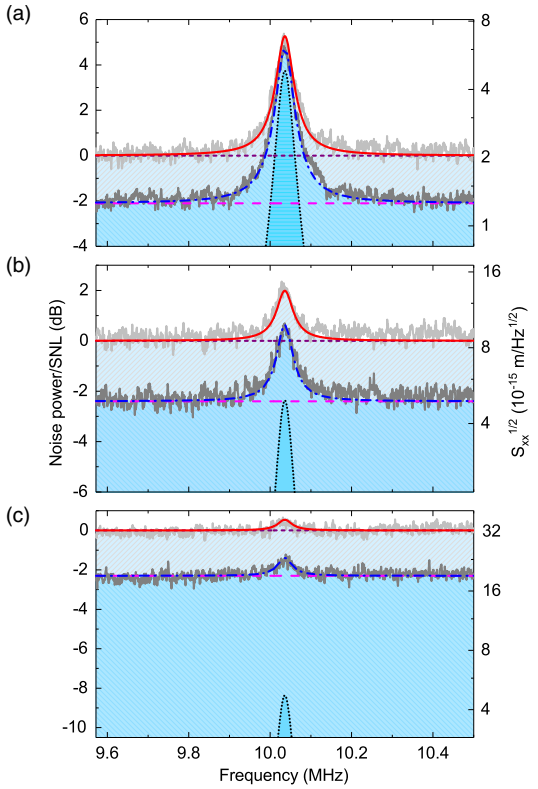

Fig. 4. Characterization of the noise power spectra around the crown mode, under different probe powers: (a) 80 μW, (b) 20 μW, and (c) 5 μW. The light gray and dark gray curves are the measured noise power for coherent and squeezed probes, respectively. The other curves are the theoretically fitted ones: black short-dotted curves, thermal noise; purple short-dashed lines, vacuum shot noise with coherent probe; magenta dashed lines, squeezed vacuum noise with squeezed probe; red solid curves, total noise for the coherent probe; and the blue dash-dotted curves, total noise for the squeezed probe. On the right axes of the figures, it shows the corresponding displacement amplitude spectral density $S_{xx}^{1/2}$. The mechanical damping rate is extracted from the linewidth of the mode in the thermal noise spectrum to be $\Gamma/2\pi = 42$ kHz. The effective mass of the crown mode is determined to be $m_{\text{eff}} = 6.06$ ng obtained from COMSOL modeling. The displacement amplitude spectral density $S_{xx}^{1/2}$ is plotted on the right axes of the figures.

is degraded by the inefficiencies in the system. These inefficiencies include: loss on the escape from the squeezing cavity, coupling loss from free space into fiber, propagation loss in the nanofiber, coupling loss from free space to the fiber, loss in propagation through optical components, and photodetector inefficiency. Transmission losses of ∼37% through the nanofiber are the dominant source of loss. These losses could be straightforwardly addressed in the future by using a more adiabatic tapered nanofiber, which has been shown to allow transmission losses under 1% [45]. The overall loss, before coupling to the optomechanical magnetometer, of 54% degrades V_{sqz} from 11 to 2.5 dB. The noise power reaches its minimum when locked at the phase quadrature, and we lock θ to that quadrature henceforth. The red and blue curves in Fig. 3(a) show the noise power for phase quadrature measurement of coherent and squeezed probes, respectively.

C. Noise Spectra with Coherent and Squeezed Probes

The squeezed field is coupled into the microcavity through the nanofiber. A trade-off exists when choosing the coupling rate. Critical coupling, where the coupling rate κ_1 equals the intrinsic loss rate κ_0, provides the maximum signal transduction. However, with this choice of coupling, the probe field is entirely absorbed within the cavity, completely removing any squeezing, and, therefore, prohibiting squeezed light enhancement. Here, we choose a compromise coupling rate $\kappa_1 = 0.52\kappa_0$, which maintains high intracavity power and significant squeezing levels. This coupling rate corresponds to a transmission of about 90% on optical resonance, and this additional 10% loss causes a degradation of squeezing from 2.5 to 2.2 dB. The noise power with both coherent and squeezed probes in the frequency range of 7–11 MHz is measured, as shown in the light gray (for coherent probe) and gray (for squeezed probe) curves in Fig. 3(b). With a probe power of 80 μW, three peaks appear in this frequency range of the noise spectrum, corresponding to three thermally excited mechanical resonance modes. We use COMSOL Multiphysics simulations to identify these three modes as the tilting mode, flapping mode, and crown mode with the corresponding mode profiles shown in the inset. It can be seen that over the frequency

ranges where the optical noise dominates, the noise floor is suppressed by up to 2.2 dB by squeezed light, while it is left essentially unchanged when thermal noise dominates.

In order to carefully study the effect of the probe power on the noise spectrum, in the following, we focus on the crown mode with mechanical resonance frequency of $\Omega/2\pi = 10.035$ MHz. This mode is chosen due to the particularly clean noise power spectrum in its vicinity. Figure 4(a) shows the noise (normalized to the shot noise level) in the vicinity of the crown mode with probe power $P = 80$ μW. As expected, in this case, the noise level remains unchanged by squeezing near the resonance frequency, where thermal noise is dominant and is suppressed away from resonance. As the probe power gradually decreases, the thermal noise drops relative to the shot noise. As shown in Figs. 4(b) and 4(c), the shot noise is dominant in the whole frequency range for probe powers of 20 and 5 μW. At these power levels, squeezing allows the noise floor to be suppressed over the entire frequency ranges. These results are consistent with the predictions in Fig. 1(c).

D. Squeezed Light Enhanced Magnetic Field Sensing

The magnetic field sensitivity of the magnetometer is then characterized. We first characterize the absolute sensitivity at a single frequency $\omega_{\mathrm{ref}}/2\pi = 8.615$ MHz. The inset of Fig. 5(a) shows the power spectrum at ω_{ref}, when the magnetometer is driven with a magnetic field with known strength B_{ref}. The sensitivity at this frequency can be derived from the signal-to-noise ratio (SNR) and B_{ref}, $\delta B_{\mathrm{ref}} = B_{\mathrm{ref}}/\sqrt{\mathrm{RBW} \times \mathrm{SNR}}$ [22], with RBW being the measurement resolution bandwidth. Figure 5(a) plots the sensitivity at this frequency as a function of the probe power. The red triangles and the blue circles represent the measured result for coherent and squeezed probes, respectively, with the error bars obtained by taking into account the fluctuation of about ±0.5 dB in the measured noise spectrum. As expected, the sensitivity is improved by squeezing at low probe power, where the shot noise is dominant, and reaches the same optimal sensitivity at high probe power, where the thermal noise is dominant, and in good agreement with theoretical fits. For instance, the sensitivity at 2.5 μW probe power is improved from 35.9 nT/$\sqrt{\mathrm{Hz}}$ to 29.2 nT/$\sqrt{\mathrm{Hz}}$, and thermal noise limited sensitivity is about 15.7 nT/$\sqrt{\mathrm{Hz}}$ for both coherent and squeezed probes. The sensitivity at ω_{ref} can be used along with the noise spectrum N_ω and network response R_ω to calibrate the sensitivity δB_ω over the whole frequency range, $\delta B_\omega = \delta B_{\mathrm{ref}}\sqrt{(N_\omega R_{\mathrm{ref}})/(N_{\mathrm{ref}} R_\omega)}$. This allows the effect of squeezing on bandwidth to be analyzed, as discussed in the following. For a probe power of 80 μW, the peak sensitivity in the whole frequency range is found to be about 5 nT/$\sqrt{\mathrm{Hz}}$ at $\omega/2\pi \sim$ 8.543 MHz for both coherent and squeezed probes.

The sensitivity is found to vary significantly over frequency ranges of around 10 kHz due to resonances in the response of terfenol-D, as shown in the sensitivity spectrum in the bottom-right inset of Fig. 5(b), and consistent with previous observations [22]. This precludes comparison of the magnetometer bandwidth as a function of squeezing to a simple theory. Instead, here, we analyze the squeezing dependence of the accumulated bandwidth, defined as the total frequency range, over which the sensitivity is better than a certain threshold value $\delta B_{\mathrm{thresh}}$ (see bottom-right inset). In Fig. 5(b), we plot the accumulated bandwidth for coherent (red solid curve) and squeezed (blue dash-dotted curve) probes at a probe power of 80 μW. It can be seen that, for each $\delta B_{\mathrm{thresh}}$, the accumulated bandwidth for the squeezed probe is greater than that for the coherent probe. The upper-left inset of Fig. 5(b) shows the accumulated bandwidth over the smaller frequency range of 0–70 kHz. Squeezed light expands the 3 dB bandwidth (corresponding to $\delta B_{\mathrm{thresh}} =$ 10 nT/$\sqrt{\mathrm{Hz}}$) by 50%, from 30 kHz (for coherent probe) to 45 kHz (for squeezed probe).

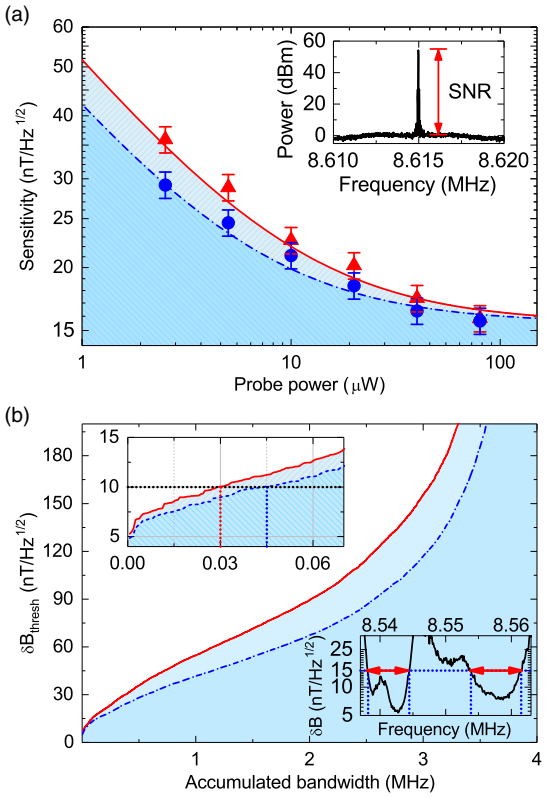

Fig. 5. Sensitivity and bandwidth improvement. (a) Sensitivity at the frequency of 8.615 MHz, as a function of the probe power. The red triangles and blue circles represent the measured results for coherent and squeezed probes, respectively. The error bars are obtained by taking into account the fluctuation in the noise power measurement. The red solid (coherent) and blue dash-dotted (squeezed) curves are the corresponding theoretical fitted result. The inset shows the power spectrum when the magnetometer is driven at this frequency with the peak denoting the signal induced by the magnetic field. (b) The accumulated bandwidth as a function of the threshold sensitivity for the coherent (red solid curve) and squeezed (blue dashed curve) probes, respectively. Top-left inset: the zoom-in of the accumulated bandwidth in the frequency range of 0–0.07 MHz, showing the 3 dB bandwidth of 30 kHz for the coherent probe and 45 kHz for the squeezed probe. Bottom-right inset: the sensitivity spectrum in the frequency range of 8.537–8.563 MHz, showing the definition of the accumulated bandwidth. For a threshold sensitivity of 15 nT/$\sqrt{\mathrm{Hz}}$, the accumulated bandwidth is defined as the sum of the frequency ranges within the two red arrows.

4. CONCLUSIONS

In summary, we have demonstrated the first application of quantum light in a microcavity optomechanical sensor. By probing a

cavity optomechanical magnetometer with phase squeezed light, the noise floor is suppressed by about 40%, allowing improved sensitivity by about 20% in the shot noise dominated regime, and a 50% enhancement in accumulated bandwidth from 30 to 45 kHz. Squeezed light further reduces the optical power required to reach the optimal sensitivity.

Our approach provides a way to improve the sensitivity of the cavity optomechanical magnetometer over a broad frequency range and also opens up possibilities for improving other optomechanical sensors, e.g., inertial sensors [20,21]. While a 20% improvement in sensitivity is relatively modest; recent advances in squeezing technologies [46–49] hold promise for more substantial improvements. For instance, with detected squeezing of 15 dB recently reported [49], a sensitivity improvement of a factor of 5.6 could potentially be realized. Moreover, squeezed light could be generated on the same silicon chip as the sensor itself, using radiation pressure induced optomechanical effects [12,13], nonlinear effects in optical resonators [50], or nonlinear waveguides [51]. Further improvements may be possible by optimizing the magnetometer design itself with sensitivities on the order of 100 $\mathrm{pT}/\sqrt{\mathrm{Hz}}$ reported in previous cavity optomechanical magnetometers [23]. Sensitivities in this range make cavity optomechanical magnetometers a promising candidate for a range of applications, such as on-chip microfluidic nuclear magnetic resonance for medical diagnosis [52] and magnetoencephalography [53], without the requirement for cryogenic systems that are necessary for other precision magnetometers, such as superconducting quantum interference device (SQUID)-based magnetometers [54,55].

Funding. Villum Fonden (13300); Danmarks Grundforskningsfond (bigQ); Danish Research Council (4184-00338B); Defense Advanced Research Projects Agency (DARPA) (QuASAR program); Australian Research Council (ARC) (DP140100734, FT140100650); Defence Science and Technology Group (DST Group) (CERA49, CERA50); University of Queensland (UQ) (2014001447); National Natural Science Foundation of China (NSFC) (11654003, 61705259).

Acknowledgment. We thank James Bennett, Rachpon Kalra, Christopher Baker, Andreas Sawadsky, Alexander Huck, Jonas Neergaard-Nielsen, and Halina Rubinsztein-Dunlop for the very helpful discussions. W. P. B. acknowledges the Australian Research Future Fellowship. B. B. L. acknowledges the support from the University of Queensland Postdoctoral Research Fellowship and Natural Science Foundation of China. T. G. acknowledges support from the Danish Research Council for Independent Research. Device fabrication was performed within the Queensland Node of the Australian Nanofabrication Facility.

Bei-Bei Li and Jan Bílek contributed equally to this work.

REFERENCES

1. T. J. Kippenberg and K. J. Vahala, "Cavity optomechanics: back-action at the mesoscale," Science **321**, 1172–1176 (2008).
2. M. Aspelmeyer, T. J. Kippenberg, and F. Marquardt, "Cavity optomechanics," Rev. Mod. Phys. **86**, 1391–1452 (2014).
3. W. P. Bowen and G. Milburn, *Quantum Optomechanics* (CRC Press, 2016).
4. A. D. O'Connell, M. Hofheinz, M. Ansmann, R. C. Bialczak, M. Lenander, E. Lucero, M. Neeley, D. Sank, H. Wang, M. Weides, J. Wenner, J. M. Martinis, and A. N. Cleland, "Quantum ground state and single-phonon control of a mechanical resonator," Nature **464**, 697–703 (2010).
5. J. Chan, T. P. M. Alegre, A. H. Safavi-Naeini, J. T. Hill, A. Krause, S. Groblacher, M. Aspelmeyer, and O. Painter, "Laser cooling of a nanomechanical oscillator into its quantum ground state," Nature **478**, 89–92 (2011).
6. J. D. Teufel, T. Donner, D. Li, J. W. Harlow, M. S. Allman, K. Cicak, A. J. Sirois, J. D. Whittaker, K. W. Lehnert, and R. W. Simmonds, "Sideband cooling of micromechanical motion to the quantum ground state," Nature **475**, 359–363 (2011).
7. D. J. Wilson, V. Sudhir, N. Piro, R. Schilling, A. Ghadimi, and T. J. Kippenberg, "Measurement-based control of a mechanical oscillator at its thermal decoherence rate," Nature **524**, 325–329 (2015).
8. A. Szorkovszky, A. C. Doherty, G. I. Harris, and W. P. Bowen, "Mechanical squeezing via parametric amplification and weak measurement," Phys. Rev. Lett. **107**, 213603 (2011).
9. E. E. Wollman, C. U. Lei, A. J. Weinstein, J. Suh, A. Kronwald, F. Marquardt, A. A. Clerk, and K. C. Schwab, "Quantum squeezing of motion in a mechanical resonator," Science **349**, 952–955 (2015).
10. J.-M. Pirkkalainen, E. Damskägg, M. Brandt, F. Massel, and M. Sillanpää, "Squeezing of quantum noise of motion in a micromechanical resonator," Phys. Rev. Lett. **115**, 243601 (2015).
11. F. Lecocq, J. Clark, R. Simmonds, J. Aumentado, and J. Teufel, "Quantum nondemolition measurement of a nonclassical state of a massive object," Phys. Rev. X **5**, 041037 (2015).
12. A. H. Safavi-Naeini, S. Grblacher, J. T. Hill, J. Chan, M. Aspelmeyer, and O. Painter, "Squeezed light from a silicon micromechanical resonator," Nature **500**, 185–189 (2013).
13. T. P. Purdy, P.-L. Yu, R. W. Peterson, N. S. Kampel, and C. A. Regal, "Strong optomechanical squeezing of light," Phys. Rev. X **3**, 031012 (2013).
14. A. Schliesser, G. Anetsberger, R. Rivière, O. Arcizet, and T. J. Kippenberg, "High-sensitivity monitoring of micromechanical vibration using optical whispering gallery mode resonators," New J. Phys. **10**, 095015 (2008).
15. M. Metcalfe, "Applications of cavity optomechanics," Appl. Phys. Rev. **1**, 031105 (2014).
16. A. Abramovici, W. E. Althouse, R. W. P. Drever, Y. Gürsel, S. Kawamura, F. J. Raab, D. Shoemaker, L. Sievers, R. E. Spero, K. S. Thorne, R. E. Vogt, R. Weiss, S. E. Whitcomb, and M. E. Zucker, "LIGO: the laser interferometer gravitational-wave observatory," Science **256**, 325–333 (1992).
17. LIGO Scientific Collaboration and Virgo Collaboration, "Observation of gravitational waves from a binary black hole merger," Phys. Rev. Lett. **116**, 061102 (2016).
18. J. D. Teufel, T. Donner, M. A. Castellanos-Beltran, J. W. Harlow, and K. W. Lehnert, "Nanomechanical motion measured with an imprecision below that at the standard quantum limit," Nat. Nanotechnol. **4**, 820–823 (2009).
19. W. Yu, W. C. Jiang, Q. Lin, and T. Lu, "Cavity optomechanical spring sensing of single molecules," Nat. Commun. **7**, 12311 (2016).
20. A. G. Krause, M. Winger, T. D. Blasius, Q. Lin, and O. Painter, "A high resolution microchip optomechanical accelerometer," Nat. Photonics **6**, 768–772 (2012).
21. F. G. Cervantes, L. Kumanchik, J. Pratt, and J. Taylor, "High sensitivity optomechanical reference accelerometer over 10 kHz," Appl. Phys. Lett. **104**, 221111 (2014).
22. S. Forstner, S. Prams, J. Knittel, E. D. vanOoijen, J. D. Swaim, G. I. Harris, A. Szorkovszky, W. P. Bowen, and H. Rubinsztein-Dunlop, "Cavity optomechanical magnetometry," Phys. Rev. Lett. **108**, 120801 (2012).
23. S. Forstner, E. Sheridan, J. Knittel, C. L. Humphreys, G. A. Brawley, H. Rubinsztein-Dunlop, and W. P. Bowen, "Ultrasensitive optomechanical magnetometry," Adv. Mater. **26**, 6348–6353 (2014).
24. C. Yu, J. Janousek, E. Sheridan, D. L. McAuslan, H. Rubinsztein-Dunlop, P. K. Lam, Y. Zhang, and W. P. Bowen, "Optomechanical magnetometry with a macroscopic resonator," Phys. Rev. Appl. **5**, 044007 (2016).
25. J. Zhu, G. Zhao, I. Savukov, and L. Yang, "Polymer encapsulated microcavity optomechanical magnetometer," Sci. Rep. **7**, 8896 (2017).
26. R. E. Slusher, L. W. Hollberg, B. Yurke, J. C. Mertz, and J. F. Valley, "Observation of squeezed states generated by four-wave mixing in an optical cavity," Phys. Rev. Lett. **55**, 2409–2412 (1985).

27. L.-A. Wu, H. J. Kimble, J. L. Hall, and H. Wu, "Generation of squeezed states by parametric down conversion," Phys. Rev. Lett. **57**, 2520–2523 (1986).
28. U. L. Andersen, T. Gehring, C. Marquardt, and G. Leuchs, "30 years of squeezed light generation," Phys. Scripta **91**, 053001 (2016).
29. C. M. Caves, "Quantum-mechanical noise in an interferometer," Phys. Rev. D **23**, 1693–1708 (1981).
30. The LIGO Scientific Collaboration, "A gravitational wave observatory operating beyond the quantum shot-noise limit," Nat. Phys. **7**, 962–965 (2011).
31. The LIGO Scientific Collaboration, "Enhanced sensitivity of the LIGO gravitational wave detector by using squeezed states of light," Nat. Photonics **7**, 613–619 (2013).
32. H. Grote, K. Danzmann, K. L. Dooley, R. Schnabel, J. Slutsky, and H. Vahlbruch, "First long-term application of squeezed states of light in a gravitational-wave observatory," Phys. Rev. Lett. **110**, 181101 (2013).
33. M. A. Taylor, J. Janousek, V. Daria, J. Knittel, B. Hage, H. A. Bachor, and W. P. Bowen, "Biological measurement beyond the quantum limit," Nat. Photonics **7**, 229–233 (2013).
34. R. C. Pooser and B. Lawie, "Ultrasensitive measurement of microcantilever displacement below the shot-noise limit," Optica **2**, 393–399 (2015).
35. N. Treps, N. Grosse, W. P. Bowen, C. Fabre, H.-A. Bachor, and P. K. Lam, "A quantum laser pointer," Science **301**, 940–943 (2003).
36. F. Wolfgramm, A. Cere, F. A. Beduini, A. Predojevic, M. Koschorreck, and M. W. Mitchell, "Squeezed-light optical magnetometry," Phys. Rev. Lett. **105**, 053601 (2010).
37. T. Horrom, R. Singh, J. P. Dowling, and E. E. Mikhailov, "Quantum-enhanced magnetometer with low-frequency squeezing," Phys. Rev. A **86**, 023803 (2012).
38. U. B. Hoff, G. I. Harris, L. S. Madsen, H. Kerdoncuff, M. Lassen, B. M. Nielsen, W. P. Bowen, and U. L. Andersen, "Quantum-enhanced micromechanical displacement sensitivity," Opt. Lett. **38**, 1413–1415 (2013).
39. C. Schäfermeier, H. Kerdoncuff, U. B. Hoff, H. Fu, A. Huck, J. Bilek, G. I. Harris, W. P. Bowen, T. Gehring, and U. L. Andersen, "Quantum enhanced feedback cooling of a mechanical oscillator using nonclassical light," Nat. Commun. **7**, 13628 (2016).
40. J. B. Clark, F. Lecocq, R. W. Simmonds, J. Aumentado, and J. D. Teufel, "Sideband cooling beyond the quantum backaction limit with squeezed light," Nature **541**, 191–195 (2017).
41. J. B. Clark, F. Lecocq, R. W. Simmonds, J. Aumentado, and J. D. Teufel, "Observation of strong radiation pressure forces from squeezed light on a mechanical oscillator," Nat. Phys. **12**, 683–687 (2016).
42. M. Korobko, L. Kleybolte, S. Ast, H. Miao, Y. Chen, and R. Schnabel, "Beating the standard sensitivity-bandwidth limit of cavity-enhanced interferometers with internal squeezed-light generation," Phys. Rev. Lett. **118**, 143601 (2017).
43. G. I. Harris, U. L. Andersen, J. Knittel, and W. P. Bowen, "Feedback-enhanced sensitivity in optomechanics: surpassing the parametric instability barrier," Phys. Rev. A **85**, 061802 (2012).
44. E. D. Black, "An introduction to Pound–Drever–Hall laser frequency stabilization," Am. J. Phys. **69**, 79–87 (2001).
45. L. Ding, C. Belacel, S. Ducci, G. Leo, and I. Favero, "Ultralow loss single-mode silica tapers manufactured by a microheater," Appl. Opt. **49**, 2441–2445 (2010).
46. E. S. Polzik, J. Carri, and H. J. Kimble, "Atomic spectroscopy with squeezed light for sensitivity beyond the vacuum-state limit," Appl. Phys. B **55**, 279–290 (1992).
47. Y. Takeno, M. Yukawa, H. Yonezawa, and A. Furusawa, "Observation of -9 dB quadrature squeezing with improvement of phase stability in homodyne measurement," Opt. Express **15**, 4321–4327 (2007).
48. T. Eberle, S. Steinlechner, J. Bauchrowitz, V. Handchen, H. Vahlbruch, M. Mehmet, H. Müller-Ebhardt, and R. Schnabel, "Quantum enhancement of the zero-area sagnac interferometer topology for gravitational wave detection," Phys. Rev. Lett. **104**, 251102 (2010).
49. H. Vahlbruch, M. Mehmet, K. Danzmann, and R. Schnabel, "Detection of 15 dB squeezed states of light and their application for the absolute calibration of photoelectric quantum efficiency," Phys. Rev. Lett. **117**, 110801 (2016).
50. A. Dutt, K. Luke, S. Manipatruni, A. L. Gaeta, P. Nussenzveig, and M. Lipson, "On-chip optical squeezing," Phys. Rev. Appl. **3**, 044005 (2015).
51. U. B. Hoff, B. M. Nielsen, and U. L. Andersen, "Integrated source of broadband quadrature squeezed light," Opt. Express **23**, 12013–12036 (2015).
52. I. Savukov and T. Karaulanov, "Magnetic-resonance imaging of the human brain with an atomic magnetometer," Appl. Phys. Lett. **103**, 043703 (2013).
53. H. Xia, A. Ben-Amar Baranga, D. Hoffman, and M. V. Romalis, "Magnetoencephalography with an atomic magnetometer," Appl. Phys. Lett. **89**, 211104 (2006).
54. J. R. Kirtley, M. B. Ketchen, K. G. Stawiasz, J. Z. Sun, W. J. Gallagher, S. H. Blanton, and S. J. Wind, "High-resolution scanning SQUID microscope," Appl. Phys. Lett. **66**, 1138–1140 (1995).
55. F. Baudenbacher, L. E. Fong, J. R. Holzer, and M. Radparvar, "Monolithic low-transition-temperature superconducting magnetometers for high resolution imaging magnetic fields of room temperature samples," Appl. Phys. Lett. **82**, 3487–3489 (2003).

Bibliography

[1]T. J. Kippenberg and K. J. Vahala, "Cavity Opto-Mechanics", Optics Express **15**, 17172 (2007) (cited on p. 1).

[2]P. N. Lebedev, *Experimental examination of light pressure*, tech. rep. (1883), p. 433 (cited on p. 1).

[3]V. B. Braginskii, *Classical and quantum restrictions on the detection of weak disturbances of macroscopic oscillator*, tech. rep. 4 (1968) (cited on p. 1).

[4]V. B.V. B. Braginskii, F. Y. Khalili, and K. S. Thorne, *Quantum measurement* (Cambridge University Press, 1995), p. 191 (cited on p. 1, 63).

[5]C. M. Caves, "Quantum-mechanical noise in an interferometer", Physical Review D **23**, 1693–1708 (1981) (cited on p. 2).

[6]M. Xiao, L.-A. Wu, and H. J. Kimble, "Precision measurement beyond the shot-noise limit", Physical Review Letters **59**, 278–281 (1987) (cited on p. 2).

[7]K. McKenzie, D. A. Shaddock, D. E. McClelland, B. C. Buchler, and P. K. Lam, "Experimental Demonstration of a Squeezing-Enhanced Power-Recycled Michelson Interferometer for Gravitational Wave Detection", Physical Review Letters **88**, 231102 (2002) (cited on p. 2).

[8]T. L. S. Collaboration et al., "A gravitational wave observatory operating beyond the quantum shot-noise limit", Nature Physics **7**, 962–965 (2011) (cited on p. 2).

[9]S. Mancini, D. Vitali, and P. Tombesi, "Optomechanical Cooling of a Macroscopic Oscillator by Homodyne Feedback", Physical Review Letters **80**, 688–691 (1998) (cited on p. 2).

[10]P. F. Cohadon, A. Heidmann, and M. Pinard, "Cooling of a mirror by radiation pressure", Physical Review Letters **83**, 2–5 (1999) (cited on p. 2).

[11]D. Leibfried, R. Blatt, C. Monroe, and D. Wineland, "Quantum dynamics of single trapped ions", Reviews of Modern Physics **75**, 281–324 (2003) (cited on p. 2).

[12]J. Chan, T. P. M. Alegre, A. H. Safavi-Naeini, J. T. Hill, A. Krause, S. Gröblacher, M. Aspelmeyer, and O. Painter, "Laser cooling of a nanomechanical oscillator into its quantum ground state", Nature **478**, 89–92 (2011) (cited on p. 2, 63).

[13]M. Rossi, D. Mason, J. Chen, Y. Tsaturyan, and A. Schliesser, "Measurement-based quantum control of mechanical motion", Nature **563**, 53–58 (2018) (cited on p. 2, 29, 63).

[14]R. A. Norte, J. P. Moura, and S. Gröblacher, "Mechanical Resonators for Quantum Optomechanics Experiments at Room Temperature", Physical Review Letters **116**, 1–11 (2016) (cited on p. 3, 29).

[15]C. Reinhardt, T. Müller, A. Bourassa, and J. C. Sankey, "Ultralow-Noise SiN Trampoline Resonators for Sensing and Optomechanics", Physical Review X **6**, 021001 (2016) (cited on p. 3, 33).

[16]M. A. M. Fox, *Quantum optics : an introduction* (Oxford University Press, 2006), p. 378 (cited on p. 5, 6, 8).

[17]D Sen, *The uncertainty relations in quantum mechanics*, tech. rep. 2 (2014) (cited on p. 5).

[18]M. O.M. O. Scully and M. S. Zubairy, *Quantum optics* (Cambridge University Press, 1997), p. 630 (cited on p. 6, 9).

[19]D. F. Walls and G. J.G. J. Milburn, *Quantum optics* (Springer, 2010), p. 425 (cited on p. 9).

[20]H.-A.H.-A. Bachor and T. C. Ralph, *A guide to experiments in quantum optics* (Wiley-VCH, 2004), p. 421 (cited on p. 10, 14).

[21]W. P. Bowen and G. J. Milburn, *Quantum optomechanics* (CRC Press) (cited on p. 11, 14, 21, 22, 26).

[22]A. A. Clerk, M. H. Devoret, S. M. Girvin, F. Marquardt, and R. J. Schoelkopf, "Introduction to quantum noise, measurement, and amplification", Reviews of Modern Physics **82**, 1155–1208 (2010) (cited on p. 13).

[23]M. Aspelmeyer, T. J. Kippenberg, and F. Marquardt, "Cavity optomechanics", Reviews of Modern Physics **86**, 1391–1452 (2014) (cited on p. 21, 29, 37, 63).

[24]A. Barchielli and B. Vacchini, "Quantum Langevin equations for optomechanical systems", New Journal of Physics **17**, 83004 (2015) (cited on p. 21).

[25]V. Giovannetti and D. Vitali, "Phase-noise measurement in a cavity with a movable mirror undergoing quantum Brownian motion", Physical Review A **63**, 023812 (2001) (cited on p. 21).

[26]C. W. Gardiner and M. J. Collett, "Input and output in damped quantum systems: Quantum stochastic differential equations and the master equation", Physical Review A **31**, 3761–3774 (1985) (cited on p. 25).

[27]T. J. Kippenberg, A. Ghadimi, D. J. Wilson, V. Sudhir, R. Schilling, N. Piro, R. Schilling, A. Ghadimi, and T. J. Kippenberg, "Measurement-based control of a mechanical oscillator at its thermal decoherence rate", Nature **524**, 325–329 (2015) (cited on p. 26, 67, 68).

[28]M. Aspelmeyer, T. J. Kippenberg, and F. Marquardt, *Cavity optomechanics : nano- and micromechanical resonators interacting with light* (2014), p. 357 (cited on p. 28).

[29]D. J. Wilson, C. A. Regal, S. B. Papp, and H. J. Kimble, "Cavity optomechanics with stoichiometric SiN films", Physical Review Letters **103**, 3–6 (2009) (cited on p. 28).

[30]I. Wilson-Rae, N. Nooshi, W. Zwerger, and T. J. Kippenberg, "Theory of ground state cooling of a mechanical oscillator using dynamical backaction", Physical Review Letters **99**, 1–4 (2007) (cited on p. 28).

[31]A. G. Krause, T. D. Blasius, and O. Painter, "Optical read out and feedback cooling of a nanostring optomechanical cavity", 1–13 (2015) (cited on p. 28, 68).

[32]C. Genes, D. Vitali, P. Tombesi, S. Gigan, and M. Aspelmeyer, "Ground-state cooling of a micromechanical oscillator: Comparing cold damping and cavity-assisted cooling schemes", Physical Review A - Atomic, Molecular, and Optical Physics **77**, 1–9 (2008) (cited on p. 28, 68).

[33]S. S. Verbridge, R. Ilic, H. G. Craighead, and J. M. Parpia, "Size and frequency dependent gas damping of nanomechanical resonators", Applied Physics Letters **93**, 1–4 (2008) (cited on p. 29).

[34]P.-L. Yu, K. Cicak, N. S. Kampel, Y. Tsaturyan, T. P. Purdy, R. W. Simmonds, and C. A. Regal, "A phononic bandgap shield for high Q membrane microresonators", Applied Physics Letters **104**, 023510 (2014) (cited on p. 29).

[35]T. P. M. Alegre, A. Safavi-Naeini, M. Winger, and O. Painter, "Quasi-two-dimensional optomechanical crystals with a complete phononic bandgap", Optics Express **19**, 5658 (2011) (cited on p. 29).

[36]Y. Tsaturyan, A. Barg, A. Simonsen, L. G. Villanueva, S. Schmid, A. Schliesser, and E. S. Polzik, "Demonstration of suppressed phonon tunneling losses in phononic bandgap shielded membrane resonators for high Q optomechanics", **22**, 6810–6821 (2013) (cited on p. 29, 41).

[37]S Schmid, K. D. Jensen, K. H. Nielsen, and A Boisen, "Damping mechanisms in high-Q micro and nanomechanical string resonators", PHYSICAL REVIEW B **84**, 165307 (2011) (cited on p. 29).

[38]B. E. A. Saleh and M. C. Teich, *Fundamentals of photonics* (Wiley-Interscience, 2007), p. 1177 (cited on p. 35, 38).

[39]F. F. Trager, *Springer handbook of lasers and optics*, edited by F. Träger (Springer, Berlin, Heidelberg, 2012), p. 1694 (cited on p. 35).

[40]U. L. Andersen, T. Gehring, J. Bilek, H. Fu, W. P. Bowen, C. Schäfermeier, U. B. Hoff, A. Huck, G. I. Harris, and H. Kerdoncuff, "Quantum enhanced feedback cooling of a mechanical oscillator using nonclassical light", Nature Communications **7** (2016) `10.1038/ncomms13628` (cited on p. 37, 64, 69, 79, 83).

[41]A. E. Siegman, *Lasers* (University Science Books, 1986), p. 1283 (cited on p. 38, 39).

[42]C. J. Hood, H. J. Kimble, and J. Ye, "Characterization of high-finesse mirrors: Loss, phase shifts, and mode structure in an optical cavity", Physical Review A - Atomic, Molecular, and Optical Physics **64**, 7 (2001) (cited on p. 50).

[43]H. Schmuck and O. Strobel, "Stabilization of a Fiber-Optic Mach-Zehnder-Interferometer Used as an Intensity Modulator", Journal of Optical Communications **7**, 86–91 (1986) (cited on p. 55).

[44]M. L. Gorodetsky, A. Schliesser, G. Anetsberger, S. Deleglise, and T. J. Kippenberg, "Determination of the vacuum optomechanical coupling rate using frequency noise calibration", Optics Express **18**, 23236 (2010) (cited on p. 58).

[45]D. Rugar, R. Budakian, H. J. Mamin, and B. W. Chui, "Single spin detection by magnetic resonance force microscopy", Nature **430**, 329–332 (2004) (cited on p. 63).

[46]P. F. Michelson, J. C. Price, R. C. Taber, Y. Gürsel, S. Kawamura, F. J. Raab, D. Shoemaker, L. Sievers, R. E. Spero, K. S. Thorne, R. E. Vogt, R. Weiss, S. E. Whitcomb, and M. E. Zucker, "Resonant-mass detectors of gravitational radiation.", Science (New York, N.Y.) **237**, 150–7 (1987) (cited on p. 63).

[47]A Abramovici, W. E. Althouse, R. W. Drever, Y Gürsel, S Kawamura, F. J. Raab, D Shoemaker, L Sievers, R. E. Spero, K. S. Thorne, R. E. Vogt, R Weiss, S. E. Whitcomb, and M. E. Zucker, "LIGO: The Laser Interferometer Gravitational-Wave Observatory.", Science (New York, N.Y.) **256**, 325–33 (1992) (cited on p. 63).

[48]W. Marshall, C. Simon, R. Penrose, and D. Bouwmeester, "Towards Quantum Superpositions of a Mirror", Physical Review Letters **91**, 130401 (2003) (cited on p. 63).

[49]C. Fabre, M. Pinard, S. Bourzeix, A. Heidmann, E. Giacobino, and S. Reynaud, "Quantum-noise reduction using a cavity with a movable mirror", Physical Review A **49**, 1337–1343 (1994) (cited on p. 63).

[50]D. Vitali, S. Gigan, A. Ferreira, H. R. Böhm, P. Tombesi, A. Guerreiro, V. Vedral, A. Zeilinger, and M. Aspelmeyer, "Optomechanical Entanglement between a Movable Mirror and a Cavity Field", Physical Review Letters **98**, 030405 (2007) (cited on p. 63).

[51]D. J. Wineland and W. M. Itano, "Laser cooling of atoms", Physical Review A **20**, 1521–1540 (1979) (cited on p. 63).

[52]O. Arcizet, P.-F. Cohadon, T. Briant, M. Pinard, and A. Heidmann, "Radiation-pressure cooling and optomechanical instability of a micromirror", Nature **444**, 71–74 (2006) (cited on p. 63).

[53]R. Ma, A. Schliesser, P. Del'Haye, A. Dabirian, G. Anetsberger, and T. J. Kippenberg, "Radiation-pressure-driven vibrational modes in ultrahigh-Q silica microspheres", Optics Letters **32**, 2200 (2007) (cited on p. 63).

[54]A. Schliesser, P. Del'Haye, N. Nooshi, K. J. Vahala, and T. J. Kippenberg, "Radiation Pressure Cooling of a Micromechanical Oscillator Using Dynamical Backaction", Physical Review Letters **97**, 243905 (2006) (cited on p. 63).

[55]K Usami, A Naesby, T Bagci, B Melholt Nielsen, J Liu, S Stobbe, P Lodahl, and E. S. Polzik, "Optical cavity cooling of mechanical modes of a semiconductor nanomembrane", Nature Physics **8**, 22 (2012) (cited on p. 63).

[56]S. Mancini, D. Vitali, P. Tombesi, U. Camerino, and I Camerino, "Phys. Rev. Lett. 80, 688 (1998) - Optomechanical Cooling of a Macroscopic Oscillator by Homodyne Feedback", Journals.Aps.Org, 2–5 (1998) (cited on p. 63).

[57]K. H. Lee, T. G. McRae, G. I. Harris, J. Knittel, and W. P. Bowen, "Cooling and control of a cavity optoelectromechanical system", Physical Review Letters **104**, 1–4 (2010) (cited on p. 64).

[58]M. Poggio, C. L. Degen, H. J. Mamin, and D. Rugar, "Feedback cooling of a cantilever's fundamental mode below 5 mK", Physical Review Letters **99**, 1–4 (2007) (cited on p. 64, 66).

[59]T. Corbitt, C. Wipf, T. Bodiya, D. Ottaway, D. Sigg, N. Smith, S. Whitcomb, and N. Mavalvala, "Optical Dilution and Feedback Cooling of a Gram-Scale Oscillator to 6.9 mK", Physical Review Letters **99**, 160801 (2007) (cited on p. 64).

[60]A. A. Clerk, S. M. Girvin, F. Marquardt, R. J. Schoelkopf, and M. H. Devoret, "Introduction to quantum noise, measurement, and amplification: Online Appendices", Reviews of Modern Physics **82**, 1155–1208 (2010) (cited on p. 66).

[61]B. C. Buchler, M. B. Gray, D. A. Shaddock, T. C. Ralph, and D. E. McClelland, "Suppression of classic and quantum radiation pressure noise by electro-optic feedback", Optics Letters **24**, 259 (1999) (cited on p. 66).

[62]E. D. Black, "An introduction to Pound–Drever–Hall laser frequency stabilization", American Journal of Physics **69**, 79–87 (2001) (cited on p. 70).

[63]L. Neuhaus and S. Deléglise, *PyRPL*, 2006 (cited on p. 73).

[64]U. B. Hoff, G. I. Harris, L. S. Madsen, H. Kerdoncuff, M. Lassen, B. M. Nielsen, W. P. Bowen, and U. L. Andersen, "Quantum-enhanced micromechanical displacement sensitivity", Optics Letters **38**, 1413 (2013) (cited on p. 79, 83).

[65]B.-B. Li, J. Bílek, U. B. Hoff, L. S. Madsen, S. Forstner, V. Prakash, C. Schäfermeier, T. Gehring, W. P. Bowen, and U. L. Andersen, "Quantum enhanced optomechanical magnetometry", Optica **5**, 850 (2018) (cited on p. 79, 83).

[66]M. V. Larsen, X. Guo, C. R. Breum, J. S. Neergaard-Nielsen, and U. L. Andersen, "Fiber coupled EPR-state generation using a single temporally multiplexed squeezed light source", (2018) (cited on p. 79).

[67]I. Savukov and T. Karaulanov, "Magnetic-resonance imaging of the human brain with an atomic magnetometer", Applied Physics Letters **103**, 043703 (2013) (cited on p. 82).

[68]A. Edelstein, "Advances in magnetometry", Journal of Physics: Condensed Matter **19**, 165217 (2007) (cited on p. 82).

[69]S. Forstner, E. Sheridan, J. Knittel, C. L. Humphreys, G. A. Brawley, H. Rubinsztein-Dunlop, and W. P. Bowen, "Ultrasensitive Optomechanical Magnetometry", Advanced Materials **26**, 6348–6353 (2014) (cited on p. 82).

[70]R. Osiander, S. A. Ecelberger, R. B. Givens, D. K. Wickenden, J. C. Murphy, and T. J. Kistenmacher, "A microelectromechanical-based magnetostrictive magnetometer", Applied Physics Letters **69**, 2930–2931 (1996) (cited on p. 82).

[71]A. Grosz, M. J. Haji-Sheikh, and S. C. Mukhopadhyay, *High Sensitivity Magnetometers* (Springer, 2016) (cited on p. 82).

[72]S. Forstner, J. Knittel, E. Sheridan, J. D. Swaim, H. Rubinsztein-Dunlop, and W. P. Bowen, "Sensitivity and performance of cavity optomechanical field sensors", Photonic Sensors (2012) `10.1007/s13320-012-0067-2` (cited on p. 82).

[73]B.-B. Li, D. Bulla, V. Prakash, S. Forstner, A. Dehghan-Manshadi, H. Rubinsztein-Dunlop, S. Foster, and W. P. Bowen, "Invited Article: Scalable high-sensitivity optomechanical magnetometers on a chip", APL Photonics **3**, 120806 (2018) (cited on p. 82).

[74]C. Schäfermeier, "Quantum enhanced optical sensing", PhD thesis (DTU, 2016) (cited on p. 82).

[75]C. Schäfermeier, M. Ježek, L. S. Madsen, T. Gehring, and U. L. Andersen, "Deterministic phase measurements exhibiting super-sensitivity and super-resolution", Optica **5**, 60 (2018) (cited on p. 82).

[76]U. B. Hof, "Integrated Quantum Optics Experiments towards integrated quantum-light sources and quantum-enhanced sensing", PhD thesis (DTU, 2015) (cited on p. 82).

[77]G. I. Harris, U. L. Andersen, U. B. Hoff, W. P. Bowen, and H. Kerdoncuff, "Squeezing-enhanced measurement sensitivity in a cavity optomechanical system", Annalen der Physik **527**, 107–114 (2014) (cited on p. 83).